

Neuroprosthetic system to restore locomotion after neuromotor disorder

THÈSE N° 6408 (2014)

PRÉSENTÉE LE 9 DÉCEMBRE 2014

À LA FACULTÉ DES SCIENCES DE LA VIE
CHAIRE IRP EN RÉPARATION DE LA MOËLLE ÉPINIÈRE
PROGRAMME DOCTORAL EN NEUROSCIENCES

ÉCOLE POLYTECHNIQUE FÉDÉRALE DE LAUSANNE

POUR L'OBTENTION DU GRADE DE DOCTEUR ÈS SCIENCES

PAR

Nikolaus WENGER

acceptée sur proposition du jury:

Prof. C. Sandi, présidente du jury
Prof. G. Courtine, directeur de thèse
Prof. O. Blanke, rapporteur
Prof. R. Gassert, rapporteur
Prof. E. Rouiller, rapporteur



ÉCOLE POLYTECHNIQUE
FÉDÉRALE DE LAUSANNE

Suisse
2014

Contents

A compiled PhD thesis format.....	4
Abstract English.....	4
Zusammenfassung auf Deutsch	5
Introduction.....	7
Anatomy of the spinal cord and spinal cord reflexes.....	7
General introduction to traumatic spinal cord injury	7
Classification of Spinal cord injury.....	8
From bench to bedside: spinal cord injury treatments.....	8
Treadmill training	9
Epidural Electrical Stimulation	9
Electrochemical spinal cord stimulation	10
Spatiotemporal neuromodulation to improve recovery from spinal cord injury	11
Neuroprosthetic systems and their design requirements	11
Neuroprosthetic system to restore locomotion after spinal cord injury	12
Mechanistic insights into the effect electrical spinal cord stimulation.....	12
Spatial mapping experiments.....	13
Temporal mapping experiments	15
A neuroprosthetic system for spatiotemporal modulation of spinal circuits	15
Conclusion	16
Original research articles.....	17
A computational model for epidural electrical stimulation of spinal sensorimotor circuits	17
Closed-loop neuromodulation of spinal sensorimotor circuits controls refined locomotion after complete spinal cord injury.....	17
Translational neuroprosthetic toolbox for modulation of spinal sensorimotor circuits in space and time	17
Discussion.....	18
Spinal cord model and electrode array design.....	18
Closed loop neuromodulation and translation in human subjects.....	19
Novelty of the technological platform for closed loop neuromodulation	20
Detailed contributions of the candidate	21
Concept and validation of the computational spinal cord model.....	22
Fabrication and optimization of multi electrode arrays.....	22
Development of real time control algorithms.....	24
Outlook.....	25

Acknowledgments	26
Bibliography.....	27

A compiled PhD thesis format

A PhD student at EPFL is eligible to submit a PhD thesis in "compiled" format if the student has contributed substantially to at least 3 publications. In this case the thesis will contain an introduction, the original research articles and a discussion. (1) The introduction is intended to give the background of the research, and to summarize and link the publications. (2) The original research articles can be accepted or submitted. (3) The general discussion and conclusion summarize the main contributions of the student, the originality of the thesis work and its relationship to other research in the field. I tried to clearly outline these requirements in the structure of the manuscript and I remain in wishing you a pleasant read.

Abstract English

Neuromodulation of spinal sensorimotor circuits improves motor control in animal models and humans with Spinal Cord Injury (SCI) and Parkinson disease. Stimulation parameters are tuned manually and remain constant during motor execution which is suboptimal to mediate maximum therapeutic effects. Here, I present a novel neuroprosthetic system that enabled adaptive changes of neuromodulation parameters during locomotion and allowed to restore high-fidelity control over leg movements in paralyzed rats. Beyond the therapeutic potential, these findings provide a conceptual and technical framework to personalize neuromodulation treatments for other neurological disorders.

Several limitations have restricted the development of neuroprosthetic systems for closed loop neuromodulation. **(1)** First, it required a mechanistic understanding of the relationships between stimulation features and the recruitment of specific sensorimotor circuits. I found that electrical neuromodulation primarily recruits afferent reflex pathways that lead to coordinated activity of leg muscles during stepping. Moreover, the specific electrode location on the spinal cord could activate distinct reflex pathways and activate specific leg muscle groups of paralyzed rats. These results have been leveraged for the design of flexible and stretchable multi-electrode arrays for electrical and chemical spinal cord stimulation. **(2)** Second, it was necessary to perform comprehensive mapping experiments to characterize the effect of neuromodulation parameters on hind limb kinematics in order to establish stable and robust feedback signals for real time control. Step height and ground reaction forces emerged as the primary targets for the control of closed loop neuromodulation after spinal cord injury. **(3)** Third, implementation and optimization of closed-loop neuromodulation strategies necessitated the development of an advanced technological platform that combined feedback and feed-forward loops that match the natural flow of information in the modulated neural systems.

These integrated developments allowed animals with complete spinal cord injury to perform over 1000 successive steps without failure, and to climb staircases of various heights and lengths with precision and fluidity. Moreover, the neuroprosthetic system was able to alleviate locomotor deficits in an alpha-synuclein rodent model of Parkinson's disease.

Current knowledge of human spinal cord properties in response to electrical neuromodulation suggests that the developed control policies can translate into clinical applications to improve neurorehabilitation therapies. Moreover, the developed neuroprosthetic system can readily be interfaced with control signals from the brain to establish cortico-spinal neuroprostheses that are intended to promote activity-dependent plasticity during recovery from spinal cord injury.

Key words: Spinal cord injury, Neuroprosthetics, Electrical spinal cord stimulation, Multi electrode array, Closed-loop control, Spatiotemporal neuromodulation

Zusammenfassung auf Deutsch

Elektrische Stimulation des Rückenmarks verbessert motorische Defizite nach Querschnittslähmung und Parkinson Erkrankung im Tiermodell und im Menschen. Typischer Weise werden die Parameter der elektrischen Stimulation manuell kalibriert und bleiben während des gesamten Bewegungsvorganges konstant. In dieser Doktorats Arbeit präsentiere ich ein neuroprothetisches System das adaptive Veränderung der Stimulations Parameter während des Bewegungsvorganges erlaubt. Nach experimenteller Querschnittslähmung konnten wir dadurch erstmals einen hohen Grad von Bewegungskontrolle wieder herstellen. Neben den therapeutischen Potential dieses Verfahrens ergeben sich aus den Resultaten Konzepte und technologische Möglichkeiten für die personalisierte Neuromodulations Therapie bei anderen neurologischen Erkrankungen.

Für die Entwicklung des neuroprothetischen Systems mussten mehrere funktionelle und technologische Aspekte berücksichtigt werden. **(1)** Zuerst haben wir die anatomische Strukturen untersucht, die durch die elektrische Rückenmarksstimulation angeregt werden. Wir konnten zeigen, dass die Rückenmarksstimulation vor allem afferenten Reflexbahnen in den Dorsalwurzeln des Rückenmarks anregt. Wir konnten das Gangbild querschnittsgelähmter Ratten angeregt durch Elektrostimulation auf die koordinierte Modulation von Muskel Reflexen zurückzuführen. Darüber hinaus konnten wir zeigen, dass Elektroden an verschiedenen Rückenmarks Segmenten spezifische Muskel Gruppen in den Beinen aktivieren. Diese Resultate führten zur Entwicklung von dehnbaren und flexiblen Multi Elektroden Arrays für elektrische und chemische Rückenmarksstimulation. **(2)** Zweitens war

es notwendig den funktionellen Zusammenhang zwischen Stimulations Parametern und der Modulation von Bein Bewegungen zu charakterisieren. Das Ziel war damit stabile Eingangssignale für die Echtzeit Bewegungskontrolle zu etablieren. Schritthöhe und vertikale Kraftentwicklung konnten als Hauptparameter für das Bewegungskontroll System identifiziert werden. (3) Drittens, für die praktische Umsetzung der Echtzeit Bewegungskontrolle war es notwendig eine technologische Plattform zu entwickeln, welche die Integration von Feed-back Signalen und Feed-forward Modellen erlaubt. Die entwickelte online Signalverarbeitung war dem natürlichen Informationsfluss des gesunden Nervensystems nachempfunden.

Das entwickelte neuroprothetische System ermöglicht Tieren mit kompletter Lähmung der Beine über 1000 kontinuierliche Schritte durchzuführen und die Schritthöhe gezielt an Stufen verschiedener Höhe und Länge anzupassen. Darüber hinaus konnte unser neuroprothetischen System das Gangbild im alpha-synuclein Tier model der Parkinson Erkrankung verbessern.

Kenntnisse über die physiologischen Eigenschaften des Rückenmarks und der Reaktion auf Elektrostimulation legen Nahe, dass die entwickelten Strategien zur Echtzeit Bewegungskontrolle in der Klinik übertragen werden können. Darüber hinaus, bietet das entwickelte neuroprothetische System die Möglichkeit einer Schnittstelle zwischen Signalen motorischer Hirn Areale und der Rückenmarksstimulation. Damit kann eine Koritko-Spinale Neuroprothese etabliert werden, deren Ziel es ist die neuronale Plastizität in der Rehabilitation nach Querschnittslähmung anzuregen und zu verbessern.

Stichwörter: Querschnittslähmung, Neuroprothetik, Elektrische Rückenmarksstimulation, Multi Elektroden Array, Echtzeit Bewegungskontrolle, Adaptive Neuromodulation

Introduction

Anatomy of the spinal cord and spinal cord reflexes

The spinal cord consists of segments that are defined by their respective nerve roots. For example, an afferent nerve root that enters the vertebral canal below vertebra S1 will define the location of spinal segment S1. Inside the vertebral canal the nerve roots run in the subarachnoid space ensheathed by myelin. Once the nerve roots reach their respective segments, they enter the spinal cord and synapse onto interneurons and motoneurons. These synaptic connections give rise to polysynaptic and monosynaptic reflex circuits.

Monosynaptic reflex circuits are activated by group Ia afferents, which have their sensors in the primary muscle spindles. Spindles sense the stretch of a muscle and induce a monosynaptic activation of motoneurons that contracts the same muscle. Polysynaptic reflex pathways receive their innervation from Ia, Ib II and cutaneous afferents. These circuits have a more complex organization and can consist of one or more inhibitory and excitatory interneurons. For example the projections of Ia afferents of an ankle flexor activate monosynaptic response in the ankle flexor. At the same time these very Ia afferents activate inhibitory interneurons that project onto motoneurons of ankle extensors of the same leg causing a reciprocal inhibition of extensor and flexor muscles.

Interneurons form distributed networks in the spinal cord. Inhibitory as well as excitatory interneurons can project to the same segment, project over several segments or cross to the contralateral side of the spinal cord. Epidural electrical stimulation (spinal cord stimulation) can activate the distributed spinal cord networks and generate a coordinated locomotor output (1). Anatomically, the electrodes for spinal cord stimulation are placed on the dorsal surface of the dura mater outside the spinal cord. The electrical field propagates into the cerebrospinal fluid in the subarachnoid space to activate the dorsal roots and their multiple reflex circuits (2).

General introduction to traumatic spinal cord injury

Severe lesions of the spinal cord lead to permanent paralysis of the legs. The majority of spinal cord injuries is traumatic in nature and related to car accidents (39.2%), falls (28.3 %) and violence (14.6 %) (3, 4). The most frequent neurologic categories at discharge from the hospital are incomplete tetraplegia (40.8%, partial paralysis in all four extremities), complete paraplegia (21.6%, complete paralysis in the legs), followed by incomplete paraplegia (21.4%) and complete tetraplegia (15.8%). Less than 1% of all patients reach a complete neurologic recovery (5).

The early age of onset (average age 33.1 in Europe and 28.7 in the US) leads to high financial costs shared between individuals and society (6-9). Treatments that lead to partial recovery after spinal cord injury can improve the health and quality of life in affected

individuals (10-13). The incident of spinal cord injury ranges from 11 to 59 patients per million inhabitants per year in Europa and the US which results in an estimated 22000 new cases every year. The estimated lifetime spending on healthcare in spinal cord injury patients in the US ranges from 1.5 to 4.5 million US dollars for each individual patient depending on the severity grade of the lesion (3-5). Thus it is of social and economic interest to translate experimental therapies that achieve improved recovery after spinal cord injury to human patients.

Classification of Spinal cord injury

The outcome of recovery greatly correlates with the initial severity of the injury. Thus it is important to have reproducible measures of the functional impairment early after injury. The most widely used classification of spinal cord injury is the ASIA score (American Spinal Injury Association). The ASIA impairment scale assesses sensory and motor function and is graded from A to E. ASIA A corresponds to complete spinal cord injury, with no motor or sensory function below the level of the injury. ASIA B to D corresponds to incomplete spinal cord injuries with different degrees of preserved sensorimotor motor function. ASIA E classifies the healthy population. Depending on the segmental level of the injury there can be a variety of additional body dysfunctions that affect the respiratory system, bladder and bowel functions. Despite acute traumatic treatments and neurorehabilitation, most patients with complete spinal cord injury reach no meaningful neurological recovery of sensorimotor or body functions (14).

From bench to bedside: spinal cord injury treatments

As early as 1910, C. Sherrington has provided insight that the neural tissue below the level of spinal cord injury is able to generate a coordinated motor output when provided with sensory stimulation(15, 16). Consequently, many strategies to improve motor recovery after spinal cord injury have intended to increase the activity of neural circuits below the lesion.

The concept of the Central Pattern Generator (CPG) describes the capacity of neural circuits below the lesion to generate an oscillating output in the absence of external sensory information (17). Little is known about the individual cell types and interneurons that compose the central pattern generator in mammals. However, we do know that interconnected network of excitatory and inhibitory interneurons are essential to mediate the coordination of locomotion (18). Individual types of interneurons identified by cell type specific promoters (type V0, V1, V2) are essential to mediate the alternation and the oscillating rhythm of stepping (18, 19). These distributed networks of interneurons innervate flexor and extensor motor neurons for both legs. Stepping, in turn, results from a coordinated activation of flexor and extensor motor neurons projecting to the left and right leg.

Experiments that study the neural mechanism of locomotion typically achieve locomotion providing sensory, electrical or chemical stimulation as external sources of neural excitation (15, 17). Research has tried to translate these interventions to improve locomotor recovery after spinal cord injury.

Treadmill training

Treadmill training provides sensory information to the neural tissue below the lesion (20). Barbeau and Rossignol (1987) showed that adult cats after a complete spinal cord injury can recover full weight bearing stepping after training on a treadmill (21). The changes in stepping capacity resulted in long lasting use dependent plasticity of neural circuits (22-24). For example, treadmill training decreased the amount of inhibitory neurotransmitter receptors (GABA-A) below the lesion, which in turn improved stepping (25, 26).

These results in animal experiments triggered the translation of activity-based training therapies in human subjects (27). Locomotor training therapy was successful in improving walking capacities in patients with incomplete spinal cord injury (28-31). For example, Dobkin et al., 2007 showed that 92 % of incomplete spinal cord injured subjects could regain walking abilities at functional speeds (32). However, locomotor training has not been sufficient for the recovery of walking abilities in patients with motor complete paralysis (33). Consequently, research has investigated additional option to provide increased levels of excitation to the spinal cord.

Epidural Electrical Stimulation

Epidural electrical stimulation tries to activate spinal circuits through sensory afferents (2, 34). During treadmill stepping, electrical stimulation evokes a succession of reflex responses in leg muscles. The coordinated alternation of flexor and extensor muscles triggered from continuous electrical stimulation pulses mediates stepping (35). Therapeutically, this intervention could be exploited to generate stepping in animal models of complete spinal cord injury (1).

Translation of electrical spinal cord stimulation in human subjects has been accelerated by electrode implants that were originally designed for the treatment of chronic pain (36) and the control of spasticity in subjects with spinal cord injury (37). Provided these implants, Dimitrijevic et al. 1998 studied the effect of electrical spinal cord stimulation in six complete paraplegic subjects classified as ASIA A (no motor or sensory functions below the lesion) (38). Tonic electrical stimulation over the lumbar segments was effective in inducing rhythmic, alternation of stance and swing phases when subjects were positioned on their back. Moreover, Gerasimenko et al. 2002 reported vertical step like movements with electrical spinal cord stimulation in a subject with complete SCI who was fully supported by a parachute harness(39).

Next, Epidural electrical stimulation was combined with partial weight bearing treadmill training (40-44). Individual case studies report improved locomotor activity in incomplete as well as complete spinal cord injured subjects. Carhartt et al. 2004 describe an improvement in over-ground ambulation in a tetraplegic subject with incomplete paralysis after the combination of locomotor training with epidural electrical stimulation. A maximum of 150 m over ground walking distance could be improved to a maximum of 325 m in the presence of stimulation (43). Minassian et al. 2007 report increased muscular activity during manually assisted treadmill locomotion in complete paraplegic patients (41).

More recently, the research group of Reggie Edgerton at UCLA was able to show a consistent therapeutic effect of epidural electrical stimulation in 4 ASIA A patients with complete motor paralysis (40, 45). After combination of locomotor training and epidural electrical stimulation all subjects were able to regain voluntarily control of leg movements when positioned on their back (45). Moreover, the patients improved autonomous and sexual functions which provided a comprehensive clinical benefit of the therapy (46).

In conclusion, the combination of training and electrical stimulation achieves improved functional recovery after spinal cord injury compared to training alone. However, there remains the limitation that no patient with motor complete spinal cord injury was able to recover over ground walking abilities. Voluntary control is limited to conditions where gravity is minimal. Consequently, therapeutic strategies for spinal cord stimulation need to take one step forward in order to provide adequate amount of excitation to the spinal cord after injury.

Electrochemical spinal cord stimulation

Spinal cord injuries interrupt monoaminergic neurotransmitter systems from the brain stem (47). The transport of serotonin, noradrenalin and dopamine to the spinal cord is interrupted and leads to permanent paralysis. Consequently, the application of monoaminergic neurotransmitters to the spinal cord enables generation of locomotion (19). Serotonin, for example, mediates its effect through multiple receptor subtypes (5-HT 1, 2, 7) that change the electrical properties of excitatory and inhibitory interneurons and motor neurons (48). The compound modulation of distributed excitatory and inhibitory interneuron networks results in stepping movements (47).

Varied pharmacological replacement strategies have been proposed for the treatment of spinal cord injury (17, 49, 50). Different from epidural electrical stimulation paradigms which target the activation of sensory afferents, chemical stimulation activates g-protein coupled receptors and results in changes of electrical properties in distributed neural networks (47). The combined application of electrical and chemical stimulation achieves synergistic effects on locomotion. Treadmill training in combination with electrochemical stimulation enabled rats with complete spinal cord injury for the first time to regain full weight-

bearing stepping on the treadmill (50). Different from cats, but similar like human, rats are not able to recover full weight bearing stepping with treadmill training alone.

It is promising that beyond the functional improvements in stepping, the combination of motor training and electrochemical stimulation augments use dependent plasticity in the spinal cord and above the injury (51). Rats, that received a severe spinal cord injury leaving a small tissue bridge intact, were trained to voluntarily engage into an over ground locomotion task in a decreased gravitational environment. After training, assisted by electrochemical stimulation, new anatomical connections were formed between motor cortex and relay interneurons in the spinal cord. These newly formed detour circuits were essential and sufficient to signal voluntary commands to the spinal cord.

The combination of electrical and chemical stimulation holds promising therapeutic perspectives for translation into human subjects. Indeed, first experimental data on the functional benefit of electrochemical spinal cord stimulation in subjects with severe upper limb paralysis have been presented at the Annual Meeting of the Society for Neuroscience 2013 (52). A combination of transcutaneous electrical spinal cord stimulation with Buspiron, a human approved 5-HT 1A agonist, could significantly increase grasping strength in 4 tetraplegic patients.

Spatiotemporal neuromodulation to improve recovery from spinal cord injury

Electrochemical stimulation mediates its functional effects through the increased excitation of remaining spinal circuits below the level of the lesion. The question remained, however, if current electrochemical stimulation paradigms mediate maximum therapeutic effects? Current stimulation paradigms provide a tonic input to the spinal cord to activate dynamic changes in neural circuits during motor execution. Here, we hypothesized that introducing temporal and spatial structure in electrical spinal cord stimulation strategies will augment the therapeutic effect and benefit recovery after spinal cord injury. Moreover, we asked whether adaptive changes in spinal cord stimulation could restore a more refined degree of leg movement control after severe spinal cord injury. These questions motivated the design of a neuroprosthetic system for spatial and temporal modulation of electrical spinal cord stimulation.

Neuroprosthetic systems and their design requirements

Neuroprosthetic systems try to restore sensory and motor function after neurological disorders. Typically, these systems are composed of an implant that provides electrical stimulation to neural tissues and a real time processing device that replaces lost body function. The electrical stimulation patterns try to match spatial and temporal characteristics of neural circuit in the healthy state.

For example the cochlear implant replaces function of lost inner hair cells in deaf patients(53). Hair cells are positioned in distinct spatial location in the inner ear to transform differential frequencies of sound into auditory signals. The cochlear implant replaces function of hair cells and transmits electrical pulses directly to the auditory nerve. A signal processing device continuously monitors sound and adapts the appropriate electrical stimulation features in time to activate different electrodes positioned at different nerve endings of the auditory nerve. Electrode location, amplitude-, frequency- and pulse width of the stimulation pulses are adjusted in order to generate appropriate perception of sound.

The design of a neuro-prosthetic system is an integrated conceptual process. First, it requires a good understanding of neuroanatomy and neurophysiology of the affected part of the nervous system. Next, it relies on the characterization of the functional effect of electrical stimulation on sensory and motor function. Third, it requires the ability to design and fabricate the final implant and a real time processing device. All these aspects need to be addressed concurrently in order to develop a fully operational neuroprosthetic system.

Neuroprosthetic system to restore locomotion after spinal cord injury

Several limitations have restricted the development of neuroprosthetic systems for spatiotemporal neuromodulation of spinal circuits in the past. First, it required a detailed understanding of the anatomical structures recruited by the electrical spinal cord stimulation. Second, it was necessary to perform comprehensive mapping experiments to characterize the effect of of spatial and temporal modulation features on hind limb kinematics. Third it required the design of a multi-electrode array and the development of a real time control platform.

During the PhD thesis, these combined developments were leveraged to assess the benefits of spatiotemporal neuromodulation on the functional recovery after severe spinal cord injury. We designed closed-loop stimulation algorithms that restored refined control of leg movements after complete paralysis. Moreover, the neuroprosthetic system was able to alleviate locomotor deficits in an alpha-synuclein model of Parkinson's disease.

Mechanistic insights into the effect electrical spinal cord stimulation

In order to understand the neuroanatomical structures that are stimulated by epidural electrical stimulation, we developed a computational model of the spinal cord (Capogrosso, Wenger et al. 2013). The model is composed of anatomical compartments that can predict the recruitment of different neural structures (axons, neurons, interneurons) in response to electrical stimulation. We validated the model predictions experimentally by using muscle vibration and pharmacology to selectively block monosynaptic and polysynaptic reflex circuits.

We found at low currents (≤ 200 μA amplitude, 0.2 ms pulse duration) electrical stimulation mediates the recruitment of afferent sensory fibers of group Ia, Ib and group II fibers. At high currents (≥ 200 μA amplitude, 0.2 ms pulse duration) electrical stimulation also recruits the efferent axons of motor neurons. Most importantly, we found that epidural electrical stimulation is not able to activate spinal cord neurons directly. Interneurons and motor neurons are shielded by the white matter of the spinal cord which acts as an insulator to the electrical field that is distributed in the cerebrospinal fluid around the spinal cord. The current used for electrical stimulation during locomotor training corresponds to low current ranges below 200 μA . Thus, we provide evidence that the functional effect of spinal cord stimulation in spinal cord injured animals is mediated through the selective recruitment of sensory afferents.

In a next step, the results of the computational model provided a working hypothesis for the design of the neuroprosthetic systems. In order to achieve spatial selectivity the electrodes of the implant had to be placed in close apposition to the afferent fiber pathways. The electrode distribution had to match the spatial arrangement of the spinal roots (Figure 1).

Spatial mapping experiments

We aimed to take advantage of the spatial distribution of spinal roots in order to recruit specific motor neuron pools in the spinal cord by stimulating spinal roots and their monosynaptic projections onto motor neurons. This aim triggered experimental mapping of anatomical location of spinal roots and motor neuron pools in rats (Figure 1).

Next, we explored whether electrical stimulation applied at different locations of the lumbosacral spinal cord can activate distinct reflex pathways and activate specific leg muscles. Electrical stimulation was applied at each spinal cord segment in the midline and 0.75 mm lateral displacement. Stimulation of left-sided S1 electrode generated unilateral activity in distal spinal cord segments (increased density of extensor motor pools) which evoked unilateral hind limb extension. Stimulation of left-side L2 electrode facilitated left hind limb flexion by the selective activation of proximal spinal cord segments (increased density of flexor motor pools).

Next, the location of lumbar spinal roots was measured with respect to the size of vertebrae, spinal cord segments and motor neuron pool locations (Figure 1). The combined anatomical measurements and functional experiments were leveraged to the design of a multi electrode array for electrical spinal cord stimulation (Figure 1 and 2).

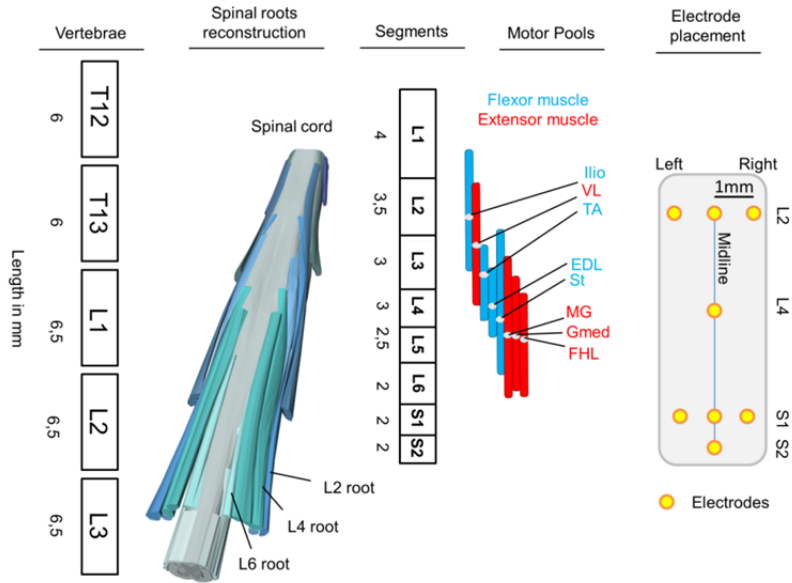


Figure 1 Anatomical mapping experiments that steered the final design of the multi electrode array. Dimensions of the implant were determined from detailed anatomical measurements of vertebrae, spinal roots and spinal cord segment during anatomical dissections in rats. Motor neuron pool locations were determined by the reconstruction of motor neurons after retrograde tracer injection experiments (Fluorogold retrograde labelling for each muscle). The multi electrode array was designed with 8 electrodes. Each electrode was determined to achieve a specific functional effect: Electrodes placed at S1 left and S1 right spinal cord segments were selected to promote left and right extension of the hind limbs; L2 left and L2 right electrodes for left and right hind limb flexion; S1 midline and L2 midline electrodes for comparison with experiments in previous literature; L4 midline as a global stimulation site that activates a majority of hind limb muscles located at L4 spinal cord segment; S2 midline electrode for practical reasons, to double the S1 midline electrodes in case of electrode failure.

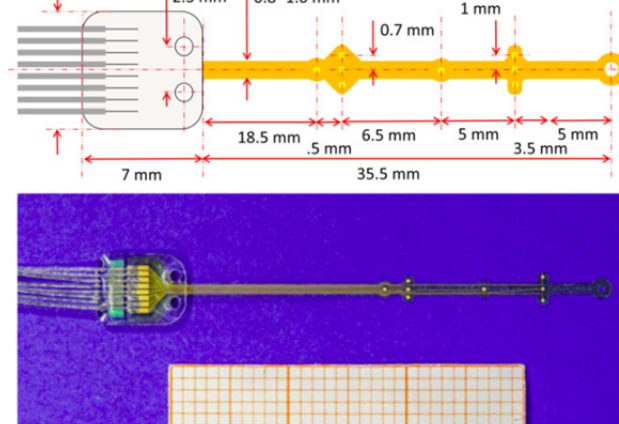


Figure 2 Multi electrode array design and final implant fabricated by the Institute for Microtechnology Mainz (IMM) (photograph of array with courtesy of Dr. Peter Detemple).

Temporal mapping experiments

In order to investigate the functional benefit of temporal changes in electrical spinal cord stimulation, we characterized the effect of changes in stimulation frequency, amplitude and pulse width in spinal cord injured animals during continuous treadmill locomotion. Electrical stimulation was delivered through L2 and S1 midline electrodes. The modulation of stimulation frequency promoted substantial and reproducible changes in the characteristics of locomotor movements. Specifically, step height and ground reaction forces were linearly modulated in response to changes in stimulation frequency (ranges from 25 – 90 Hz). The linear increase in step height could be explained by the coordinated increase in muscular amplitude with stimulation frequency (Wenger, Moraud et al 2014, in press). Contrary to stimulation frequency, amplitude and pulse width failed to induce substantial and reproducible modulations of hind limb kinematics across animals.

Next, we sought to highlight the functional relevance of these results for the recovery of locomotor function after SCI. To this aim, we designed and validated a novel real-time control system (Wenger, Martin-Moraud et al 2014, in press). The real time control system consisted of a motion tracking system (Vicon) that monitored hind limb kinematics, a multithreaded C++ code that determined the appropriate electrical stimulation features and a stimulation device that sent electrical stimulation pulses back to the animal. The computational infrastructure of the real-time control system embedded a forward model and proportional-integral feedback loop that adjusted step height during continuous locomotion. The forward model was derived from the linear regression between stimulation frequency and step height. The feedback loop served as an error correction that compensated for changes in baseline stepping and the inherent variability of step height in each individual animal.

During experimental validation we found an unexpectedly high degree of controllability of step height. Within single step cycles the animals were able to adjust their step height from the minimum to the maximum of their physiological limits. When we provided forward propulsion from a robotic device, the rats were able to adapt their hind limb trajectory to climb staircases of varied heights and lengths. Moreover, adaptive changes in stimulation frequency could double the time periods the animals were able to step continuously on the treadmill. To the best of our knowledge, this is the first time a closed-loop control system for spinal cord stimulation restored locomotion across a broad range of locomotor trajectories in paralyzed rats.

A neuroprosthetic system for spatiotemporal modulation of spinal circuits

In a final step during the PhD thesis, the multi electrode array and the real time control system were integrated to enable the stimulation of multiple electrodes at distinct locations of the spinal cord and at specific time points during the gait cycle (Wenger, Musienko, Moraud

et al 2014, in preparation). The aim was to apply spatiotemporal neuromodulation patterns that mimic the oscillating activity of spinal motor neurons pools during natural locomotion in healthy rats.

The developed stimulation algorithms tuned stimulation features through 4 independent electrode configurations promoting side-dependent movements of leg flexion and extension during continuous locomotion (L2 left and right electrodes for flexion during swing, and S1 left and right electrodes for extension during stance). The optimal timing of the onset and end of stimulation was characterized for each electrode individually. To this aim, we implemented a virtual clock that allowed precise detection of time events during the gait cycle. The time in the gait cycle could be determined from kinematics of the limb endpoint and its relative position to a virtual gravity center that was calculated from the limb endpoint trajectory for each gait cycle.

Spatiotemporal neuromodulation promoted increased activation of muscular activity in the presence of chemical stimulation. In turn, the increased muscular activity resulted in stepping patterns with clearly developed phases of extension and flexion and increased ground reaction forces during stepping in paralyzed rats.

Conclusion

The developed neuroprosthetic system allowed animals with complete spinal cord injury to perform over 1000 successive steps without failure, and to climb staircases of various heights and lengths with precision and fluidity. Spatiotemporal neuromodulation algorithms resulted in stepping patterns with clearly developed phases of extension and flexion on the left and right hind limb in rats with complete and partial spinal cord injury. Moreover, continuous electrical stimulation applied through multiple independent electrodes was able to improve stepping capacities in an alpha-synuclein rodent model of Parkinson's disease.

Current knowledge of human spinal cord properties in response to electrical stimulation suggests that the developed stimulation strategies can be translated into clinical applications to improve neurorehabilitation therapies (Wenger, Moraud et al. 2014, discussion). Moreover, the developed neuroprosthetic system can readily be interfaced with real-time control signals from the brain to design neuroprosthetic systems that establish a communication bridge between the brain and the spinal cord. This kind of cortico-spinal neuroprosthetic system heralds promise to increase activity-dependent plasticity during recovery from spinal cord injury. (Borton ... Wenger et al, 2014).

Original research articles

A computational model for epidural electrical stimulation of spinal sensorimotor circuits

Capogrosso M, Wenger N, Raspopovic S, Musienko P, Beauparlant J, Bassi Luciani L, Micera S and Courtine G. *The Journal of Neuroscience*, 2013

My contributions as second author: conducted and planned experiments to validate the computational model, conceptualizing anatomical structure of the computational model, experimental data analysis, figure preparation, writing article with main author

Closed-loop neuromodulation of spinal sensorimotor circuits controls refined locomotion after complete spinal cord injury.

Wenger N, Martin Moraud E, Raspopovic S, Bonizzato M, DiGiovanna J, Musienko P, Morari M, Micera S and Courtine G. *Science Translational Medicine* (in press)

My contributions: Main author, contributed to all aspects of the work

Translational neuroprosthetic toolbox for modulation of spinal sensorimotor circuits in space and time

Wenger N, Musienko P, Martin Moraud E, Larmagnac A, Gandar J, Micera S, Vörös J and Courtine G. *submitted*

My contributions: Main author, contributed to all aspects of the work

The original research articles are attached at the end of manuscript.

Discussion

Spinal cord model and electrode array design

We developed a computational model of the spinal cord that provides insights into the neuroanatomical structures recruited by electrical spinal cord stimulation. Therapeutic amplitude ranges of electrical stimulation primarily recruited afferent sensory fiber pathways in the spinal cord.

In previous scientific work, Rattay et al. (2000) come to a similar conclusion that spinal cord stimulation can activate large diameter afferents in the human spinal cord (34). The authors present a computational model that looks at the recruitment of sensory afferents. Intraspinal axons and anterior roots were excluded from the model since their thresholds were argued to be out of therapeutic current ranges, i.e. greater than 10 V. Neurons were not considered in the model. No experimental validations of model predictions were performed. Our spinal cord model is the first comprehensive neuroanatomical model that incorporates dorsal roots, ventral roots, intraspinal axons, interneurons and motor neurons. Additionally, through experimental validations we were able to show that electrically evoked spinal cord reflexes are mediated through monosynaptic connections of group Ia afferents and polysynaptic responses of group Ib and group II afferents. We do come to the same conclusion as previous studies regarding the recruitment of large diameter afferents fibers. However, we were able to specifically address the question whether interneurons and motor neurons are recruited by electrical stimulation.

These combined computational and experimental results were instrumental in the design of the multi electrode array. (1) Electrodes had to be placed next to the dorsal roots several segments away from the extensor and flexor motor neurons which we aimed to stimulate during locomotion. (2) We were able to reduce the number of active electrodes to a minimum of 4 stimulation sites: S1 left/right, L2 left/right. We anatomically mapped afferent fibers projecting to all lumbosacral spinal cord segments. At spinal segment S1, the roots projecting to S1, L6, L5, L4, L3 and L2 spinal segments were arranged from medial to lateral (Figure 3 Left). Consequently we understood at this spinal segment, electrodes were able to recruit the activation of multiple afferent roots. Computational and functional experiments determined the optimal location to achieve extensor pool selectivity and left right leg specificity 0.75 mm lateral from the spinal cord midline at spinal segment S1 (Figure 3 Right). At spinal segment S1 we were able to selectively recruit segments L4 to L6, which host the majority of extensor motor neuron pools to evoke distal limb extension (for anatomy compare Figure 1, introduction).

These combined considerations, make our 8 channel electrode array conceptually different from previous work. Gad et al. 2013 had proposed a high density electrode array of

27 functional electrodes distributed equally along the lumbosacral spinal cord to activate motor neuron pools directly (54). Different to this work, we answered three important conceptual questions for the design of the multi electrode array: First, which functional effect needs to be achieved by electrical stimulation? Second, where is the best anatomical location to interface electrodes to neural tissues to achieve the desired effect? And third, what is the maximum neuroanatomical and functional specificity that can be achieved by the electrical field? The answer to these questions allowed us to optimally exploit the functional selectivity of the array and to simplify the array design. Reducing to 8 functional stimulation sites, we could decrease the overall surface of the array and make the mechanical properties of the implant more flexible. Spinal cord tissue damage was avoided as a long term complication after implantation.

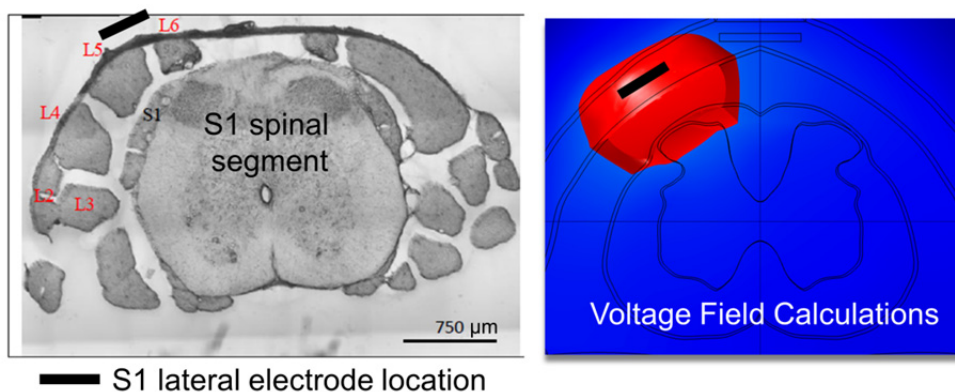


Figure 3 Multiple spinal roots can be activated at spinal segment S1. (Left) Anatomical mapping experiments reveal the relative location of dorsal roots and lateral electrode at spinal cord segment S1. (Right) Computational voltage field calculations predicted the selective recruitment of L4 to L6 spinal cord segments at therapeutic current ranges, voltage field simulations in red.

Closed loop neuromodulation and translation in human subjects

In the experimental work on closed loop neuromodulation we find that adjustment in electrical stimulation frequency achieves predictive modulations of hind limb kinematics. Changes in stimulation frequency lead to robust linear adjustments in step height.

After spinal cord injury the neural tissue below the lesions remains the capacity to modulate refined locomotor output. For example, Lovely et al. 1990 exposed cats with complete spinal cord injury to different treadmill speeds (55). The animals could adjust their gait cycle duration to the changes in speed related sensory input. The modulation of locomotor output in response to changes in speed can vary from sprinting when the treadmill is at maximum speed, to standing when the treadmill is stopped (50).

Research has identified external sources that can modulate specific aspects of locomotion. For example different serotonin receptor subtypes mediate distinct patterns of locomotion in paralyzed rats (47). 5-HT 2A/C receptor agonists promote limb extension and weight bearing capacities. 5-HT 1A and 5-HT 7 receptor agonists enhance limb flexion and the rhythmicity of the stepping pattern. Gad et al. 2013 have proposed to use a multi electrode arrays for electrical spinal cord stimulation to achieve selective muscular recruitments (54). However these results remained at observational levels. No control parameters have been identified and the modulation of hind limb kinematics has not been used for closed loop neuromodulation. In our experiments we identified linear modulation of step height as control parameter to achieve refined control of limb kinematics during continuous locomotion.

For the translation of these results in human subjects, future experiments need to address the degree of modulation that can be achieved by frequency modulation. Jilge et al. 2003 have shown that different stimulation frequencies applied at T12/L1 vertebral levels can modulate distinct aspects of stepping behaviors in human patients (56). In 5 patients with motor complete paralysis, stimulation frequencies at less than 15 Hz evoked extension movements of the lower limbs, while stimulation frequency above 25 Hz evoked stepping like activity. Future studies will need to address whether frequency modulation above 25 Hz can achieve graded muscular recruitment. Moreover, careful examination of electrode locations and adjustments of stimulation amplitudes will be necessary to translate closed loop neuromodulation strategies in patients.

Novelty of the technological platform for closed loop neuromodulation

We developed a neuroprosthetic system for spinal cord stimulation. The system is composed of a multi electrode array and a real time control system that adjust stimulation features based on movement feedback. In a first study, the system was leveraged for the design of closed loop control algorithms to restore refined control of leg movement. In a second study, spatiotemporal neuromodulation algorithms were developed that matched the natural motor circuit dynamics in healthy animals.

Previous research has established a neuroprosthetic system for intraspinal electrical stimulation (57). In this intervention, multiple metallic wires penetrate the dura mater and spinal cord tissue to position electrodes in the ventral horn of the spinal cord (58). Each electrode recruits a specific subset of motor neuron pools. Multiple electrodes are stimulated in sequence on the left and the right side to produce stepping like movements in non-paralyzed anesthetized cats (57). Kinematic movement feedback was used to determine swing and stance phases when the leg of the animal crossed a manually set threshold. The intention of the closed loop control strategies was to restore a stereotype limb endpoint trajectory that promotes functional stepping movements. Functional benefits of closed loop

intraspinal stimulation were limited. In anesthetized cats, intraspinal stimulation achieved stepping movements at 12% bodyweight support. The sequential stimulation of multiple motor neuron pools was controlled successfully in a limited number of 15 out of 30 stepping trials. Per trial the number of steps was limited to 20 consecutive gait cycles. The intervention has not been applied after spinal cord injury (57)

In contrast our real time control experiments were performed in awake paralyzed rats. We restored 60 % bodyweight support and the animals performed more than 1000 consecutive steps without failure during real time control trials. The idea to control locomotion through kinematic movement feedback is similar to the approach taken for closed loop intraspinal stimulation. However, instead of a manually set threshold, we used continuous limb endpoint trajectory to derive a detailed representation of the gait cycle. We achieved refined control of multiple locomotor trajectories that enabled rats to perform adaptive stepping patterns during continuous locomotion.

The developed technological platform for closed loop neuromodulation in rats can readily be translated for human subjects. For this purpose, industrial development of clinical closed loop stimulation platforms provide the appropriate neurotechnology to incorporate adaptive spinal cord stimulation algorithms (59). Wearable and implantable motion sensors could generate the necessary feedback to incorporate automated closed-loop control policies into neuromodulation therapies for use outside laboratory environments (60).

Detailed contributions of the candidate

The design and development of a neuroprosthetic system is an integrated and interdisciplinary process. During my PhD, I worked independently on the concept of a neuroprosthetic system for spinal cord stimulation with the help and guidance of my supervisor Prof. Grégoire Courtine. I investigated anatomical structures of the spinal cord and I established functional mapping experiments for spatial and temporal selectivity of electrical spinal cord stimulation. I characterized the modulation of hind limb kinematics during real time adjustments of stimulation features in paralyzed rats. I performed experimental validations, surgical interventions, neurophysiological data analysis, program coding, figure preparation, project coordination and manuscript preparations. The author contributions can also be found at the end of each research article. For specific aspects in the development of the neuroprosthetic system, I collaborated with partners in the engineering sciences. My contributions to these collaborative aspects of the work are specified below. I am particularly grateful for the opportunity to have work in an interdisciplinary and very cooperative environment. The final, fully operational neuroprosthetic system to restore locomotion after neuromotor disorders could only be achieved in collaborations.

Concept and validation of the computational spinal cord model

The developed computational model of the spinal cord has the remarkable capacity to predict experimental results of electrical spinal cord stimulation. The predictions are achieved by incorporating the electrical properties of spinal cord tissues and arranging them in an anatomically realistic computational model. Marco Capogrosso, a PhD student at Scuola Superiore Santa Anna, Pisa, Italy, with a background in Physics developed the computational model. He worked on voltage field simulations and performed all the mathematical computations that were necessary to predict the activation of neural structures. My conceptual contributions to the computational work remain at the level of spinal cord anatomy. I have provided literature on the distribution of neural structures, interneurons and motor neurons and I have suggested incorporating the detailed arrangement of afferent sensory fiber pathways that run in the subdural space outside the spinal cord.

My main contribution to work was the experimental validation of the model predictions. I provided experimental concepts how to demonstrate the recruitment of different fiber pathways and neural structures. Achilles tendon vibration and frequency dependent reflex suppression were used to block all proprioceptive afferent fiber pathways (group Ia, Ib and group II sensory afferents). Tizanidine, an alpha-2 adrenergic antagonist, was used to block group Ib and group II afferent fiber pathways at their polysynaptic connection onto interneurons. Tetrodotoxin, a sodium channel blocker, was used to block all neural cell bodies in the spinal cord permitting the selective recruitment of motor axons only. These mechanical and pharmacological interventions allowed validation of the prediction that epidural electrical stimulation primarily recruits afferent fiber pathways in the spinal cord.

I performed chronic experiments in rats with complete spinal cord injury to demonstrate the effect of unilateral spinal cord stimulation. S1 lateral electrodes could achieve unilateral limb movements during dynamic stepping conditions in paralyzed animals. These experiments were important to demonstrate that the selective recruitment of unilateral fiber pathways results in functional stepping movements. I analyzed experimental data, prepared figures, and participated in the manuscript preparation with the main author and my supervisor.

Fabrication and optimization of multi electrode arrays

In the European FP 7 project NEUWALK, our partners from the Institute for Microtechnology Mainz (IMM), Germany, worked on the fabrication of the multi electrode arrays for spinal cord stimulation in rats. The realization of the final implants was a long and tedious development process. The first arrays for implantation in rats arrived in March 2010. The first implant that lasted chronically in rats to allow functional experiments was developed only three years later in October 2013. During this 3 years period, all of the electrodes had failed soon after

implantation. Several biological adaptations had to be made to the implant shape, the implant location and the material in order to achieve chronic electrode stability in vivo.

The implant design was iteratively updated based on in vivo implantations in healthy animals. During the 3 years development process my colleague, Dr. Pavel Musienko, a specialized animal surgeon from the Pavlov Institute of Physiology in St. Petersburg implanted the rats. After implantation I routinely monitored the electrodes performance and electrode impedances for a period of 9 weeks. Once the electrodes failed, I performed anatomical dissections and CT scans to report on the anatomical failure analysis.

Several milestones were achieved towards the chronic electrode stability. (1) When bending the animals during dissections, we found that the implants slide and break at the entry into the vertebral canal (Figure **4A**). Here, the implant was in direct contact with the sharp edges of the vertebral bone (Figure **4C**). In order to stabilize the vertebrae at the entry point we conceptualized a vertebral prosthesis that stabilized the vertebrae with metallic screws and dental cement (Figure **4C**). (2) Anatomical dissections showed that the implant compressed and damaged the soft spinal cord tissue inside the vertebral canal. The shape of the implant was rectangular and rigid. Together with IMM we decided to change the shape of the implant to maximally reduce its surface. The final implant had a fishbone like structure that increased the flexibility of the polyamide implant (fishbone shape see Figure 2, introduction). (3) CT Scans revealed that a subcutaneous loop that was initially placed to allow adaptive motion of the implant resulted in a focal 180 degree bend (Figure **4B**). This deformation prevented any movement of the array and caused cracks in the conductive electrode leads. We decided to remove the stress release loop, shortened the electrode array and positioned the connector directly at the entry of the implant in the vertebral canal. (4) Implants were breaking at the connector, specifically at the interface of metallic wires and polyimide array. To stabilize this connection, we decided to cover the entire connector in dental cement (Figure **4D**). Consequently, metallic wires, polyamide implant and vertebral bone were immobilized with respect to each other through the prosthesis.

In conclusion, we were able to develop a chronically stable multi electrode array for spinal cord stimulation. In a multistep procedure we adapted the design and properties of the implant to accommodate to the challenging anatomical environment of the rat spinal cord.

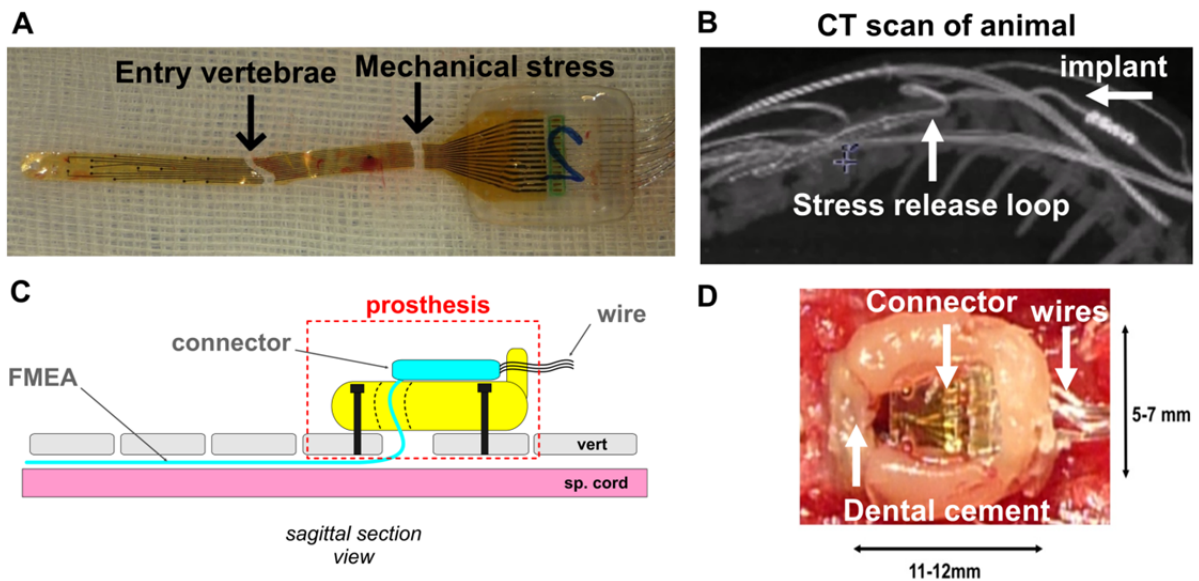


Figure 4 Trouble shooting to achieve chronic stability of multi electrode array in vivo. (A) Cracks in the implant were identified after 3 weeks of implantation in healthy rats. One crack occurred at the entry of the implant into the vertebral canal; another crack resulted from the mechanical stress the animal exerted during natural locomotion in the home cage. (B) A CT-Scan of the multi electrode in vivo revealed that a stress release loop resulted in a 180 degree bend. The implant was redesigned, shortened and the stress release loop was removed in consequent implantations. (C) A vertebral prosthesis stabilized the flexible multi electrode array (FMEA) with respect to the vertebral bone (vert.). Metallic screws in black, dental cement in yellow. (D) Photograph of the vertebral prosthesis in vivo. Dental cement stabilized array connector and metallic wires to avoid failure of their connection.

Development of real time control algorithms

Before my PhD thesis, I worked one year in Prof. Courtine's laboratory as a master student in Neuroinformatics at ETH Zurich. During this time, I coded a first version of the real time control system that was later extended to incorporate closed loop control algorithms. I implemented a multithread C++ program and a user interface that allowed automated adjustments of stimulation features triggered from real time feedback of muscular signals. During my PhD, this real time platform has been extended to integrate a proportional-integral (PI) controller that adjusted stimulation features based on movement feedback. My colleague Eduardo Martin Moraud, a PhD student at ETH Zurich, with a background in automatic control worked on the implementation of the PI controller.

During the PhD thesis, I performed functional mapping experiments to identify reproducible modulations of hind limb kinematics in paralyzed rats. Step height emerged as the primary target for closed loop control. Based on the linear regression between stimulation frequency and step height, we could derive a forward model for the control algorithms. Together with Eduardo, I worked on the conceptualization of the control structure and the

functional experiments to assess the performance of the code. When the closed loop control was implemented, we worked together on a daily basis in experiments to validate the controllability and functional benefits of closed loop spinal cord stimulation in paralyzed rats. I analyzed functional and neurophysiological data and I programmed automated Matlab routines for the analysis of muscular reflex responses during stepping. The final manuscript on closed loop control of spinal cord stimulation was conceived as an equally contributed work.

Outlook

Closed loop neuromodulation significantly improved stepping capacities in rats with complete and partial spinal cord injuries. The newly developed stimulation strategies were tested on their assistive effect on locomotor function. Future studies need to address whether the newly developed stimulation strategies can increase the amount of plasticity across the spinal cord lesion. These investigations will be important to define the potential of closed loop spinal cord stimulation to improve long lasting rehabilitation after spinal cord injury. Our stimulation strategies aim to reactivate spinal sensorimotor circuits below the level of the lesion. Continuous stimulation of the spinal cord in combination with overground training was able to increase the amount of supraspinal connections across an incomplete spinal cord lesion (51). By the principle of hebbian plasticity, neural connections can be strengthened by the coordinated activity of presynaptic and postsynaptic neural activity. Recent investigations have shown the potential of deep brain stimulation to improve recovery after spinal cord injury (61). Potentially the combination of spinal cord stimulation and deep brain stimulation could further improve the capacity of neuromodulation strategies for recovery after spinal cord injury.

Our investigations identified a set of four electrodes that were optimal to reproduce the activity of flexor and extensor motor neuron pools during gait. These results were based on the maximum specificity that can be achieved with monopolar voltage fields. A single electrode was able to recruit a specific subset of dorsal roots. It remains an open question whether spinal cord stimulation could be more specific. Our multi electrode arrays provide an immediate opportunity to investigate the effect of multipolar voltage fields in their ability to recruit individual dorsal roots. Moreover, it remains to be addressed whether more specific spinal cord stimulation can improve the recovery after spinal cord injury.

Acknowledgments

I would like to thank my supervisor Prof Gregoire Courtine for his dedicated guidance throughout my PhD. His energy and enthusiasm about research and science has been truly inspirational. I share the believe that the research and the translational efforts in our laboratory will have a substantial impact on neuro-rehabilitation strategies and future healthcare.

I want to thank the all the members of the G-Lab. Many of my colleagues have become true friends over the years. Specifically, I want thank Eduardo Martin Moraud for the countless hours spent together in the experimental room, the discussions and writing sessions. Besides his intellectual skills, I value him for his kind, insightful and supportive character. I want to thank Marco Capogrosso for the many discussions over the years. Marco brought a true sense of philosophy to our research. Moreover, I thank Stanisa Raspopovic and Marco Bonizzato for their invaluable contributions to the characterization and the first demonstration of real time control of spinal cord stimulation.

I want to thank my family, my parents Anna and Ernst and my sister Lola for their continuous support and I would like to dedicate this work to my grandmother Amanda Klammer. Thank you for all the support, the sweets and prayers.

‘Wichtig ist, dass man es schafft’

Amanda Klammer

Bibliography

1. Y. A. T. IWAHARA, E. GARCIA-RILL AND R. D. SKINNER, Spinal Cord Stimulation-Induced Locomotion in the Adult Cat. *Brain Research Bulletin*, Vol. 28, pp. 99-105, (1991).
2. M. Capogrosso *et al.*, A computational model for epidural electrical stimulation of spinal sensorimotor circuits. *The Journal of neuroscience : the official journal of the Society for Neuroscience* **33**, 19326 (Dec 4, 2013).
3. M. Wyndaele, J. J. Wyndaele, Incidence, prevalence and epidemiology of spinal cord injury: what learns a worldwide literature survey? *Spinal cord* **44**, 523 (Sep, 2006).
4. The National SCI Statistical Center. Facts and figures at a glance. Birmingham: University of Alabama.
5. J. W. McDonald *et al.*, Late recovery following spinal cord injury. Case report and review of the literature. *Journal of neurosurgery* **97**, 252 (Sep, 2002).
6. A. Ackery, C. Tator, A. Krassioukov, A global perspective on spinal cord injury epidemiology. *J Neurotrauma* **21**, 1355 (Oct, 2004).
7. I. G. Fiedler, P. W. Laud, D. J. Maiman, D. F. Apple, Economics of managed care in spinal cord injury. *Archives of physical medicine and rehabilitation* **80**, 1441 (Nov, 1999).
8. M. S. Ramer, G. P. Harper, E. J. Bradbury, Progress in spinal cord research - a refined strategy for the International Spinal Research Trust. *Spinal cord* **38**, 449 (Aug, 2000).
9. C. H. Tator, E. G. Duncan, V. E. Edmonds, L. I. Lapczak, D. F. Andrews, Complications and costs of management of acute spinal cord injury. *Paraplegia* **31**, 700 (Nov, 1993).
10. K. D. Anderson, Targeting recovery: priorities of the spinal cord-injured population. *J Neurotrauma* **21**, 1371 (Oct, 2004).
11. D. G. Tate, C. Z. Kalpakjian, M. B. Forchheimer, Quality of life issues in individuals with spinal cord injury. *Archives of physical medicine and rehabilitation* **83**, S18 (Dec, 2002).
12. G. Courtine *et al.*, Can experiments in nonhuman primates expedite the translation of treatments for spinal cord injury in humans? *Nature medicine* **13**, 561 (May, 2007).
13. S. J. Harkema *et al.*, Locomotor training: as a treatment of spinal cord injury and in the progression of neurologic rehabilitation. *Archives of physical medicine and rehabilitation* **93**, 1588 (Sep, 2012).
14. G. S. Sapkas, S. A. Papadakis, Neurological outcome following early versus delayed lower cervical spine surgery. *Journal of orthopaedic surgery* **15**, 183 (Aug, 2007).
15. C. S. Sherrington, Flexion-reflex of the limb, crossed extension-reflex, and reflex stepping and standing. *The Journal of physiology* **40**, 28 (Apr 26, 1910).

16. T. G. Brown, The Intrinsic Factors in the Act of Progression in the Mammal. *Proceedings of the Royal Society of London. Series B, Containing Papers of a Biological Character*, (1911).
17. S. Grillner, P. Zangger, On the central generation of locomotion in the low spinal cat. *Experimental brain research. Experimentelle Hirnforschung. Experimentation cerebrale* **34**, 241 (Jan 15, 1979).
18. O. Kiehn, Locomotor circuits in the mammalian spinal cord. *Annual review of neuroscience* **29**, 279 (2006).
19. O. Kiehn *et al.*, Excitatory components of the mammalian locomotor CPG. *Brain research reviews* **57**, 56 (Jan, 2008).
20. M. Hubli, V. Dietz, The physiological basis of neurorehabilitation--locomotor training after spinal cord injury. *Journal of neuroengineering and rehabilitation* **10**, 5 (2013).
21. H. Barbeau, S. Rossignol, Recovery of locomotion after chronic spinalization in the adult cat. *Brain research* **412**, 84 (May 26, 1987).
22. V. R. Edgerton, N. J. Tillakaratne, A. J. Bigbee, R. D. de Leon, R. R. Roy, Plasticity of the spinal neural circuitry after injury. *Annual review of neuroscience* **27**, 145 (2004).
23. V. R. Edgerton *et al.*, Retraining the injured spinal cord. *The Journal of physiology* **533**, 15 (May 15, 2001).
24. V. R. Edgerton *et al.*, Training locomotor networks. *Brain research reviews* **57**, 241 (Jan, 2008).
25. N. J. Tillakaratne *et al.*, Use-dependent modulation of inhibitory capacity in the feline lumbar spinal cord. *The Journal of neuroscience : the official journal of the Society for Neuroscience* **22**, 3130 (Apr 15, 2002).
26. N. J. Tillakaratne *et al.*, Increased expression of glutamate decarboxylase (GAD(67)) in feline lumbar spinal cord after complete thoracic spinal cord transection. *Journal of neuroscience research* **60**, 219 (Apr 15, 2000).
27. V. Dietz, Good clinical practice in neurorehabilitation. *The Lancet. Neurology* **5**, 377 (May, 2006).
28. A. Wernig, S. Muller, Laufband locomotion with body weight support improved walking in persons with severe spinal cord injuries. *Paraplegia* **30**, 229 (Apr, 1992).
29. V. Dietz, G. Colombo, L. Jensen, Locomotor activity in spinal man. *Lancet* **344**, 1260 (Nov 5, 1994).
30. H. Barbeau, M. Ladouceur, K. E. Norman, A. Pepin, A. Leroux, Walking after spinal cord injury: evaluation, treatment, and functional recovery. *Archives of physical medicine and rehabilitation* **80**, 225 (Feb, 1999).
31. A. L. Behrman, S. J. Harkema, Locomotor training after human spinal cord injury: a series of case studies. *Physical therapy* **80**, 688 (Jul, 2000).

32. B. Dobkin *et al.*, The evolution of walking-related outcomes over the first 12 weeks of rehabilitation for incomplete traumatic spinal cord injury: the multicenter randomized Spinal Cord Injury Locomotor Trial. *Neurorehabilitation and neural repair* **21**, 25 (Jan-Feb, 2007).
33. V. Dietz, S. Grillner, A. Trepp, M. Hubli, M. Bolliger, Changes in spinal reflex and locomotor activity after a complete spinal cord injury: a common mechanism? *Brain : a journal of neurology* **132**, 2196 (Aug, 2009).
34. F. Rattay, K. Minassian, M. R. Dimitrijevic, Epidural electrical stimulation of posterior structures of the human lumbosacral cord: 2. quantitative analysis by computer modeling. *Spinal cord* **38**, 473 (Aug, 2000).
35. I. Lavrov *et al.*, Epidural stimulation induced modulation of spinal locomotor networks in adult spinal rats. *The Journal of neuroscience : the official journal of the Society for Neuroscience* **28**, 6022 (Jun 4, 2008).
36. J. P. Hunter, P. Ashby, Segmental effects of epidural spinal cord stimulation in humans. *The Journal of physiology* **474**, 407 (Feb 1, 1994).
37. G. Barolat *et al.*, Epidural spinal cord stimulation in the management of spasms in spinal cord injury: a prospective study. *Stereotactic and functional neurosurgery* **64**, 153 (1995).
38. M. R. Dimitrijevic, Y. Gerasimenko, M. M. Pinter, Evidence for a spinal central pattern generator in humans. *Annals of the New York Academy of Sciences* **860**, 360 (Nov 16, 1998).
39. Y. P. Gerasimenko, A. N. Makarovskii, O. A. Nikitin, Control of locomotor activity in humans and animals in the absence of supraspinal influences. *Neuroscience and behavioral physiology* **32**, 417 (Jul-Aug, 2002).
40. S. Harkema *et al.*, Effect of epidural stimulation of the lumbosacral spinal cord on voluntary movement, standing, and assisted stepping after motor complete paraplegia: a case study. *The Lancet* **377**, 1938 (2011).
41. K. Minassian *et al.*, Human lumbar cord circuitries can be activated by extrinsic tonic input to generate locomotor-like activity. *Human movement science* **26**, 275 (Apr, 2007).
42. R. Herman, J. He, S. D'Luzansky, W. Willis, S. Dilli, Spinal cord stimulation facilitates functional walking in a chronic, incomplete spinal cord injured. *Spinal cord* **40**, 65 (Feb, 2002).
43. M. R. Carhart, J. He, R. Herman, S. D'Luzansky, W. T. Willis, Epidural spinal-cord stimulation facilitates recovery of functional walking following incomplete spinal-cord injury. *IEEE transactions on neural systems and rehabilitation engineering : a publication of the IEEE Engineering in Medicine and Biology Society* **12**, 32 (Mar, 2004).
44. H. Huang, J. He, R. Herman, M. R. Carhart, Modulation effects of epidural spinal cord stimulation on muscle activities during walking. *IEEE transactions on neural systems and rehabilitation engineering : a publication of the IEEE Engineering in Medicine and Biology Society* **14**, 14 (Mar, 2006).

45. C. A. Angeli, V. R. Edgerton, Y. P. Gerasimenko, S. J. Harkema, Altering spinal cord excitability enables voluntary movements after chronic complete paralysis in humans. *Brain : a journal of neurology* **137**, 1394 (May, 2014).
46. V. R. Edgerton, S. Harkema, Epidural stimulation of the spinal cord in spinal cord injury: current status and future challenges. *Expert review of neurotherapeutics* **11**, 1351 (Oct, 2011).
47. P. Musienko *et al.*, Controlling specific locomotor behaviors through multidimensional monoaminergic modulation of spinal circuitries. *The Journal of neuroscience : the official journal of the Society for Neuroscience* **31**, 9264 (Jun 22, 2011).
48. B. J. Schmidt, L. M. Jordan, The role of serotonin in reflex modulation and locomotor rhythm production in the mammalian spinal cord. *Brain research bulletin* **53**, 689 (Nov 15, 2000).
49. R. M. Ichiyama *et al.*, Dose dependence of the 5-HT agonist quipazine in facilitating spinal stepping in the rat with epidural stimulation. *Neuroscience letters* **438**, 281 (Jun 27, 2008).
50. G. Courtine *et al.*, Transformation of nonfunctional spinal circuits into functional states after the loss of brain input. *Nature neuroscience* **12**, 1333 (Oct, 2009).
51. R. van den Brand *et al.*, Restoring voluntary control of locomotion after paralyzing spinal cord injury. *Science* **336**, 1182 (Jun 1, 2012).
52. E. Lu, Yong, Modaber, Morikawa, Anaya, Zdunowski, Roy, Gerasimenko, in *Annual Meeting of the Society for Neuroscience, San Diego 2013*. (2013).
53. J. P. Rauschecker, R. V. Shannon, Sending sound to the brain. *Science* **295**, 1025 (Feb 8, 2002).
54. P. Gad *et al.*, Development of a multi-electrode array for spinal cord epidural stimulation to facilitate stepping and standing after a complete spinal cord injury in adult rats. *Journal of neuroengineering and rehabilitation* **10**, 2 (2013).
55. R. G. Lovely, R. J. Gregor, R. R. Roy, V. R. Edgerton, Weight-bearing hindlimb stepping in treadmill-exercised adult spinal cats. *Brain research* **514**, 206 (Apr 30, 1990).
56. B. Jilge *et al.*, Initiating extension of the lower limbs in subjects with complete spinal cord injury by epidural lumbar cord stimulation. *Experimental brain research. Experimentelle Hirnforschung. Experimentation cerebrale* **154**, 308 (Feb, 2004).
57. B. J. Holinski, K. A. Mazurek, D. G. Everaert, R. B. Stein, V. K. Mushahwar, Restoring stepping after spinal cord injury using intraspinal microstimulation and novel control strategies. *Conference proceedings : ... Annual International Conference of the IEEE Engineering in Medicine and Biology Society. IEEE Engineering in Medicine and Biology Society. Conference* **2011**, 5798 (2011).
58. J. A. Bamford, K. G. Todd, V. K. Mushahwar, The effects of intraspinal microstimulation on spinal cord tissue in the rat. *Biomaterials* **31**, 5552 (Jul, 2010).
59. P. Afshar *et al.*, A translational platform for prototyping closed-loop neuromodulation systems. *Frontiers in neural circuits* **6**, 117 (2012).

60. B. Mariani, S. Rochat, C. J. Bula, K. Aminian, Heel and toe clearance estimation for gait analysis using wireless inertial sensors. *IEEE Trans Biomed Eng* **59**, 3162 (Nov, 2012).
61. L. C. Bachmann *et al.*, Deep brain stimulation of the midbrain locomotor region improves paretic hindlimb function after spinal cord injury in rats. *Science translational medicine* **5**, 208ra146 (Oct 23, 2013).

A Computational Model for Epidural Electrical Stimulation of Spinal Sensorimotor Circuits

Marco Capogrosso,^{1,2} Nikolaus Wenger,³ Stanisa Raspopovic,^{1,2} Pavel Musienko,^{3,4} Janine Beauparlant,³ Lorenzo Bassi Luciani,¹ Grégoire Courtine,^{3*} and Silvestro Micera^{1,2*}

¹The BioRobotics Institute, Scuola Superiore Sant'Anna, Pisa, Italy, ²Translational Neural Engineering Laboratory, Center for Neuroprosthetics and Institute for Bioengineering, School of Engineering, Swiss Federal Institute of Technology (EPFL), Lausanne, Switzerland, ³International Paraplegic Foundation Chair in Spinal Cord Repair, Center for Neuroprosthetics and Brain-Mind Institute, Swiss Federal Institute of Technology (EPFL), Lausanne, Switzerland, and ⁴Pavlov Institute of Physiology, St. Petersburg, Russia

Epidural electrical stimulation (EES) of lumbosacral segments can restore a range of movements after spinal cord injury. However, the mechanisms and neural structures through which EES facilitates movement execution remain unclear. Here, we designed a computational model and performed *in vivo* experiments to investigate the type of fibers, neurons, and circuits recruited in response to EES. We first developed a realistic finite element computer model of rat lumbosacral segments to identify the currents generated by EES. To evaluate the impact of these currents on sensorimotor circuits, we coupled this model with an anatomically realistic axon-cable model of motoneurons, interneurons, and myelinated afferent fibers for antagonistic ankle muscles. Comparisons between computer simulations and experiments revealed the ability of the model to predict EES-evoked motor responses over multiple intensities and locations. Analysis of the recruited neural structures revealed the lack of direct influence of EES on motoneurons and interneurons. Simulations and pharmacological experiments demonstrated that EES engages spinal circuits trans-synaptically through the recruitment of myelinated afferent fibers. The model also predicted the capacity of spatially distinct EES to modulate side-specific limb movements and, to a lesser extent, extension versus flexion. These predictions were confirmed during standing and walking enabled by EES in spinal rats. These combined results provide a mechanistic framework for the design of spinal neuroprosthetic systems to improve standing and walking after neurological disorders.

Key words: computational model; electrical epidural stimulation; finite element model; spinal cord injury; spinal cord stimulation; spinal reflexes

Introduction

Epidural electrical stimulation (EES) of the spinal cord has been used for >40 years to alleviate chronic pain syndromes (Mailis-Gagnon et al., 2004). However, the therapeutic potential of EES may not be limited to pain treatment. There is growing evidence that EES may also contribute to improving motor execution and recovery after spinal cord injury (SCI; Harkema et al., 2011), Parkinson's disease (PD; Fuentes et al., 2009; Fénelon et al., 2012), multiple sclerosis (MS; Illis et al., 1976), and possibly other neurological disorders affecting descending control systems (Minassian et al., 2012; Musienko et al., 2012).

Over the past decade, a series of studies firmly established that EES applied over the dorsal aspect of lumbosacral segments promotes weight-bearing standing and stepping-like movements in experimental animals and humans with severe SCI (Minassian et al., 2004; Ichiyama et al., 2005; Harkema et al., 2011; Lyalka et al., 2011). Recent experiments showed that EES is also capable of enabling functional interactions between residual descending connections and spinal circuits. Together with rehabilitation, EES restored supraspinal control over joint-specific movements in motor-complete paraplegic patients (Harkema et al., 2011), as well as refined locomotion when combined with pharmacological modulations and robot-assisted training in paralyzed rats (van den Brand et al., 2012).

The neurotechnology and EES protocols for sensorimotor therapeutic applications are at the early stages of development (Edgerton and Harkema, 2011). Experimental and clinical studies conducted in subjects with SCI, MS, or PD used wire electrodes (Musienko et al., 2009) or electrode arrays designed for pain treatment (Harkema et al., 2011; Fénelon et al., 2012). Empirical knowledge and visual observations have guided electrode positioning, as well as the selection of electrode configurations and stimulation parameters. Extensive mappings revealed that each electrode location, electrode configuration,

Received April 22, 2013; revised Oct. 28, 2013; accepted Oct. 30, 2013.

Author contributions: M.C., G.C., and S.M. designed research; M.C., N.W., S.R., P.M., J.B., L.B.L., and G.C. performed research; M.C., N.W., S.R., J.B., G.C., and S.M. analyzed data; M.C., G.C., and S.M. wrote the paper.

*G.C. and S.M. contributed equally.

The authors declare no competing financial interests.

This work was supported by a Starting Grant from the European Research Council (ERC 261247, Walk Again), the European Community's Seventh Framework Program (CP-IP 258654, NeuWALK), and funding from the NanoTera.ch program of the Swiss National Science Foundation (SpineRepair).

Correspondence should be addressed to Dr. Grégoire Courtine, International Paraplegic Foundation Chair in Spinal Cord Repair, EPFL SV UPCOURTINE - station 19, Swiss Federal Institute of Technology, 1015 Lausanne, Switzerland. E-mail: gregoire.courtine@epfl.ch.

DOI:10.1523/JNEUROSCI.1688-13.2013

Copyright © 2013 the authors 0270-6474/13/3319326-15\$15.00/0

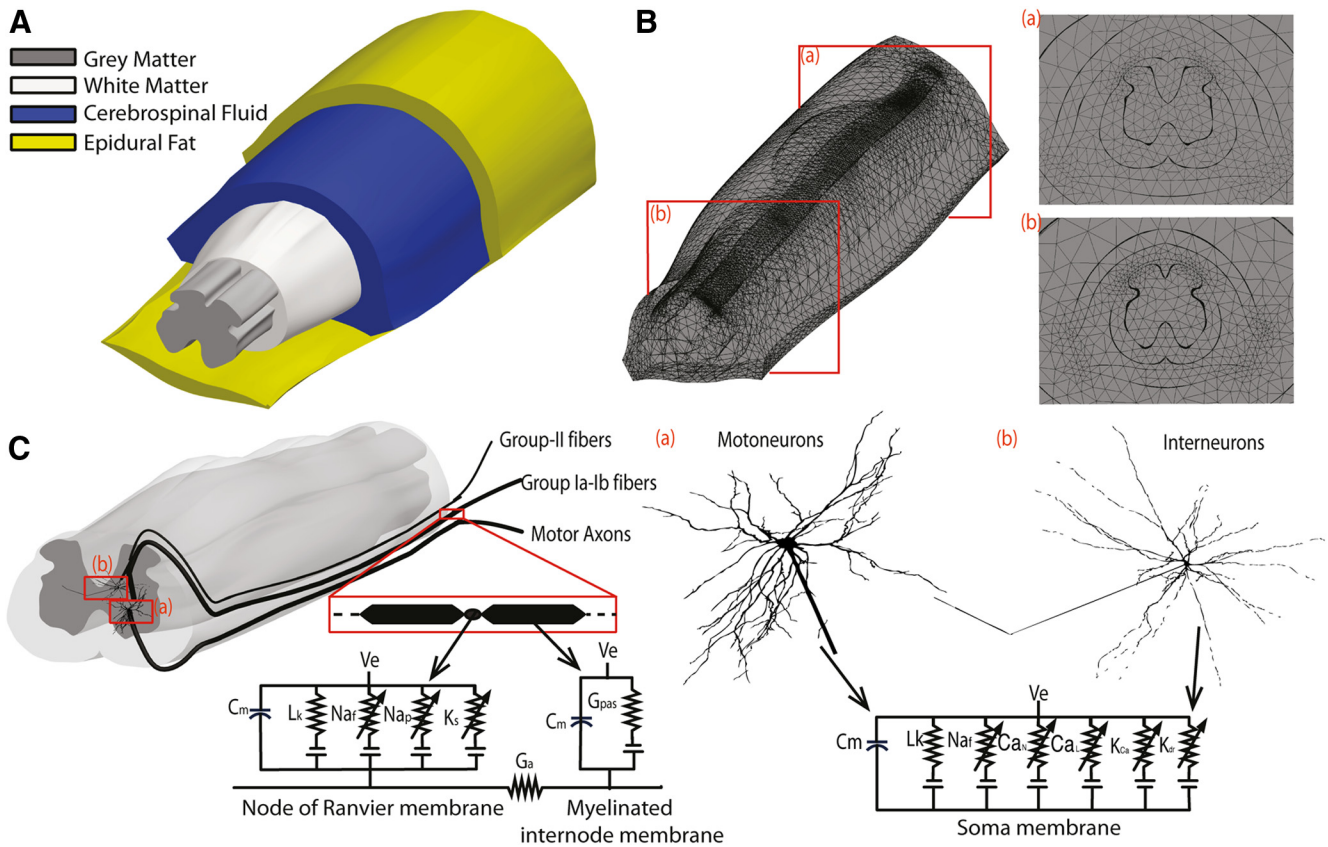


Figure 1. Characteristics of the computational model. **A**, Anatomically realistic volume conductor model with explicit, color-coded representation of the gray and white matter, CSF, and epidural fat. **B**, Meshing of the FEM structure with tetrahedral elements, and cross sections of spinal segments L2 (**a**) and S1 (**b**). **C**, Axon cable model of afferent and efferent fibers with realistic geometrical representation of efferent and afferent fibers, alpha motoneurons, and interneurons. Membrane potentials were calculated through Hodgkin–Huxley equations. Afferent fibers entered the spinal cord below the spinal segment S1 and ran longitudinally before bending in the gray matter of their target segment, as depicted in the pictorial representation. Interneurons were located in laminae I–III and VII, with efferent axons expanding dorsoventrally, or crossing the spinal cord midline, respectively. Alpha motoneurons were located based on our anatomical evaluations (Fig. 2). Their efferent axons ran longitudinally toward the S1 segment before exiting the spinal cord.

and stimulation parameter modulates specific aspects of standing, stepping, and isolated movements (Minassian et al., 2004; Courtine et al., 2009; Harkema et al., 2011; Lyalka et al., 2011). This labor-intensive, empirical approach is necessarily suboptimal and impractical for elaborating efficient EES protocols. These experiments emphasize the need to establish a mechanistic framework that will steer the development of spinal neuroprosthetic systems, and will support the design of optimal EES paradigms to facilitate movement in motor-impaired subjects.

The mechanisms and neural structures through which EES enables motor control remain unclear. Computational models (Struijk et al., 1992; Ladenbauer et al., 2010) and electrophysiological studies (Gerasimenko et al., 2006; Minassian et al., 2007) suggested that EES primarily recruits proprioceptive afferent fibers in the dorsal roots and along their course in the dorsal column, but a direct action of EES onto interneurons has also been proposed (Lavrov et al., 2006; Edgerton and Harkema, 2011). Here, we developed a hybrid computational model of EES that we validated comprehensively. We demonstrate the value of the model to (1) identify the fibers and circuits recruited by EES, (2) characterize the degree of EES selectivity, and (3) predict optimal electrode positioning to facilitate specific movements during EES-elicited standing and walking in spinal rats.

Materials and Methods

Hybrid computational model

We aimed to design a hybrid computational model combining (1) a 3D finite element method (FEM) to characterize the electric potential and currents generated by EES, and (2) a geometrically realistic biophysical model of spinal sensorimotor circuits to identify the type of neurons, fibers, and circuits recruited by EES-induced electrical fields and currents.

3D finite element model. Using 3D FEM, we elaborated an anatomically and electrically realistic volume conductor model of the rat lumbosacral spinal cord (Fig. 1A,C). Spinal cord geometry was derived from anatomical data taken from the rat spinal cord atlas (Reeve and Reeve, 2008) and in the rats used in our experiments (Lewis; Centre d'Élevage Janvier, Le Genest-Saint-Isle, France). To delimitate the borders of the gray and white matter, we stained 40- μm -thick coronal sections with NeuN antibodies (Fig. 2A). A histological picture for each segment comprised between L2 and S1 was segregated into white and gray matter compartments using the software ImageJ and the toolbox NeuronJ (<http://rsb.info.nih.gov/ij/>). We used Pro/ENGINEER Wildfire 5.0 to interpolate adjacent 2D segment representations into a full 3D model of lumbosacral segments. The length of each spinal segment was derived from our experimental data. The total length of the modeled structure reached 15.5 mm. The CSF and epidural spaces were designed from pictorial representations of the cord (Coburn, 1985). The vertebrae were modeled as elliptic bony structures surrounding the spinal cord. Table 1 reports the features and specific conductivity values for each of the modeled structures. The thin dura mater presents a conductivity of the same order of

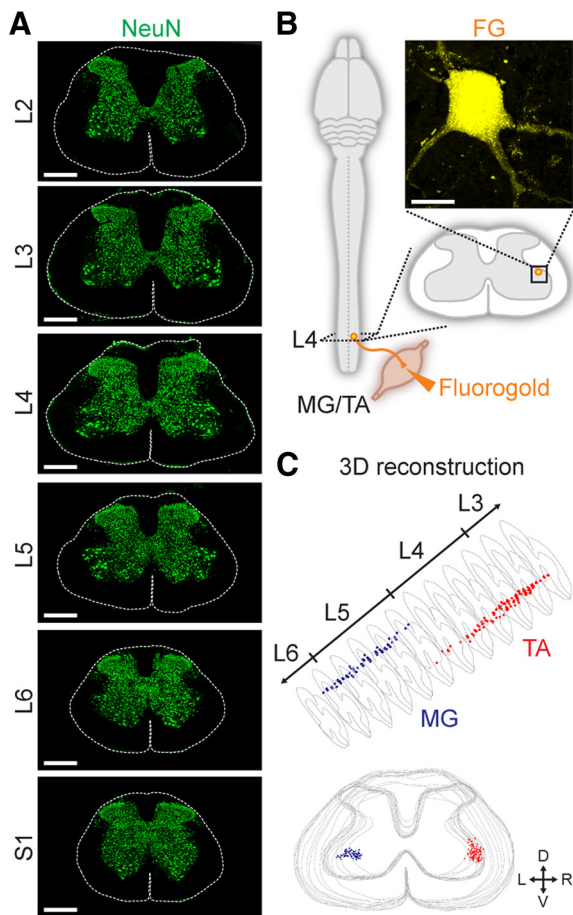


Figure 2. Anatomical features implemented in the computational model. **A**, Neuronal nuclei (NeuN) staining revealing the shape of the gray matter along the rostrocaudal extent of the lumbo-sacral spinal cord. Scale bar, 500 μm . **B**, The retrograde tracer Fluorogold (FG) was injected into the medial gastrocnemius (MG, ankle extensor) and the tibialis anterior (TA, ankle flexor) muscles to label MG and TA motoneurons, respectively ($n = 3$ rats). Scale bar, 30 μm . **C**, The 3D location of MG (blue) and TA (red) motoneurons was evaluated based on the analysis of serial spinal cord sections in the software NeuroLucida. Angled and cross-sectional projections of the reconstructed motoneuron columns are shown. D, Dorsal; V, ventral; L, left; R, right.

Table 1. Values of tissue conductivity implemented in the computational model

Tissue	Conductivity (S/m)
White matter	0.6 longitudinal/0.083 transversal
Grey matter	0.23 isotropic
Epidural fat	0.04 isotropic
CSF	1.7 isotropic
Vertebral bone	0.02 isotropic
Saline	2 isotropic
Teflon wire	$1e^{-23}$ isotropic

Conductivity is scalar for isotropic tissues; the conductivity tensor is diagonal in the reference frame of the tissue (Ladenbauer et al., 2010).

magnitude as the epidural fat, which is <3% compared with the high CSF conductivity (Rattay et al., 2000). As a consequence, the drop of voltage across the dura primarily results from the difference between CSF and the epidural fat conductivities. Therefore, as in previous studies (McIntyre and Grill, 2002; Ladenbauer et al., 2010), we did not model the thin dura mater in our computational model.

Simulation of EES in the FEM model. EES was delivered through micro-wire electrodes, which we modeled as active sites of 1 mm in length, as used in rats to facilitate stepping (Courtine et al., 2009). We positioned EES electrodes on the dorsal aspect of spinal segments L2, L4, and S1, which have been the primary and more effective sites to facilitate move-

ment execution in rats (Musienko et al., 2009) and humans (Harkema et al., 2011) with SCI. The electrodes were placed at the midline, or at various mediolateral positions. A current source of unitary amplitude was placed at the surface of the active part of the electrode. The electrical potential was obtained by means of the quasi-static approximation of the Maxwell Equations, which we expressed through a Laplace formulation:

$$\nabla \cdot \sigma \nabla V_e = 0 \quad (1)$$

with Dirichlet boundary conditions set at the outermost boundaries of the model:

$$V_e(\delta\Omega) = 0, \quad (2)$$

where $\delta\Omega$ is the outermost surface (saline) of the model.

Equation 2 is an approximation of the ground condition at infinity. To approximate this condition into a finite model, we placed a saline conductor around the spinal cord (McIntyre and Grill, 2002; Schiefer et al., 2008; Raspopovic et al., 2011). We also prolonged the overall length of the structure at the rostral (L2) and caudal (S1) extremities by 2 cm.

We used established conductivity values to characterize each modeled tissue (Table 1; Ladenbauer et al., 2010), while ensuring proper continuity conditions at each boundary. A nonuniform, second-order tetrahedral mesh consisting of $\sim 900,000$ elements (~ 1.2 million degrees of freedom) was generated for the discretization of the model. The model was implemented into COMSOL 3.5a. Simulations were performed with a 2.8 GHz Intel i7 quad core with 12 GB RAM using MATLAB R2009b (MathWorks).

Basic properties of the biophysical model. We used NEURON 7.2 (Hines and Carnevale, 1997) to develop a computational model of Group Ia/Ib fibers, Group II fibers, segmental interneurons, proprioceptive interneurons, commissural interneurons, and alpha motoneurons (Fig. 1C).

Alpha motoneurons. Alpha motoneurons were modeled using a realistic cat motoneuron shape obtained from the free, shared database at <http://NeuroMorpho.Org> (Alvarez et al., 1998; Ascoli et al., 2007). The size of the soma and length of the dendritic structure were rescaled according to a linear factor extracted from the ratio between the mean dimension of spinal neurons in rats and cats (Roy et al., 2007). The final motoneuron structure included a spherical soma of 40 μm diameter and a dendritic tree encompassing 149 segments. The rostrocaudal and mediolateral positions of motoneuron somas were derived from anatomical experiments. The tracer Fluorogold was injected into the medial gastrocnemius (MG) and tibialis anterior (TA) muscles ($n = 3$ rats). The stereotaxic location of retrogradely labeled motoneurons was reconstructed using NeuroLucida (MBF Bioscience), and averaged across rats (Fig. 2B). For the TA muscle, we modeled a total of 50 motoneurons distributed between L2 (20%) and L3 (80%). A total of 50 motoneurons were modeled for the MG muscle, spanning the spinal segments L3 (20%), L4 (60%), and L5 (20%). A myelinated efferent axon with an explicit representation of the initial segment was attached to each motoneuron. The efferent axon exited the spinal cord via the ventral roots.

Interneurons. Interneurons were modeled as a spherical soma connected to a realistic 3D dendritic tree comprising 83 segments. The realistic shape was obtained from cat interneuron database <http://NeuroMorpho.Org> (Bui et al., 2003; Ascoli et al., 2007). We applied the same geometrical linear scaling as for motoneurons, resulting in an interneuron soma diameter of $\sim 23 \mu\text{m}$. We positioned interneurons with dorsoventral fibers in laminae II and III, and commissural interneurons with spinal cord midline crossing axons in lamina VII. Axon diameters were set at 2.5 μm (Saywell et al., 2011).

Cell properties. Both alpha motoneuron and interneuron soma membranes included fast sodium channels, a delayed rectifier potassium current, N-type and L-type calcium currents, and a calcium-activated potassium current. The initial segment membrane included fast and persistent sodium channels as well as delayed rectifier potassium currents, whereas dendrites were treated as passive compartments. All the modified Hodgkin–Huxley equations for the soma, dendrites, and initial axonal segment were obtained from validated neuron models (McIntyre and Grill, 2002). Electrical parameters are reported in Table 2. The diameters of efferent axons were based on a realistic shape distribution

Table 2. Electrical parameters of the model for cells

Parameters	Values
Electrical parameters	
Axoplasmic resistivity (ρ_a)	200 Ω cm
Soma parameters	
Maximum Na ⁺ conductance (g_{Na})	0.05 S/cm ²
Maximum rectifier K ⁺ conductance (g_{Kr})	0.3 S/cm ²
Maximum Ca ²⁺ activated K ⁺ conductance (g_{KCa})	0.3 S/cm ²
Maximum N-type Ca ²⁺ conductance (g_{CaN})	0.05 S/cm ²
Maximum L-type Ca ²⁺ conductance (g_{CaL})	0.0001 S/cm ²
Leakage conductance (g_{Lk})	0.002 S/cm ²
Na ⁺ Nernst potential (E_{Na})	50 mV
K ⁺ Nernst potential (E_K)	−80 mV
Leakage reversal potential (E_{Lk})	−70 mV
Dendrite parameters	
Leakage conductance (g_{Lk})	0.0002 S/cm ²
Initial segment parameters	
Maximum Na ⁺ conductance (g_{Na})	0.5 S/cm ²
Maximum K ⁺ conductance (g_K)	0.1 S/cm ²
Leakage conductance (g_{Lk})	0.01 S/cm ²

Parameters are taken from McIntyre et al., 2002.

Table 3. Electrical parameters of the axon cable model for myelinated afferent and efferent fibers

Parameters	Values	References
Electrical parameters		
Membrane capacitance (c_m)	2 μ F/cm ²	McIntyre and Grill, 2002
Axoplasmic resistivity (ρ_a)	70 Ω cm	
Nodal Parameters		
Maximum fast Na ⁺ conductance (g_{Naf})	3 S/cm ²	McIntyre and Grill, 2002
Maximum persistent Na ⁺ conductance (g_{Nap})	0.01 S/cm ²	
Maximum slow K ⁺ conductance (g_{Ks})	0.08 S/cm ²	
Leakage conductance (g_{Lk})	0.007 S/cm ²	
Na ⁺ Nernst potential (E_{Na})	60 mV	
K ⁺ Nernst potential (E_K)	−80 mV	
Leakage reversal potential (E_{Lk})	−80 mV	
Internodal parameters		
Myelin conductance (g_{my}), per lamella	0.1 μ F/cm ²	McIntyre et al., 2002
Myelin capacitance (c_{my}), per lamella	0.001 S/cm ²	

Unmyelinated fibers have a continuous active membrane. Number of lamella membranes for the evaluation of the myelin properties varies with fiber diameter.

derived from motor axons in the rat sciatic nerve (Raspovic et al., 2011).

Afferent fibers. We used experimental morphometric data from the rat sciatic nerve to model realistic fiber diameter distributions (Vleggeert-Lankamp et al., 2004). Group I and Group II fibers were modeled as log-norm functions with the following parameters: $\mu = 9 \mu$ m, $\sigma = 0.2 \mu$ m and $\mu = 4.4 \mu$ m, $\sigma = 0.5 \mu$ m, respectively, where μ is the most frequent diameter parameter, and σ is the SD (Vleggeert-Lankamp et al., 2004). Internode length was set to a value of 100D, where D is the fiber diameter. Diameters of the Node of Ranvier were linearly scaled with D, as described previously (Raspovic et al., 2011). Myelinated fibers, which included Group Ia/Ib, Group II, and efferent axons, were modeled as cable-axon structures with two compartments: (1) active Nodes of Ranvier and (2) passive myelinated internodes. A McIntyre-Richardson-Grill (MRG) model (Richardson et al., 2000) was used to describe the equation of the active membrane at the nodes of Ranvier and at the passive internodal segments. Myelin was represented as a nonperfect insulator, as used for model B in the study by Richardson et al., 2000. The nodes of Ranvier's membrane included fast sodium, persistent sodium, and slow potassium channels along with a leakage conductance. All the parameters (Table 3) underlying the electrical properties of the modeled channels were taken from previous computational models (Richardson et al., 2000; McIntyre and Grill, 2002). Node dynamics were extracted from the work of McIntyre and Grill, 2002 in Model DB with accession number 3810 (Hines et al., 2004).

Group Ia/Ib fibers. We modeled 30 Group Ia/Ib afferent fibers for each spinal segment, which resulted in a total number of 180 Group Ia/Ib fibers that were distributed along the whole extent of the lumbosacral spinal cord model. Group Ia/Ib fibers followed a course parallel to that of efferent motor axons below the S1 segment (Rattay et al., 2000). The fibers entered the CSF below the S1 segment and reached their target segments through multiple segmental levels (Rattay et al., 2000). The fibers entered their target segment through the dorsal aspect of the spinal cord. Both the position around the sacral spinal cord and the rostrocaudal location at which each fiber entered its target segment were randomized using a uniform random distribution. Group Ia fiber entered the spinal cord from the L2–L6 spinal segment, bent toward the spinal cord, and established an excitatory synaptic connection with a random dendrite of a motoneuron, thus creating a monosynaptic reflex circuit (Fig. 1C). Group Ia/Ib fiber also contacted a random dendrite of an excitatory interneuron, which was randomly positioned within lamina VII of each segment (Fig. 1C). The excitatory synapse was modeled using a mono-exponential approximation with a decay constant of $\tau = 0.5$ ms. The synaptic conductance was tuned to match the composite subthreshold EPSP evoked at the soma from stimulation of Group Ia fibers (McIntyre et al., 2002). The model included 150 combinations of Group Ia fiber and alpha motoneuron, and 150 combinations of Group Ia/Ib fiber and interneuron.

Group II fibers. We modeled 30 Group II fibers per spinal segment, which followed the same path as Group Ia fibers, and terminated in lamina VII. Afferent fibers innervating each muscle projected to the different segments with the same ratios as the distribution of alpha motoneurons.

Model composition. The model included a total of 180 Group Ia/Ib fibers, 180 Group II fibers, 180 interneurons in lamina VII, 180 interneurons in lamina III, 150 commissural interneurons, and 150 alpha motoneurons.

Coupling between FEM and NEURON models. We computed the voltage solution of the FEM model for a unitary current input located at spinal segments L2, L4, or S1. Electrodes were placed on the midline, or at varying distances from the midline. The electric potentials were exported from the FEM solutions into the realistic biophysical model in Matlab (MathWorks). Stimuli were constructed as monopolar square pulses with a duration of 500 μ s for the experimental validation of the reflex responses (Gerasimenko et al., 2006; Courtine et al., 2009). Cathodal amplitude ranged from 20 to 600 μ A, which covered the parameters (100–300 μ A) used experimentally in rats to facilitate locomotion (Gerasimenko et al., 2006; Courtine et al., 2009). To simulate different amplitudes, we multiplied the voltage solutions with a proper scalar factor, which is appropriate under quasi-static assumptions (Bossetti et al., 2008).

Evaluation of fiber and cell recruitment. Recruitment curves for increasing current amplitudes were measured for each type of fiber and cell in each modeled spinal segment. A fiber was considered recruited when an action potential traveled along its whole length; i.e., when it reached the last node of Ranvier. Cells were considered recruited if the resulting depolarization elicited an action potential that traveled along the efferent axon. The model used the assumption that, at low frequency (1 Hz), the peak-to-peak amplitude of each motor potential evoked by a single EES stimulus is proportional to the number of motor axons recruited either directly or indirectly via monosynaptic or polysynaptic reflex circuits (Fuglevand et al., 1993). Simulated motor evoked potentials were divided into three responses based on their latencies. We linked each of these responses to a specific subset of efferent or afferent fibers based on their respective latency. In the model, the early-, medium-, and late-latency responses were proportional to the number of directly recruited (1) motor axons, (2) Group Ia fibers, and (3) both Group I and Group II fibers, respectively. The late-latency responses likely result from the recruitment of both excitatory and inhibitory interneuronal circuits that receive converging inputs from multifaceted afferents (Jankowska, 1992). Consequently, the number of recruited afferent fibers cannot predict the modulation of late-latency response. However, we used this oversimplification to illustrate the relative recruitment threshold and saturation of Group I and Group II fibers compared with experimental motor re-

sponses. We thus avoided any assumption about putative interneuron circuits, which are poorly characterized (Jankowska, 1992), but sought to provide useful information on the recruitment of afferent fibers with increasing intensities.

Thresholds and saturations were defined as the current amplitude for which 10% and 90% of the total number of fibers was recruited, respectively. Recruitment curves were compared with experimental data using a Kruskal–Wallis test with a 95% level of significance over the distribution of recruitment threshold and saturation currents.

To evaluate the degree of selectivity in the recruitment of muscles with EES, we used a selectivity index previously used in sciatic nerve modeling studies (Raspopovic et al., 2011). Muscular selectivity between TA and MG muscles was defined as follows:

$$\text{Sel}_{\text{TA}} = \text{TA}_{\text{REC}} - \text{MG}_{\text{REC}} \quad (3)$$

where TA_{REC} and MG_{REC} correspond to the normalized amplitude of the motor responses evoked in the TA and MG muscles, respectively. This index spans the interval $[-1, 1]$, where -1 indicates maximum activation of the undesired muscle together with a total absence of activation of the desired muscles, 0 indicates that both muscles are active at the same level, and 1 shows the exclusive recruitment of the targeted muscle.

Experimental procedures

Animal model. Experiments were conducted on adult female Lewis rats (>200 g). All the procedures were approved by the Veterinary Office of the Canton of Vaud, Switzerland. Rats were housed individually on a 12 h light/dark cycle, with access to food and water *ad libitum*. The experiments were performed on different models, depending on the aim of the study. The first series of experiments was conducted on healthy rats ($n = 4$) that were chronically implanted with stimulating electrodes over the dorsal aspect of spinal segments L2, L4, and S1, and with EMG electrodes into the MG and TA muscles bilaterally. EES-evoked motor responses were recorded in the implanted muscles for a range of EES intensities to obtain recruitment curves that could be compared with those obtained in the computational model. A second group of healthy rats ($n = 10$) was tested under acute, anesthetized conditions to conduct complementary neurophysiological and pharmacological experiments. Acute recordings were conducted with the same electrodes and procedures as those used for chronic experiments. Finally, the capacity of spatially distinct EES to modulate specific limb movements during standing and walking was evaluated in a group of spinal rats that were chronically implanted with stimulating electrodes over the midline of S1 spinal segment and the right aspect ($\sim 750 \mu\text{m}$ from the midline) of L2 and S1 segments.

Surgical procedures. All the procedures have been described in detail previously (Gerasimenko et al., 2006; Courtine et al., 2009). Briefly, under general anesthesia and aseptic conditions, a partial laminectomy was performed over spinal segments L2, L4, and S1. Teflon-coated, stainless-steel wires (AS632; Cooner Wire) were passed under the spinous processes and above the dura mater of the remaining vertebrae between the partial laminectomy sites. After removing a small portion (1 mm notch) of the Teflon coating to expose the stainless-steel wire on the surface facing the spinal cord, electrodes were secured on the midline or $\sim 750 \mu\text{m}$ lateral from the midline of spinal segments L2 and S1 by suturing the wires to the dura mater above and below the electrodes. Laterally located wires were tied with knots to the midline wires above and below the electrodes to ensure proper mediolateral spacing. A common ground wire (1 cm of the Teflon removed at the distal end) was inserted subcutaneously in the mid-back region.

Bipolar intramuscular EMG electrodes using the same wire type as above were inserted bilaterally in the mid-belly of the TA and the medial deep region of the MG muscles. All the electrode wires were connected to a percutaneous Amphenol connector cemented to the skull of the rat. Proper location of the epidural and EMG electrodes was verified postmortem.

During the same surgical procedure, some of the rats received a complete SCI. A partial laminectomy was made at a midthoracic level (approximately T7) and the spinal cord was transected. Gel foam was inserted into the gap created by the transection as a coagulant and to separate the cut ends of the spinal cord. The completeness of spinal cord

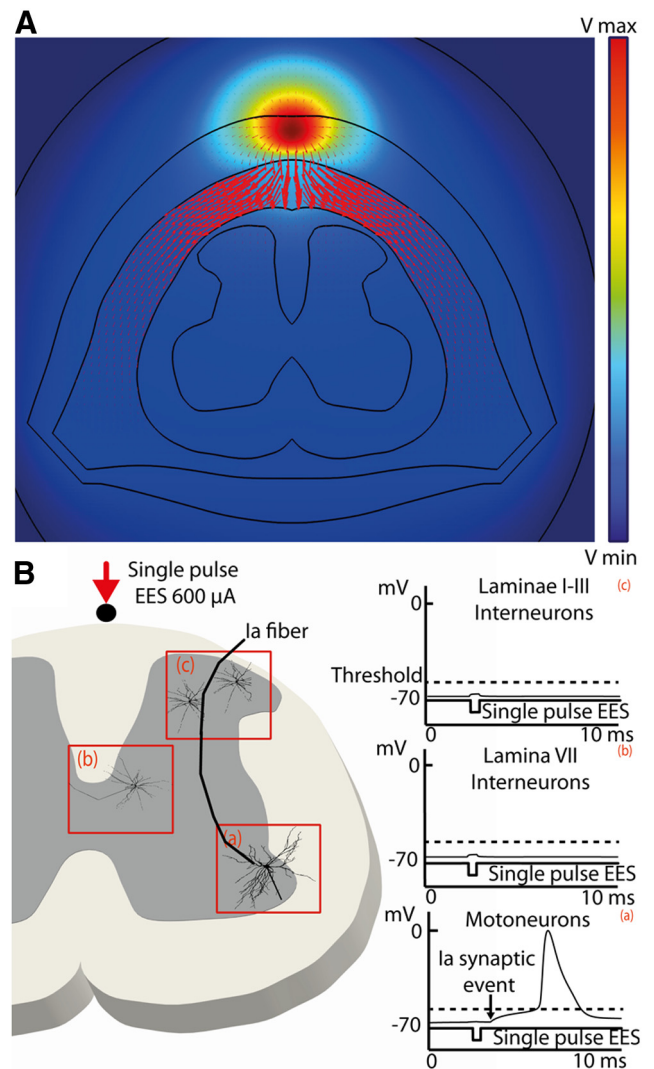


Figure 3. Currents generated by EES and effects on membrane potential of cells. **A**, Color-coded electrical potentials and generated currents following a single pulse of EES applied on the dorsal aspect of the spinal cord. The length and orientation of the arrows represent the intensity and direction of the induced current density, respectively. **B**, Effect of the extracellular field induced by a $500 \mu\text{s}$ duration pulse of EES applied at L4 with an intensity of $600 \mu\text{A}$ on the somatic membrane potential of laminae I–III interneurons (**a**), lamina VII interneurons (**b**), and motoneurons (**c**). The dotted horizontal lines indicate the threshold to elicit action potentials. Even at large intensities, EES did not affect the resting membrane potential of the modeled cells. Alpha motoneurons were stimulated synaptically via the excitatory EPSP resulting from the direct recruitment of Group Ia fibers with EES.

transections was verified by lifting the cut ends of the cord during the surgery as well as histologically postmortem.

Recruitment curves. EES-evoked motor responses were recorded during bipedal standing in a support harness with 80% body weight support. Rectangular pulses (0.5 ms duration) were delivered at 0.2 Hz through the implanted L2, L4, or S1 electrodes (Gerasimenko et al., 2006; Courtine et al., 2009). The intensity of the electrical stimulation was increased progressively from $20 \mu\text{A}$ to $600 \mu\text{A}$. EES-evoked motor potentials were recorded in TA and MG muscles. EMG signals (12.207 kHz) were amplified, filtered (1–5000 Hz bandpass), and stored for off-line analysis. The onset latency and peak amplitude of the different components in compound action potentials were determined through custom-made software in Matlab (MathWorks).

Electrophysiological and pharmacological experiments. Acute experiments were performed under urethane (1 g/kg, i.p.) anesthesia. The following experimental conditions were tested: (1) tonic vibration was

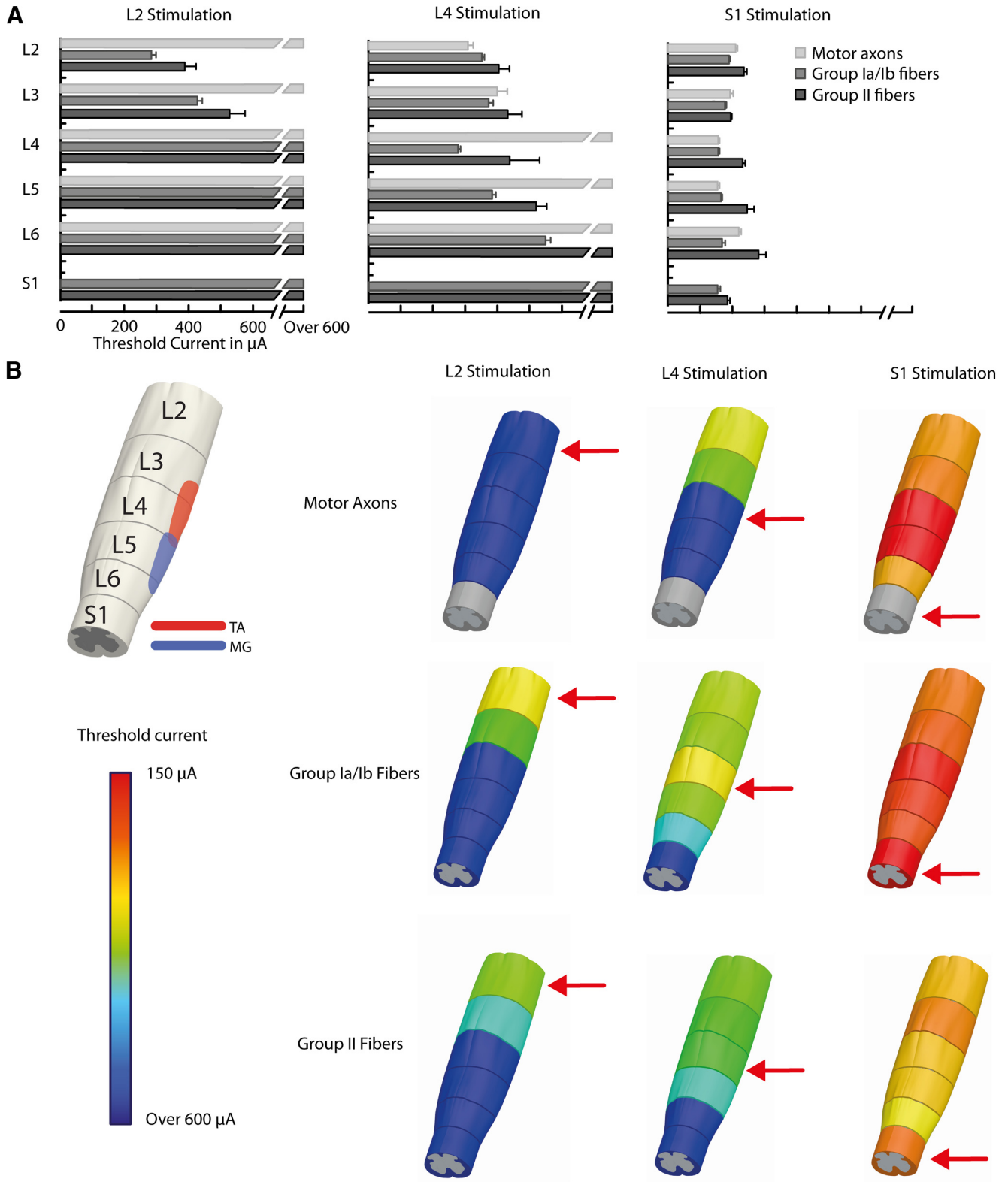


Figure 4. Threshold current for the recruitment of afferent and efferent axons following EES applied at various lumbosacral locations. **A**, Bar graphs reporting the threshold for the recruitment of motor axons, Group Ia/Ib fibers, and Group II fibers in each spinal segment when delivering a cathodal square EES pulse of 500 μs at spinal segments L2, L4, and S1. Thresholds were computed as the necessary current to recruit 10% of the total number of fibers in a given segment. Currents exceeding 600 μA were not considered. **B**, Scheme representing the location of TA and MG motor columns. To facilitate the visualization of current thresholds for each fiber and segment, the data reported in **A** are displayed using a color map overlaid onto a schematic representation of spinal segments. The red arrow indicates the location of the stimulation.

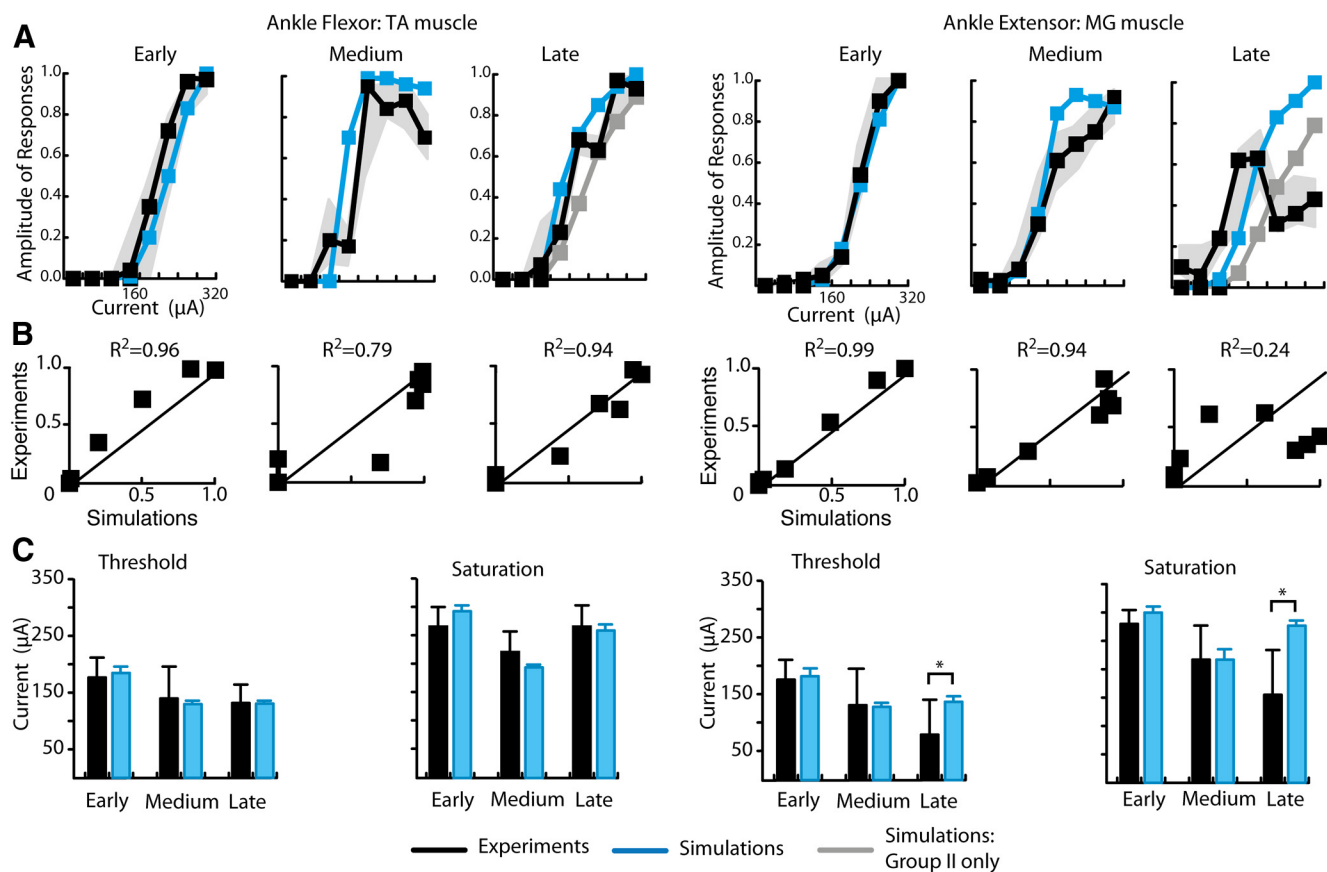


Figure 5. Simulated and experimental modulations of early-, medium-, and late-latency motor responses. **A**, Plots reporting the change in amplitude of the early-, medium-, and late-latency motor responses as a function of current applied at S1 for the computational model compared with experimental recordings. The shaded areas indicate the SEM of response amplitude for the experimental rats. **B**, Correlation plots between the normalized amplitudes of experimental and simulated motor responses. R^2 values are reported in each graph. **C**, Histogram plots reporting the average current values for the threshold and saturation of the early-, medium-, and late-latency motor responses in the TA and MG muscles for experiments and simulations. Significant differences at $*p < 0.05$.

applied to the Achilles' tendon using a vibratory stimulus of 70 Hz frequency and 1 mm amplitude; (2) frequency-dependent depression of proprioceptive reflexes was tested by delivering two successive pulses of EES at intervals of 50 and 100 ms (Gerasimenko et al., 2006); and (3) pharmacological modulation of EES-evoked motor responses was tested using the α_2 -adrenergic receptor agonist Tizanidine (1 mg/kg), which decreases excitability of spinal interneurons supplied by Group II fibers (Corna et al., 1995), and the sodium channel blocker tetrodotoxin (TTX; concentration, 1 μM ; volume of bolus, 50 μl), which suppresses synaptic transmission (Tresch and Kiehn, 2000). Both pharmacological agents were injected into the subarachnoid space of the spinal cord through an inlet cannula. A subsequent bolus injection of saline (40 μl) was made to flush the drug outside the dead space of the cannula (30 μl). The position of the cannula was verified postmortem. In all cases, the tip was positioned between spinal segments L5 and S1.

EES-mediated modulation of standing and walking. An upper-body harness was used to support spinal rats ($n = 3$) during bipedal stepping on a treadmill (9 cm s^{-1}). An automated, servo-controlled robotic arm (Robomedica) adjusted the level of body-weight support (50–80% of body weight) to obtain optimal facilitation of stepping. Modulation of bipedal standing was evaluated using a robotic postural neuroprosthesis that provided a constant force in the direction of gravity (80% of body weight), while preventing fall in the mediolateral direction (Dominici et al., 2012). To transform lumbosacral circuits from nonfunctional to highly functional networks, a systemic administration of quipazine and 8-OHDAPT was delivered 10 min before testing (Courtine et al., 2009). Testing was conducted at 5 weeks postlesion.

Kinematic and EMG recordings during standing and walking. Three-dimensional video recordings were made using the motion capture sys-

tem Vicon by means of 12 infrared television cameras (200 Hz). Reflective markers were attached bilaterally overlying the following anatomical landmarks: iliac crest, greater trochanter, lateral condyle, lateral malleolus, and metatarsophalangeal joint. Nexus (Vicon) software was used to obtain the spatial coordinates of the markers. The body was modeled as an interconnected chain of rigid segments, and joint angles were generated accordingly (Courtine et al., 2009). EMG signals (2 kHz) were amplified, filtered (10–1000 Hz bandpass), stored, and analyzed off-line. The vertical component of ground reaction forces was monitored using a biomechanical force plate (2 kHz, HE6X6, AMTI).

Results

Electrical potential and currents induced by EES

We developed a 3D FEM model to characterize the electric potential and currents induced by a single pulse of EES applied over the midline and dorsal aspect of a spinal segment. Figure 3A shows a color-coded representation of the electrical potential resulting from EES in the model. The length and orientation of the arrows represent the intensity and direction of the induced current density, respectively. EES-induced currents primarily flowed within the well conductive CSF, where they reached both the dorsal and ventral roots. Amplitude of EES-induced currents sharply decreased in the white and gray matter. This rapid attenuation of EES-induced currents within spinal structures was due to the lower transversal conductance of the white and gray matters compared with the CSF liquid (Table 1), as observed in previous models (Holsheimer, 2002; Ladenbauer et al., 2010).

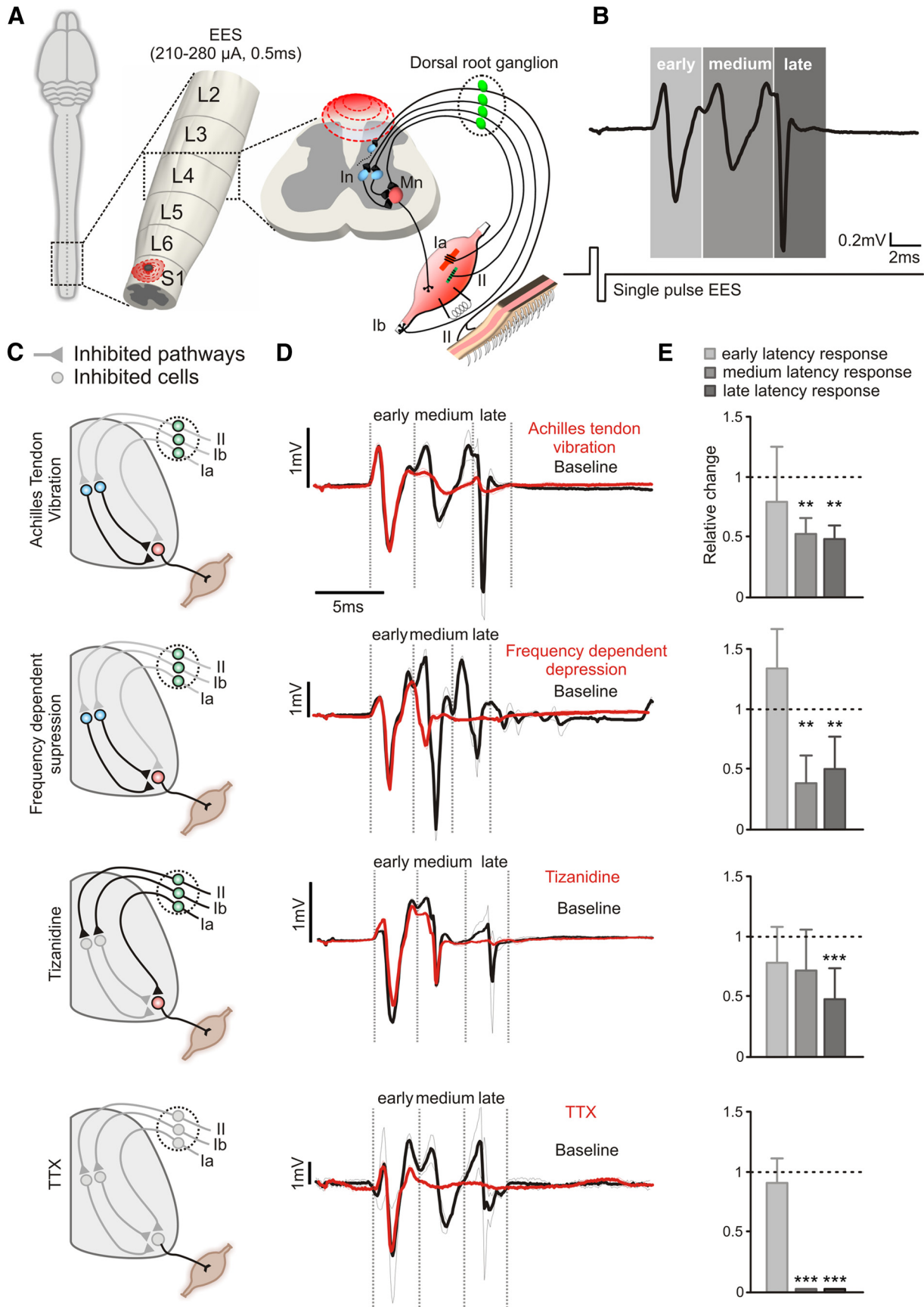


Figure 6. Electrophysiological and pharmacological evaluations of fibers and circuits engaged by EES *in vivo*. **A**, Scheme illustrating the putative afferent fibers innervating proprioceptors and mechanoreceptors, and their associated reflex circuits activated by EES. In, Interneuron. Mn, motoneuron. **B**, Representative recordings of the early-, medium-, and late-latency motor responses recorded in the TA muscle following EES applied at S1. The responses were differentiated based upon their respective latencies. **C**, Theoretical schemes illustrating which (Figure legend continues.)

Robustness of the 3D FEM model

In the present model, we added noninformative compartments around the spinal cord to ensure proper equation settings. However, the size of these compartments may influence the quality of the solutions. To test the robustness of the model, we doubled the size and length of the structures surrounding the spinal cord. We used the correlation coefficient and the magnification factor to evaluate putative changes in voltage distribution inside the CSF and spinal cord (Raspopovic et al., 2011). Both parameters were equal to 1, which indicated that the model was unaffected when changing boundary condition settings. These results demonstrate that the implemented dimensions were appropriate to ensure correct solutions in the computational model.

Impact of EES on membrane potential of modeled cells and intraspinal axons

The small amplitude of induced currents in the gray and white matters in response to EES suggested that a direct excitation of internal spinal cord structures was improbable. Evaluation of the impact of EES on interneurons (Fig. 3B) located in different regions of the spinal cord and on motoneurons (Fig. 3B) confirmed that a single pulse of EES failed to alter the membrane potential of the modeled cells with current amplitudes as large as 1 mA. This suggests that EES does not directly stimulate somas or dendritic compartments of cells regardless of their size or position in the gray matter. In fact, the external electrical excitability of cell membranes is proportional to the second spatial derivative along the direction of the membrane (Rattay, 1986). Consequently, the probability of direct excitation of cells is markedly lower than the probability of recruiting long myelinated fibers, suggesting that EES may recruit axons running in the gray matter (Lavrov et al., 2008). However, our computer simulations revealed that EES did not recruit dorsoventrally projecting fibers and commissural axons.

Impact of EES on motor axons

EES elicited currents that flowed dorsoventrally within the CSF, which suggested that a single pulse of EES might recruit myelinated motor axons running into the ventral roots. Computer simulations confirmed that EES could elicit action potentials that occurred at, and propagated along, the motor axons. The orthodromic volley induced a direct muscle response. Instead, antidromically propagating action potentials led to a depolarization of alpha motoneurons' somas (data not shown). The intensity of current necessary to recruit a given motor axon significantly depended upon the stimulated segment. Although EES applied at S1 elicited action potentials at low threshold in virtually all the modeled motor axons because of their course in the vicinity of sacral segments, the efficacy of EES to recruit motor axons rapidly decreased and eventually vanished when positioning stimulating electrodes more rostrally (Fig. 4).

Impact of EES on Group Ia/Ib and Group II fibers

The substantial currents elicited by EES within the CSF suggested that myelinated afferent fibers running into the dorsal roots were the primary sites of action of EES. Computerized simulations confirmed that EES-induced depolarization first occurred in Group Ia/Ib and Group II fibers (Fig. 4). As expected based on their thicker diameter, Group Ia/Ib fibers were depolarized at significantly lower thresholds than Group II fibers ($p < 0.01$; Fig. 4). We found a clear gradient in the recruitment of segment-specific afferent fibers. EES first depolarized Group Ia/Ib and Group II fibers innervating the stimulated segment (Fig. 4). The influence of EES progressively expanded to neighboring segments at higher stimulation intensities with the notable exception of EES applied at S1, which recruited nearly all the afferent fibers simultaneously due to their common course around the sacral spinal cord (Fig. 4). Cutaneous afferents, which encompass the same A α and A β diameter classes as those modeled for Group I and Group II fibers, may also be recruited in response to EES.

Experimental validation of the computational model

To validate the computational model, we conducted acute electrophysiological experiments in intact rats under anesthetized conditions. EES was applied over the midline and dorsal aspect of S1 segment. EMG responses evoked by a single pulse (0.5 ms) of EES were recorded in both extensor (MG) and flexor (TA) muscles of the ankle. EES elicited three successive motor responses that we distinguished based on their respective latencies (see Fig. 6B). Each response emerged at a distinct current threshold and showed specific modulation with increasing EES intensities (Fig. 5A). These results suggest that each response is primarily due to the recruitment of a specific type of fibers and circuits.

We used the computational model to establish predictions of the putative fibers associated with each response. This analysis suggested that (1) the early-latency response (3–5 ms) resulted from the direct recruitment of motor axons; (2) the medium-latency response (5–9 ms) was elicited via the recruitment of Group Ia fibers that activated monosynaptic reflex circuits; and (3) the recruitment of Group Ia/Ib and Group II fibers caused a long-latency response (9–15 ms) through the activation of disynaptic and/or trisynaptic reflex circuits (Fig. 6A). We translated these predictions into recruitment models in which the amplitude of each of the three EES-induced motor responses (early-, medium-, late-latency response) was directly proportional to the number of fibers recruited for each class of axons (motor axons, Group Ia, Group II, and Group Ia/Ib). Based on this classification, we evaluated the threshold, modulation, and saturation for each of the modeled motor responses over a range of current intensities, and compared the results of these computerized simulations with the outcomes of *in vivo* experiments. Figure 5A displays the actual and predicted recruitment curves ($n = 4$ rats, 13 muscles) for the MG and TA muscles. The model accurately predicted the threshold ($p > 0.05$; Fig. 5C), saturation level ($p > 0.05$; Fig. 5C), and slopes of the recruitment curves ($p > 0.05$; Fig. 5B) for the early- and medium-latency responses of the TA and MG muscles. Late-latency responses were oversimplified in the recruitment model since we did not incorporate interneuron circuits. However, late-latency responses computed based on the number of recruited fibers were close to experimental results for the TA muscle ($p > 0.05$; Fig. 5C). Instead, we found a significant discrepancy ($p < 0.05$; Fig. 5A–C) between actual and predicted late-latency responses in the MG muscle. First-order interneurons connected to extensor motor pools receive a rich innervation from proprioceptive afferents (Tripodi et al., 2011), which

←

(Figure legend continued.) neurons, fibers, and/or circuits were likely inhibited (gray) in response to each experimental manipulation in anesthetized rats. **D**, Representative waveforms recorded in the same rat during baseline, concurrently to Achilles' tendon vibration, during repeated (10 Hz) stimulation, and after the administration of tizanidine or TTX, from top to bottom. Each waveform is the average (\pm SD) of 10 stimuli. **E**, Histogram plots reporting, for each experimental condition, the relative change in the integral of the recruitment curve for each motor response compared with baseline. Significant differences at $**p < 0.01$ and $***p < 0.0001$, respectively.

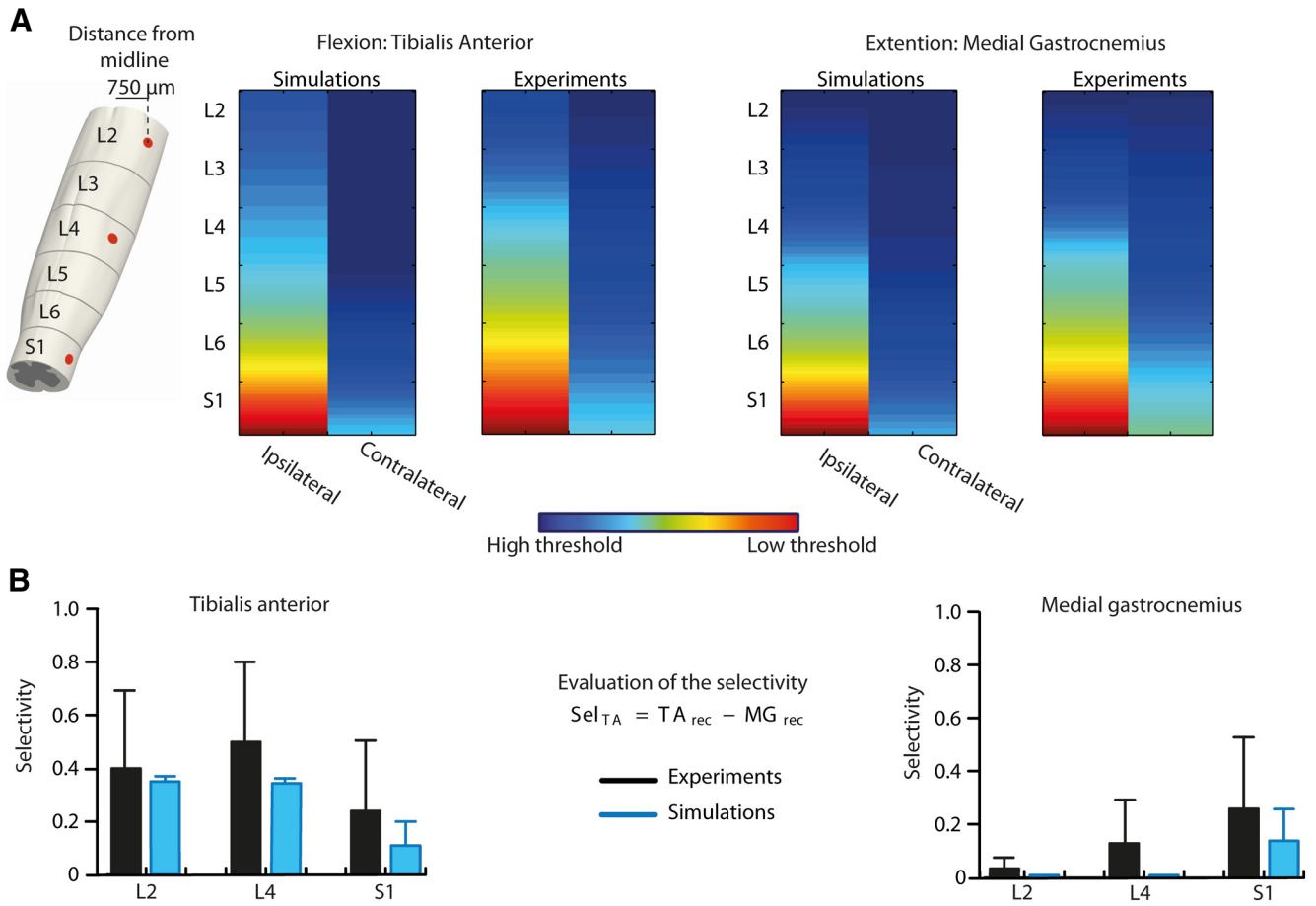


Figure 7. Recruitment of selective sensorimotor circuits with EES. **A**, Color maps representing the current threshold for the recruitment of the medium-latency response following stimulation applied at spinal segment L2, L4, and S1 at a distance of 750 μm from the spinal cord midline in the computational compared with experimental rats. Current threshold for nonstimulated segments were obtained through linear interpolation. **B**, Selectivity in the recruitment of TA and MG muscles were computed for EES applied at spinal segment L2, L4, and S1 in the computational model compared with experimental rats.

trigger a mixture of inhibitory and excitatory inputs to motoneurons (Jankowska, 1992). This complex interneuron circuit organization likely explains the failure of the model to predict late-latency responses only based on the number of recruited afferent fibers.

Experimental evaluation of model predictions

We next conducted a series of electrophysiological and pharmacological testing to provide experimental evidence for the predictions of the computational model.

To assess the contribution of direct motor axon recruitment to the genesis of early-latency responses, we blocked sodium currents through a local intrathecal delivery of TTX at L5/L6 spinal segments. TTX eliminates action potentials in alpha motoneurons and interneurons (Tresch and Kiehn, 2000), which abolished both medium- and long-latency responses ($p < 0.0001$; Fig. 6C–E). The maximum amplitude, latency, and shape of early-latency responses was not affected by TTX ($p > 0.05$; Fig. 6C–E), although a two- to threefold increase in current amplitude was necessary to elicit the same response as before injection. These results revealed that the early response was not dependent on chemical neurotransmission and, thus, exclusively relied on the direct recruitment of motor axons. The higher threshold was expected, since the partial diffusion of TTX within the ventral roots likely blocked sodium channels in the initial segments of the efferent axons.

We combined two well established electrophysiological tests to evaluate the potential contribution of Group Ia and Group II fibers to medium- and long-latency responses. First, we applied continuous vibration (70 Hz) to Achilles’ tendons bilaterally. Vibration primarily recruits muscle spindle Group Ia afferents and, to a lesser extent, Group II afferents (Roll et al., 1989). The vibration-induced afferent volley induces a depression of monosynaptic and polysynaptic reflex circuits due to presynaptic inhibition onto spindle afferent fibers (Bove et al., 2003). The early-latency response was globally unaffected by the vibratory stimulus. Instead, the amplitude of both medium- and long-latency responses significantly decreased during vibration ($p < 0.01$; Fig. 6C–E). Second, we tested the impact of repetitive EES with low (0.2 Hz) and high (10/20 Hz) frequency on the magnitude of motor responses. Our objective was to verify the occurrence of frequency-dependent depression in reflex circuits associated with muscle proprioceptive afferents (Gerasimenko et al., 2006). EES delivered at high frequency led to a significant decrease of both medium- and long-latency responses ($p < 0.01$; Fig. 6C–E), but did not alter early-latency responses ($p > 0.05$; Fig. 6C–E). The medium-latency response thus exhibited the electrophysiological signature of the Hoffmann reflex (Schieppati, 1987).

To assess the contribution of Group II fibers to the long-latency response, we depressed the transmission in Group II interneurons with an intrathecal injection of the $\alpha 2$ -adrenergic

receptor agonist tizanidine (Bras et al., 1990). Early- and medium-latency responses did not change significantly after tizanidine injection ($p > 0.05$; Fig. 6C–E). Concurrently, we observed a substantial decrease in the amplitude of long-latency responses, which nearly vanished with large concentrations of tizanidine ($p < 0.0001$; Fig. 6C–E).

Computer and experimental evaluation of EES selectivity

The developed computational model provided the opportunity to iterate simulations to identify near-optimal positioning of EES electrodes for achieving the selective recruitment of left versus right limb muscles. Computer simulations revealed that 750 μm lateral to the spinal cord midline was the more robust location to induce unilateral recruitment of limb muscles. Experiments in anesthetized rats confirmed that EES applied $\sim 750 \mu\text{m}$ lateral to the midline near-exclusively induced motor responses in muscles ipsilateral to the stimulation (Fig. 7A). We found a remarkable similarity between predicted and experimental excitability maps associated with the recruitment of flexor and extensor motor pools with EES applied on the lateral aspect (750 μm) of L2, L4, and S1 (Fig. 7B). We next evaluated the ability to recruit extensor versus flexor with EES applied at specific segment locations. To quantify muscle selectivity, we developed a simple measure reflecting the relative recruitment of TA and MG muscles in response to EES (Fig. 7C). As expected based on segmental recruitment maps (Fig. 4), both computerized simulations and experiments showed that, under static conditions, the capacity of EES to recruit specific sensorimotor circuits was limited. Whereas EES applied at the rostral level achieved an acceptable degree of selectivity in the recruitment of the TA muscle, sacral EES engaged both flexor- and extensor-related circuits concurrently.

Evaluation of EES selectivity during standing and walking in spinal rats

We sought to illustrate the predictive value of the developed computational model to facilitate standing and walking in adult rats with complete mid-thoracic transection. At 5 weeks postlesion, all the tested rats ($n = 3$) exhibited complete hindlimb paralysis when supported bipedally over a moving treadmill belt (Fig. 8A, B). Continuous (40 Hz, 0.2 ms, $\sim 200 \mu\text{A}$) EES applied over the midline of S1 spinal segment enabled bilateral stepping movements with alternating oscillations of the left and right hindlimbs (Fig. 8B, C). As predicted by the model, continuous EES applied $\sim 750 \mu\text{m}$ lateral to the spinal cord midline elicited coordinated stepping of the hindlimb ipsilateral to the stimulation but did not facilitate movement in the contralateral hindlimb (Fig. 8B, C).

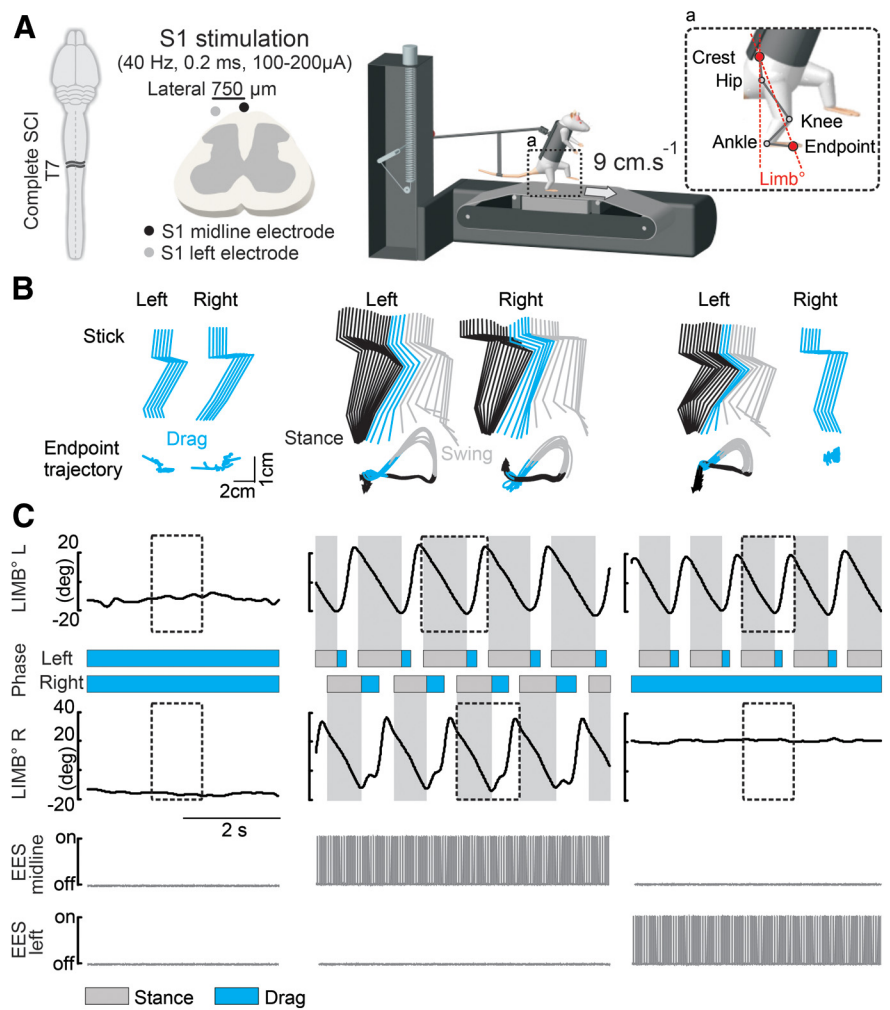


Figure 8. Lateralized EES promotes unilateral facilitation of stepping in spinal rats. **A**, Schematic of the complete SCI, electrode positioning, and robotic system providing adjustable body weight support during stepping on a treadmill (9 cm/s). Reflective markers were positioned overlying bony landmarks to monitor hindlimb joint motion. The limb was defined as a virtual segment reflecting whole-hindlimb oscillation. **B**, Representative stick diagram of decomposition of left and right hindlimb movements together with the successive, color-coded trajectories of the limb endpoint extracted from a continuous sequence of stepping movements without stimulation, and during EES applied at 0 or 750 μm from the midline (left) of spinal segment S1. Stick diagrams were extracted from the time window highlighted by the dotted squares in **C**. **C**, The oscillations of the left and right limbs are displayed at the bottom together with the stance (filled) and swing (empty) phases of gait, and the concurrent pattern of EES.

Analysis of EMG activity in flexor (TA) and extensor (MG) muscles during stepping revealed that each burst was elaborated from a succession of medium- and late-latency motor responses that were locked to each pulse of EES (Fig. 9A, B). The amplitude of the evoked responses in each muscle was strictly gated as a function of the general excitability of the motor pool and, thus, as a function of the phase of the step cycle ($p < 0.01$; Fig. 9C, D). This phase-dependent modulation of segmental reflex circuits ensured the alternating recruitment of flexor and extensor muscles with the appropriate timing and amplitude to produce coordinated stepping movements.

The model also predicted that EES applied at L2 would primarily engage ankle flexor muscles, whereas EES at S1 would preferentially influence extensor muscles. To test these predictions during a behaviorally relevant task, we applied EES on the lateral aspect of L2 and S1 spinal segments during bipedal standing enabled by a robotic postural neuroprosthesis (Fig. 10A). The robot provided a constant force against the direction of gravity (80% of the body weight) and prevented falls in the mediolateral

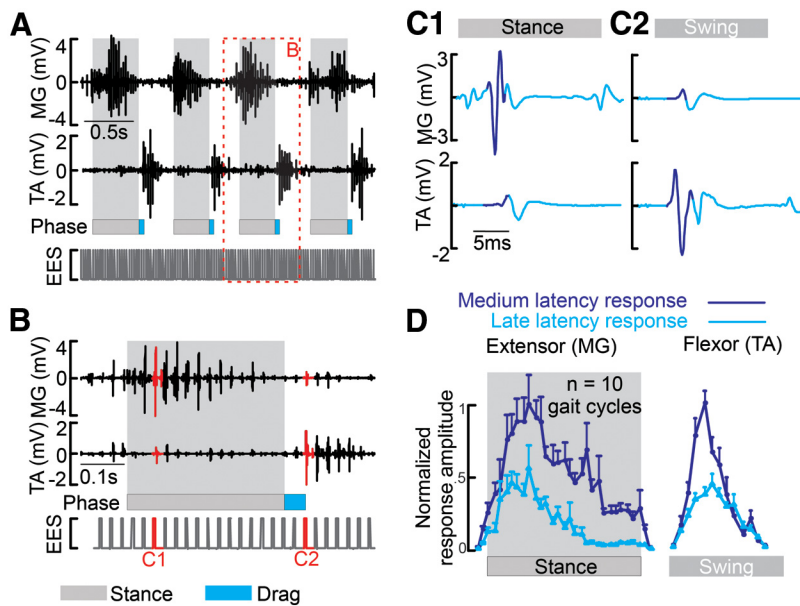


Figure 9. Modulation of medium- and late-latency reflexes during gait. **A**, Continuous sequence of EMG activity recorded from the left MG and TA muscles during stepping enabled by EES. **B**, Detailed EMG activity extracted from the time window highlighted by the red, dotted line in **A**. During locomotion, each pulse of EES induces a reflex response locked to the stimulation. **C**, Color-coded medium- and late-latency responses evoked in the ipsilateral MG and TA muscles during stance (**C1**) versus swing (**C2**). **D**, The plots report modulation of mean ($n = 10$ responses per rat) amplitude (\pm SD) of medium- and late-latency responses over the course of the stance phase for the MG muscle, and the swing phase for the TA muscle.

direction. The application of continuous EES at L2 induced a rapid and prolonged flexion of the hindlimb ipsilateral to the stimulation. This whole-limb flexion was associated with a sustained activation of flexor (TA) muscles, whereas extensor (MG) muscles became quiescent (Fig. 10B). As observed during stepping, the elaboration of hindlimb muscle activity during standing was mediated through the repeated recruitment of medium- and late-latency motor responses (Fig. 10C). In turn, EES applied at S1 promoted a pronounced extension of all the joints in the hindlimb ipsilateral to the stimulation, which was associated with a substantial activation of extensor (MG) muscles and a significant increase of vertical ground reaction forces (Fig. 10B).

The degree of selectivity in the recruitment of motor pools during standing with site-specific EES was remarkably high compared with model predictions. During standing, EES applied at S1 near-exclusively induced medium-latency responses in extensor (MG) muscles, whereas EES delivered at L2 elicited medium- and late-latency responses restricted to flexor (TA) muscles (Fig. 10C).

Discussion

We developed a computational model of the rat lumbosacral spinal cord that uncovered the types of fibers and circuits recruited by EES, and predicted electrode positioning to promote specific movements during standing and walking in spinal rats. This model provides a mechanistic framework for the design of neuroprosthetic systems based on spinal cord stimulation to improve the recovery of sensorimotor functions following neurological disorders.

Design, validation, and limitation of the computational model

Previous computational models of electrical spinal cord stimulation focused on global anatomical features to determine the generated electrical fields (Coburn, 1980; Struijk et al., 1992, 1993; Rattay et al., 2000), morphological characteristics to identify the

recruited neural structures (Struijk et al., 1993; Holsheimer, 1998; Ladenbauer et al., 2010), or advanced cell models to characterize neuronal modulation (McIntyre and Grill, 2002). Here, we combined all the aspects implemented in previous models and added new characteristics. Specifically, we modeled multiple motoneuron columns, various lamina-specific interneurons, and the different types of myelinated afferent fibers—all in statistically realistic quantities. Anatomical features were derived from neuromorphological evaluations conducted in the same rats as those used for *in vivo* experiments. Our objective was to develop an anatomically realistic model that could predict a wide range of experimental results.

The number of synaptic connections was highly underestimated in the model. However, our objective was to identify the neural structures recruited with EES, which is not influenced by complex interactions between inhibitory and excitatory synaptic events. We made various geometrical approximations to build the FEM structure. For example, the bony vertebrae were modeled as an outer structure surrounding the spinal cord. Nevertheless, we focused on distinguishing the neural structures recruited with stimulation applied directly to the spinal cord, which justified such approximations.

To quantify the outputs of the model, we postulated the existence of direct relationships between the number of recruited axons and the overall muscle activation (Fuglevand et al., 1993). We thus translated microscopic events, i.e., firing along any axon of the model, into a macroscopic quantity that can be measured experimentally, i.e., amplitude of EMG activity. We previously exploited this reductionism to validate a hybrid computational model of sciatic nerve stimulation (Raspopovic et al., 2012). Here, we expanded this method to a realistic number of motoneurons, interneurons, and fibers in the spinal cord; and to multiple motor responses conveyed through distinct neural pathways. Using this assumption, we could dissociate the different components of EES-induced motor responses based upon their respective latencies and could formulate hypotheses on the putative underlying circuits. Despite modeling approximations, computer simulations accurately predicted the threshold, saturation, and modulation of multiple motor responses in both extensor and flexor muscles following EES applied to various rostrocaudal and mediolateral locations over the entire extent of lumbosacral segments. To the best of our knowledge, this is the more extensive qualitative and quantitative validation of a computational model for electrical spinal cord stimulation.

EES exerts no direct influence on cells

The computational model revealed that EES generates currents that primarily flow within the well-conductive CSF (Rattay et al., 2000). This result suggested that EES could recruit motor axons at their exit from the spinal cord. Indeed, computer simulations and experiments in which synaptic transmission was blocked with TTX demonstrated that EES induces an early response in hindlimb muscles through the direct recruitment of motor ax-

ons, but only when stimulating the more caudal levels. Fibers innervating hindlimb muscles run on the lateral aspect of sacral segments, which explained their recruitment during EES applied toward S1 (Rattay et al., 2000; Gerasimenko et al., 2006). However, relatively high currents were necessary to elicit sizeable responses. Indeed, we did not detect direct responses in hindlimb muscles during standing and walking enabled by EES. These observations exclude a significant contribution of direct muscle activation to movement execution during EES.

The model revealed that EES-induced currents poorly penetrate spinal cord structures. Simulations showed that EES exerts no significant influence on neurons. Likewise, EES failed to recruit intrasegmental and commissural axons within the gray matter, as expected based on the small caliber of these axons and their lack of myelin. These results indicated that, contrary to previous hypotheses (Lavrov et al., 2006, 2008), the direct stimulation of interneurons or their axons is unlikely to contribute to facilitating motor execution during EES.

EES facilitates motor execution through the recruitment of myelinated afferent fibers

The computational model predicted that EES engages spinal circuits transynaptically through the recruitment of Group I and Group II fibers, which convey sensory input from muscle spindles, Golgi's tendon organs, and cutaneous receptors (Gardner et al., 2000). These fibers are recruited at low excitation threshold due to their large diameter and their change of path direction with respect to the EES-induced electric potential (Rattay et al., 2000; Ladenbauer et al., 2010).

We deployed a range of electrophysiological and pharmacological experiments to identify the nature of neuronal circuits recruited with EES. Computer simulations suggested that the medium-latency response relied on the recruitment of Group Ia fibers—a response equivalent to the Hoffmann reflex (Schieppati, 1987). Pharmacological and electrophysiological testing confirmed that this response exhibited the stereotypical signature of the monosynaptic reflex.

Identification of the neural structures associated with the late-latency responses was less univocal. Computer simulations and pharmacological experiments provided evidence suggesting that these responses primarily emerged from the activation of interneurons via the direct recruitment of Group II fibers (Jankowska, 1992; Minassian et al., 2004; Gerasimenko et al., 2006). Simulations based on this model predicted the modulation of late-latency responses in flexor muscles, which likely correspond to the classical flexor reflex. However, we found significant discrepancies between simulated and actual responses in extensor muscles. Group Ia/Ib fibers and cutaneous afferents are known to exert robust excitatory and inhibitory

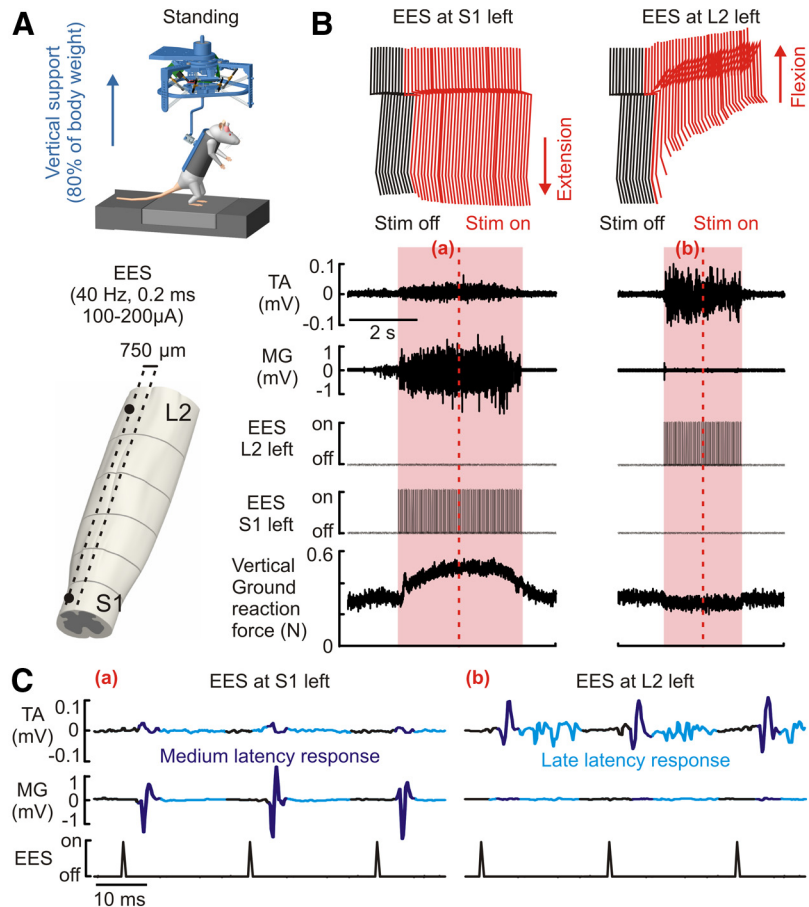


Figure 10. Site-specific EES promotes extension versus flexion of the hindlimb during standing in spinal rats. **A**, Robotic postural neuroprosthesis providing adjustable body weight support in the vertical and mediolateral directions during bipedal standing. Scheme showing the lateralized location of stimulating electrodes at spinal segment L2 and S1. **B**, Representative stick diagram of decomposition of hindlimb movements before (black) and during (red) the application of continuous EES at S1 versus L2 during standing. EMG activity of left ankle muscles and vertical ground reaction forces before, during (shaded area), and after delivering continuous EES at L2 versus S1 during standing. **C**, Color-coded medium- and late-latency motor responses recorded in the left MG and TA muscles following EES applied at S1 versus L2, respectively. The displayed temporal windows (**a**, **b**) were extracted from the middle of the stimulating period shown in **B**.

influences on extensor motoneurons via disynaptic and trisynaptic reflex circuits that were not modeled in our computational model (Guertin et al., 1995; McCrea et al., 1995). Late-latency responses evoked in extensor muscles probably result from the recruitment of multifaceted polysynaptic circuits.

Mechanisms underlying the facilitation of motor execution with EES

Our results suggest that the elaboration of motor patterns with EES relies on two complementary mechanisms: (1) the recruitment of segmental reflex circuits, and (2) the widespread influence of proprioceptive and cutaneous inputs on the state of spinal circuits (Jankowska, 1992; McCrea, 2001; Dietz, 2002).

During motor execution enabled by EES, each stimulus elicited a medium- and late-latency response (Lavrov et al., 2008). Our results indicate that these responses correspond to the activation of monosynaptic and polysynaptic reflex circuits, respectively. Here, we showed that the bursts of leg muscle activity during stepping and standing were elaborated from these motor responses. In parallel, the propagation of the tonic neural drive elicited along proprioceptive and cutaneous fibers likely activates central pattern-generating circuits. For example, the recruitment of Group Ia fibers with electrical stimulation (McCrea, 2001) or

muscle vibration (Gerasimenko et al., 2010) triggers step-like movements of the lower limbs. In turn, the transformation of spinal circuits from resting to rhythmic state leads to the reconfiguration of sensorimotor circuits, whereby reflex pathways become gated based on the performed task (Stein and Capaday, 1988) and the phase of movement (Courtine et al., 2007; Lavrov et al., 2008). Here, we showed that task-dependent modulation of medium- and late-latency responses ensured the appropriate timing and amplitude of leg muscle activation during standing and walking in spinal rats. The tuning of segmental reflex circuits contributed to reinforcing EES selectivity. While the model anticipated a limited ability to recruit extensor- versus flexor-related circuits with the application of site-specific EES, task-dependent reconfiguration of these reflex pathways enabled a high degree of specificity in the elicited movements of extension versus flexion *in vivo*.

Practical value of the computational model

Finally, we sought to illustrate the practical value of the computational model for therapeutic applications. For this, we iterated computer simulations to determine optimal electrode positioning to engage specific subsets of sensorimotor circuits, or to recruit afferent fibers unilaterally. Experimental recordings based on model predictions revealed the capacity of site-specific EES to promote limb-dependent extension and flexion movements during standing and walking in spinal rats. Time-consuming mapping experiments documented comparable properties of spinal sensorimotor circuits in a paraplegic man (Harkema et al., 2011).

Our computational model can provide a faster, and arguably more precise, alternative to optimize the position, size, and configuration of EES electrodes. The model may also help in identifying the more efficient combinations of electrodes to achieve the highest possible degree of specificity in the recruitment of sensorimotor circuits with EES.

Differences between static and dynamic conditions stress the importance of extending our computational model to more advanced simulations combining static and dynamic network modeling. With the availability of high-density electrode arrays affording near-infinite stimulating capabilities (Gad et al., 2013), computational models will play an essential role to steer the development of spinal neuroprosthetic systems to improve the recovery of motor functions after neurological disorders.

References

- Alvarez FJ, Pearson JC, Harrington D, Dewey D, Torbeck L, Fyffe REW (1998) Distribution of 5-hydroxytryptamine-immunoreactive boutons on α -motoneurons in the lumbar spinal cord of adult cats. *J Comp Neurol* 393:69–83. [CrossRef Medline](#)
- Ascoli GA, Donohue DE, Halavi M (2007) NeuroMorpho.Org: a central resource for neuronal morphologies. *J Neurosci* 27:9247–9251. [CrossRef Medline](#)
- Bossetti CA, Birdno MJ, Grill WM (2008) Analysis of the quasi-static approximation for calculating potentials generated by neural stimulation. *J Neural Eng* 5:44–53. [CrossRef Medline](#)
- Bove M, Nardone A, Schieppati M (2003) Effects of leg muscle tendon vibration on group Ia and group II reflex responses to stance perturbation in humans. *J Physiol* 550:617–630. [CrossRef Medline](#)
- Bras H, Jankowska E, Noga B, Skoog B (1990) Comparison of effects of various types of NA and 5-HT agonists on transmission from group II muscle afferents in the cat. *Eur J Neurosci* 2:1029–1039. [CrossRef Medline](#)
- Bui TV, Cushing S, Dewey D, Fyffe RE, Rose PK (2003) Comparison of the morphological and electrotonic properties of Renshaw cells, Ia inhibitory interneurons, and motoneurons in the cat. *J Neurophysiol* 90:2900–2918. [CrossRef Medline](#)
- Coburn B (1980) Electrical stimulation of the spinal cord: two-dimensional finite element analysis with particular reference to epidural electrodes. *Med Biol Eng Comput* 18:573–584. [CrossRef Medline](#)
- Coburn B (1985) A theoretical study of epidural electrical stimulation of the spinal cord—Part II: Effects on long myelinated fibers. *IEEE Trans Biomed Eng* 32:978–986. [Medline](#)
- Corna S, Grasso M, Nardone A, Schieppati M (1995) Selective depression of medium-latency leg and foot muscle responses to stretch by an alpha 2-agonist in humans. *J Physiol* 484:803–809. [Medline](#)
- Courtine G, Harkema SJ, Dy CJ, Gerasimenko YP, Dyhre-Poulsen P (2007) Modulation of multisegmental monosynaptic responses in a variety of leg muscles during walking and running in humans. *J Physiol* 582:1125–1139. [CrossRef Medline](#)
- Courtine G, Gerasimenko Y, van den Brand R, Yew A, Musienko P, Zhong H, Song B, Ao Y, Ichiyama RM, Lavrov I, Roy RR, Sofroniew MV, Edgerton VR (2009) Transformation of nonfunctional spinal circuits into functional states after the loss of brain input. *Nat Neurosci* 12:1333–1342. [CrossRef Medline](#)
- Dietz V (2002) Proprioception and locomotor disorders. *Nat Rev Neurosci* 3:781–790. [CrossRef Medline](#)
- Dominici N, Keller U, Vallery H, Friedli L, van den Brand R, Starkey ML, Musienko P, Riener R, Courtine G (2012) Versatile robotic interface to evaluate, enable and train locomotion and balance after neuromotor disorders. *Nat Med* 18:1142–1147. [CrossRef Medline](#)
- Edgerton VR, Harkema S (2011) Epidural stimulation of the spinal cord in spinal cord injury: current status and future challenges. *Expert Rev Neurother* 11:1351–1353. [CrossRef Medline](#)
- Fénelon G, Goujon C, Gurruchaga JM, Cesaro P, Jarraya B, Palfi S, Lefaucheur JP (2012) Spinal cord stimulation for chronic pain improved motor function in a patient with Parkinson's disease. *Parkinsonism Relat Disord* 18:213–214. [CrossRef Medline](#)
- Fuentes R, Petersson P, Siesser WB, Caron MG, Nicoletis MA (2009) Spinal cord stimulation restores locomotion in animal models of Parkinson's disease. *Science* 323:1578–1582. [CrossRef Medline](#)
- Fuglevand AJ, Winter DA, Patla AE (1993) Models of recruitment and rate coding organization in motor-unit pools. *J Neurophysiol* 70:2470–2488. [Medline](#)
- Gad P, Choe J, Nandra MS, Zhong H, Roy RR, Tai YC, Edgerton VR (2013) Development of a multi-electrode array for spinal cord epidural stimulation to facilitate stepping and standing after a complete spinal cord injury in adult rats. *J Neuroeng Rehabil* 10:2. [CrossRef Medline](#)
- Gardner E, Martin J, Jessel T (2000) The bodily senses. In: *Principles of neural science* (Kandel E, Schwartz J, Jessell T, eds), pp 430–450. New York: McGraw-Hill.
- Gerasimenko YP, Lavrov IA, Courtine G, Ichiyama RM, Dy CJ, Zhong H, Roy RR, Edgerton VR (2006) Spinal cord reflexes induced by epidural spinal cord stimulation in normal awake rats. *J Neurosci Methods* 157:253–263. [CrossRef Medline](#)
- Gerasimenko Y, Gorodnichev R, Machueva E, Pivovarova E, Semyenov D, Savochin A, Roy RR, Edgerton VR (2010) Novel and direct access to the human locomotor spinal circuitry. *J Neurosci* 30:3700–3708. [CrossRef Medline](#)
- Guertin P, Angel MJ, Perreault MC, McCrea DA (1995) Ankle extensor group I afferents excite extensors throughout the hindlimb during fictive locomotion in the cat. *J Physiol* 487:197–209. [Medline](#)
- Harkema S, Gerasimenko Y, Hodes J, Burdick J, Angeli C, Chen Y, Ferreira C, Willhite A, Rejc E, Grossman RG, Edgerton VR (2011) Effect of epidural stimulation of the lumbosacral spinal cord on voluntary movement, standing, and assisted stepping after motor complete paraplegia: a case study. *Lancet* 377:1938–1947. [CrossRef Medline](#)
- Hines ML, Carnevale NT (1997) The NEURON simulation environment. *Neural Comput* 9:1179–1209. [CrossRef Medline](#)
- Hines ML, Morse T, Migliore M, Carnevale NT, Shepherd GM (2004) ModelDB: a database to support computational neuroscience. *J Comput Neurosci* 17:7–11. [CrossRef Medline](#)
- Holsheimer J (1998) Computer modelling of spinal cord stimulation and its contribution to therapeutic efficacy. *Spinal Cord* 36:531–540. [CrossRef Medline](#)
- Holsheimer J (2002) Which neuronal elements are activated directly by spinal cord stimulation. *Neuromodulation* 5:25–31. [CrossRef Medline](#)
- Ichiyama RM, Gerasimenko YP, Zhong H, Roy RR, Edgerton VR (2005) Hindlimb stepping movements in complete spinal rats induced by epidural spinal cord stimulation. *Neurosci Lett* 383:339–344. [CrossRef Medline](#)

- Illis LS, Oygar AE, Sedgwick EM, Awadalla MA (1976) Dorsal-column stimulation in the rehabilitation of patients with multiple sclerosis. *Lancet* 1:1383–1386. [Medline](#)
- Jankowska E (1992) Interneuronal relay in spinal pathways from proprioceptors. *Prog Neurobiol* 38:335–378. [CrossRef Medline](#)
- Ladenbauer J, Minassian K, Hofstoetter US, Dimitrijevic MR, Rattay F (2010) Stimulation of the human lumbar spinal cord with implanted and surface electrodes: a computer simulation study. *IEEE Trans Neural Syst Rehabil Eng* 18:637–645. [CrossRef Medline](#)
- Lavrov I, Gerasimenko YP, Ichiyama RM, Courtine G, Zhong H, Roy RR, Edgerton VR (2006) Plasticity of spinal cord reflexes after a complete transection in adult rats: relationship to stepping ability. *J Neurophysiol* 96:1699–1710. [CrossRef Medline](#)
- Lavrov I, Dy CJ, Fong AJ, Gerasimenko Y, Courtine G, Zhong H, Roy RR, Edgerton VR (2008) Epidural stimulation-induced modulation of spinal locomotor networks in adult spinal rats. *J Neurosci* 28:6022–6029. [CrossRef Medline](#)
- Lyalka VF, Hsu LJ, Karayannidou A, Zelenin PV, Orlovsky GN, Deliagina TG (2011) Facilitation of postural limb reflexes in spinal rabbits by serotonergic agonist administration, epidural electrical stimulation, and postural training. *J Neurophysiol* 106:1341–1354. [CrossRef Medline](#)
- Mailis-Gagnon A, Furlan AD, Sandoval JA, Taylor R (2004) Spinal cord stimulation for chronic pain. *Cochrane Database Syst Rev*:CD003783.
- McCrea DA (2001) Spinal circuitry of sensorimotor control of locomotion. *J Physiol* 533:41–50. [CrossRef Medline](#)
- McCrea DA, Shefchyk SJ, Stephens MJ, Pearson KG (1995) Disynaptic group I excitation of synergist ankle extensor motoneurons during fictive locomotion in the cat. *J Physiol* 487:527–539. [Medline](#)
- McIntyre CC, Grill WM (2002) Extracellular stimulation of central neurons: influence of stimulus waveform and frequency on neuronal output. *J Neurophysiol* 88:1592–1604. [Medline](#)
- McIntyre CC, Richardson AG, Grill WM (2002) Modeling the excitability of mammalian nerve fibers: influence of afterpotentials on the recovery cycle. *J Neurophysiol* 87:995–1006. [Medline](#)
- Minassian K, Jilge B, Rattay F, Pinter MM, Binder H, Gerstenbrand F, Dimitrijevic MR (2004) Stepping-like movements in humans with complete spinal cord injury induced by epidural stimulation of the lumbar cord: electromyographic study of compound muscle action potentials. *Spinal Cord* 42:401–416. [CrossRef Medline](#)
- Minassian K, Persy I, Rattay F, Pinter MM, Kern H, Dimitrijevic MR (2007) Human lumbar cord circuitries can be activated by extrinsic tonic input to generate locomotor-like activity. *Hum Mov Sci* 26:275–295. [CrossRef Medline](#)
- Minassian K, Hofstoetter U, Tansey K, Mayr W (2012) Neuromodulation of lower limb motor control in restorative neurology. *Clin Neurol Neurosurg* 114:489–497. [CrossRef Medline](#)
- Musienko P, van den Brand R, Maerzendorfer O, Larmagnac A, Courtine G (2009) Combinatory electrical and pharmacological neuroprosthetic interfaces to regain motor function after spinal cord injury. *IEEE Trans Biomed Eng* 56:2707–2711. [CrossRef Medline](#)
- Musienko P, Heutschi J, Friedli L, van den Brand R, Courtine G (2012) Multi-system neurorehabilitative strategies to restore motor functions following severe spinal cord injury. *Exp Neurol* 235:100–109. [CrossRef Medline](#)
- Raspopovic S, Capogrosso M, Micera S (2011) A computational model for the stimulation of rat sciatic nerve using a transverse intrafascicular multichannel electrode. *IEEE Trans Neural Syst Rehabil Eng* 19:333–344. [CrossRef Medline](#)
- Raspopovic S, Capogrosso M, Badia J, Navarro X, Micera S (2012) Correction to “Experimental validation of a hybrid computational model for selective stimulation using transverse intrafascicular multichannel electrodes.” *IEEE Trans Neural Syst Rehabil Eng* 20:615. [CrossRef](#)
- Rattay F (1986) Analysis of models for external stimulation of axons. *IEEE Trans Biomed Eng* 33:974–977. [Medline](#)
- Rattay F, Minassian K, Dimitrijevic MR (2000) Epidural electrical stimulation of posterior structures of the human lumbosacral cord: 2. Quantitative analysis by computer modeling. *Spinal Cord* 38:473–489. [CrossRef Medline](#)
- Reeve C, Reeve D (2008) *The spinal cord*. New York: Elsevier.
- Richardson AG, McIntyre CC, Grill WM (2000) Modelling the effects of electric fields on nerve fibres: influence of the myelin sheath. *Med Biol Eng Comput* 38:438–446. [CrossRef Medline](#)
- Roll JP, Vedel JP, Ribot E (1989) Alteration of proprioceptive messages induced by tendon vibration in man: a microneurographic study. *Exp Brain Res* 76:213–222. [Medline](#)
- Roy RR, Matsumoto A, Zhong H, Ishihara A, Edgerton VR (2007) Rat α - and γ -motoneuron soma size and succinate dehydrogenase activity are independent of neuromuscular activity level. *Muscle Nerve* 36:234–241. [CrossRef Medline](#)
- Saywell SA, Ford TW, Meehan CF, Todd AJ, Kirkwood PA (2011) Electrophysiological and morphological characterization of propriospinal interneurons in the thoracic spinal cord. *J Neurophysiol* 105:806–826. [CrossRef Medline](#)
- Schiefer MA, Triolo RJ, Tyler DJ (2008) A model of selective activation of the femoral nerve with a flat interface nerve electrode for a lower extremity neuroprosthesis. *IEEE Trans Neural Syst Rehabil Eng* 16:195–204. [CrossRef Medline](#)
- Schieppati M (1987) The Hoffmann reflex: a means of assessing spinal reflex excitability and its descending control in man. *Prog Neurobiol* 28:345–376. [CrossRef Medline](#)
- Stein RB, Capaday C (1988) The modulation of human reflexes during functional motor tasks. *Trends Neurosci* 11:328–332. [CrossRef Medline](#)
- Struijk JJ, Holsheimer J, van der Heide GG, Boom HB (1992) Recruitment of dorsal column fibers in spinal cord stimulation: influence of collateral branching. *IEEE Trans Biomed Eng* 39:903–912. [CrossRef Medline](#)
- Struijk JJ, Holsheimer J, Boom HB (1993) Excitation of dorsal root fibers in spinal cord stimulation: a theoretical study. *IEEE Trans Biomed Eng* 40:632–639. [CrossRef Medline](#)
- Tresch MC, Kiehn O (2000) Motor coordination without action potentials in the mammalian spinal cord. *Nat Neurosci* 3:593–599. [CrossRef Medline](#)
- Tripodi M, Stepien AE, Arber S (2011) Motor antagonism exposed by spatial segregation and timing of neurogenesis. *Nature* 479:61–66. [CrossRef Medline](#)
- van den Brand R, Heutschi J, Barraud Q, DiGiovanna J, Bartholdi K, Huerliemann M, Friedli L, Vollenweider I, Moraud EM, Duis S, Dominici N, Micera S, Musienko P, Courtine G (2012) Restoring voluntary control of locomotion after paralyzing spinal cord injury. *Science* 336:1182–1185. [CrossRef Medline](#)
- Vleggeert-Lankamp CLAM, van den Berg RJ, Feirabend HKP, Lakke EAJF, Malassy MJA, Thomeer RTWM (2004) Electrophysiology and morphometry of the A α - and A β -fiber populations in the normal and regenerating rat sciatic nerve. *Exp Neurol* 187:337–349. [CrossRef Medline](#)

Editor's Summary

Closing the Loop on Neuroprosthetic Control

Patients with spinal cord injury (SCI) and paralysis may soon be outfitted with so-called neuromodulation devices, which electrically stimulate the brain or spinal cord, causing movement in the legs. Currently, tuning such modulation requires constant observation and patient-specific adjustments, which are not ideal for fluid movement or for broad translation of these technologies to injured patients. In response, Wenger *et al.* have created a closed-loop system that will essentially "auto-tune" the device, allowing the paralyzed patient—or, in their study, the paralyzed rat—to move freely, without worrying about adjusting electrical pulse width, amplitude, or frequency. The authors gave rats complete SCI epidural electrical stimulation and then mapped their leg movements and sensorimotor responses while in a body support system, walking upright (bipedal) on a treadmill, or climbing stairs. From this information, they devised a computational system that integrated feedback and feed-forward models for closed-loop, continuous control of leg movement and, in turn, a more natural locomotion. Closed-loop neuromodulation of spinal circuits could impart fluid motor control and prevent fatigue when rehabilitating patients with SCI.

A complete electronic version of this article and other services, including high-resolution figures, can be found at:

<http://stm.sciencemag.org/content/6/255/255ra133.full.html>

Supplementary Material can be found in the online version of this article at:

<http://stm.sciencemag.org/content/suppl/2014/09/22/6.255.255ra133.DC1.html>

Related Resources for this article can be found online at:

<http://stm.sciencemag.org/content/scitransmed/5/210/210ra155.full.html>

<http://stm.sciencemag.org/content/scitransmed/6/222/222ra19.full.html>

<http://stm.sciencemag.org/content/scitransmed/5/210/210ra154.full.html>

<http://stm.sciencemag.org/content/scitransmed/5/210/210ps15.full.html>

<http://stm.sciencemag.org/content/scitransmed/5/210/210rv2.full.html>

<http://stm.sciencemag.org/content/scitransmed/5/208/208ra146.full.html>

<http://www.sciencemag.org/content/sci/345/6204/1254927.full.html>

Information about obtaining **reprints** of this article or about obtaining **permission to reproduce this article** in whole or in part can be found at:

<http://www.sciencemag.org/about/permissions.dtl>

Closed-loop neuromodulation of spinal sensorimotor circuits controls refined locomotion after complete spinal cord injury

Nikolaus Wenger,^{1*} Eduardo Martin Moraud,^{2,3*} Stanisa Raspopovic,^{2,4} Marco Bonizzato,² Jack DiGiovanna,² Pavel Musienko,^{1,5} Manfred Morari,³ Silvestro Micera,^{2,4†} Grégoire Courtine^{1†‡}

Neuromodulation of spinal sensorimotor circuits improves motor control in animal models and humans with spinal cord injury. With common neuromodulation devices, electrical stimulation parameters are tuned manually and remain constant during movement. We developed a mechanistic framework to optimize neuromodulation in real time to achieve high-fidelity control of leg kinematics during locomotion in rats. We first uncovered relationships between neuromodulation parameters and recruitment of distinct sensorimotor circuits, resulting in predictive adjustments of leg kinematics. Second, we established a technological platform with embedded control policies that integrated robust movement feedback and feed-forward control loops in real time. These developments allowed us to conceive a neuroprosthetic system that controlled a broad range of foot trajectories during continuous locomotion in paralyzed rats. Animals with complete spinal cord injury performed more than 1000 successive steps without failure, and were able to climb staircases of various heights and lengths with precision and fluidity. Beyond therapeutic potential, these findings provide a conceptual and technical framework to personalize neuromodulation treatments for other neurological disorders.

INTRODUCTION

Regulation of dysfunctional neuronal circuits with electrical neuromodulation therapies has broadened the spectrum of treatment options for neurological disorders (1, 2). For example, deep brain stimulation of basal ganglia has become a common medical practice to alleviate motor symptoms of Parkinson's disease (3–6). Experimentally, epidural electrical stimulation (EES) and intraspinal stimulation of the lumbosacral and thoracic spinal segments have enabled improved motor control capabilities in rodents and humans with spinal cord injury (SCI) (7–9) and Parkinson's disease (10, 11). In these experiments, empirical knowledge and visual observations guided the tuning of electrical neuromodulation parameters. After manual adjustment of pulse width, amplitude, and frequency, stimulation of the brain and spinal cord remained constant. Such an approach is likely suboptimal to mediate maximum therapeutic effects in patients (1, 2). Indeed, preliminary evaluations have suggested that nonregular temporal patterns (5, 6) and closed-loop adjustment (4, 12) of deep brain stimulation augment the therapeutic impact of neuromodulation.

The ability to modulate the parameters and timing of EES of lumbosacral circuits to improve motor control after SCI remains unclear. Various studies have shown that tuning frequency, amplitude, and pulse width of EES can modulate specific aspects of standing, stepping, and isolated movements in both animal models and humans (8, 13–15).

However, to our knowledge, a comprehensive mapping of the functional relationships between stimulation parameters and limb kinematics that could be leveraged to achieve closed-loop control of EES has not been conducted.

Several limitations have restricted the development of closed-loop control systems for neuromodulation (16). First, efficient control policies require a mechanistic understanding of the relationships between stimulation features, the recruitment of specific sensorimotor circuits, and the resulting functional effects. Second, closed-loop control of neuromodulation relies on the availability of a stable and robust feedback signal to tune stimulation parameters. Third, implementation and optimization of closed-loop control algorithms necessitate advanced technological platforms combining feedback and feed-forward loops that match the natural flow of information in the modulated neural systems. Here, we sought to address these issues simultaneously to modulate lumbosacral circuits through closed-loop EES.

Previous studies using EES to improve standing and walking in severely paralyzed subjects have operated under the assumption that the stimulation primarily increases the general level of excitability within spinal circuits (8) and activates central pattern generators (13). However, EES is also able to recruit specific afferent pathways connected to distinct sensorimotor circuits, which, in turn, generate well-defined responses in leg muscles after each pulse of stimulation (17–19). We first capitalized on this understanding of EES mechanisms to establish a mapping between EES parameters, neuromodulation of sensorimotor circuits, and adjustments of leg movements. Second, we developed robust algorithms to extract a useful feedback signal from spatiotemporal characteristics of leg kinematic during locomotion. Third, we established a versatile technological platform with embedded control policies that interfaced feedback signals and feed-forward models operating in real time. These integrated developments allowed us to conceive a closed-loop neuromodulation system that controlled a broad range of leg movements during natural locomotion in paralyzed rats.

¹International Paraplegic Foundation Chair in Spinal Cord Repair, Center for Neuroprosthetics and Brain Mind Institute, Swiss Federal Institute of Technology (EPFL), Lausanne CH-1015, Switzerland. ²Translational Neural Engineering Lab, Center for Neuroprosthetics and Institute of Bioengineering, School of Bioengineering, Swiss Federal Institute of Technology (EPFL), Lausanne CH-1015, Switzerland. ³Automatic Control Laboratory, Swiss Federal Institute of Technology (ETHZ), Zurich CH-8092, Switzerland. ⁴The BioRobotics Institute, Scuola Superiore Sant'Anna, Pisa IT-56025, Italy. ⁵Pavlov Institute of Physiology, St. Petersburg RU-100034, Russia.

*These authors contributed equally to this work.

†These authors contributed equally to this work.

‡Corresponding author. E-mail: gregoire.courtine@epfl.ch

RESULTS

Modulation of EES parameters tunes specific aspects of leg movements

We first characterized the impact of EES amplitude, pulse width, and frequency on the modulation of leg kinematic, ground reaction force, and muscle activity in adult rats that received a complete transection of the mid-thoracic spinal cord (fig. S1). After 5 weeks of recovery, all of the tested rats ($n = 5$) dragged both hindlimbs along the treadmill belt when supported bipedally in a robotic body weight support system (Fig. 1A). The combination of serotonin agonists (5HT_{1A/2/7}) and EES delivered at S1 and L2 spinal segments (Fig. 1B) promoted continuous and alternating stepping movements of the legs. Frequency, amplitude, and pulse width of EES were adjusted to cover the entire range of values that promoted functional movements.

Increments of EES frequency led to a graded and consistent modulation of gait patterns in all the tested rats within a range of 20 to 90 Hz (Fig. 1, C and D). To characterize this modulation and identify the most relevant features reflecting tuning of leg movements with EES frequency, we computed 147 kinematic, force, and electromyographic (EMG) variables that provided a comprehensive description of the locomotor state (listed in table S1). We subjected these combined parameters to a PC analysis. Stepping patterns associated with each EES frequency were differentiated along PC1, which explained nearly 50% of the total variance in the data sets (Fig. 1D). Analysis of factor loadings on PC1 revealed that step height was the more robust variable (factor loading, 0.97) to capture the modulation of leg movements during changes in EES frequency (fig. S2). There were linear correlations between EES frequency and step height that were reproducible within a session (Fig. 2A), over weeks (Fig. 2A), and among rats (Fig. 2B), despite idiosyncratic gait patterns. Tuning EES frequency over the useful range of values (shaded areas in Fig. 2A) mediated a threefold increase in foot elevation, which allowed rats to cover step heights ranging from 2.9- to 6.8-cm mean across rats.

Increase in EES amplitude (Fig. 3, A to C) mediated adjustments of lower limb kinematics similar to those observed with changes in EES frequency, including a significant, albeit limited increase in step height (2.8 to 3.9 cm) (Fig. 3C). Changes in limb kinematics were less systematic when adjusting pulse width (Fig. 3, D to F). Moreover, increase in EES amplitude and pulse width induced coactivation of leg muscles (Fig. 3, A and D), which led to a rapid saturation of stepping movements, and thus limited the relevance of these parameters for neuro-modulation strategies.

EES frequency modulates specific sensorimotor circuits

We next sought to identify the physiological principles underlying the modulation of step height with EES frequency. EES primarily recruits proprioceptive afferent fibers (17, 19, 20). Here, we found that the recruitment of proprioceptive fibers engages monosynaptic and polysynaptic reflex circuits, which elicited well-defined motor responses in leg muscles after each pulse of EES (Fig. 4A). We dissociated these responses functionally based on their respective latencies (medium- and late-latency responses). In turn, phase-dependent modulation of these responses in flexor versus extensor muscles resulted in alternating bursts of EMG activity, enabling continuous locomotion in otherwise paralyzed rats (Fig. 4B and fig. S3, A and B).

EES-induced motor responses remained locked to each pulse of stimulation across the entire range of tested EES frequencies (Fig. 4,

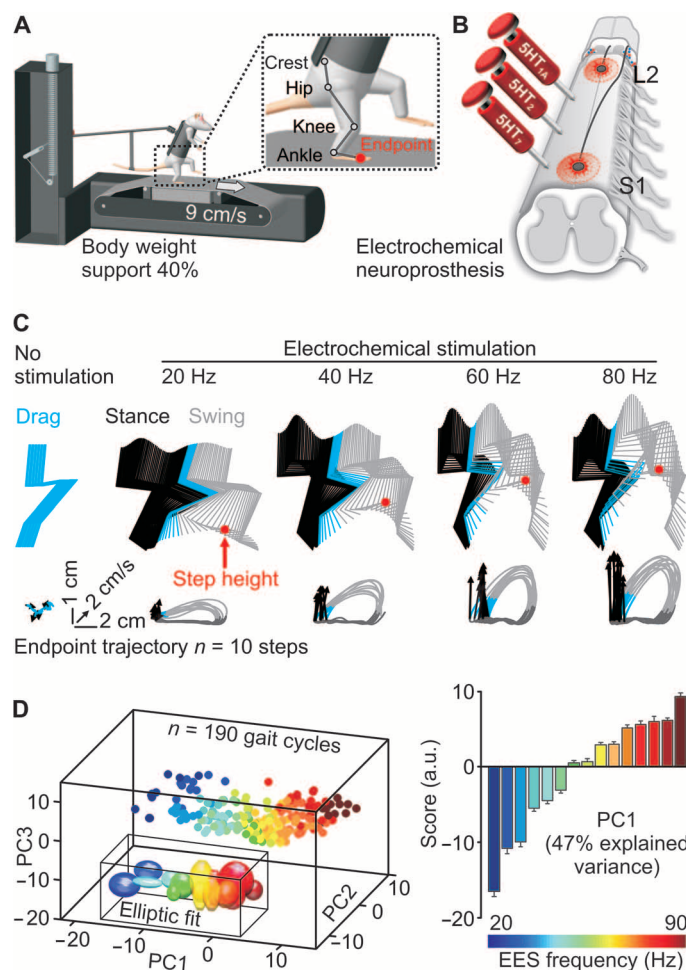


Fig. 1. Modulation of EES frequency tune foot trajectory during locomotion. (A) Rats with complete SCI were positioned bipedally over a treadmill belt using an adjustable body weight support system. In the inset, markers were positioned over leg joints, including the limb endpoint. (B) EES was applied along the midline of L2 and S1 spinal segments. Serotonin agonists (5HT) were administered systemically before stepping. (C) Representative, color-coded stick diagram decomposition of hindlimb movements during stance (black), drag (cyan), and swing (gray), together with 10 successive trajectories of the limb endpoint. The red dot indicates the maximum step height. The black arrows represent the direction and intensity of the limb endpoint trajectory at swing onset. (D) Principal component (PC) analysis applied on all 147 gait variables (table S1) measured over 10 successive gait cycles during EES frequencies ranging from 20 to 90 Hz, with a 5-Hz increment for a representative rat. Least-square elliptical fits are drawn to emphasize frequency-dependent modulation of gait patterns. The bar graph reports the score for each EES frequency along PC1. Data are means + SEM. a.u., arbitrary units.

B and C). Consequently, increment of EES frequency induced a graded increase in the number of medium- and late-latency responses in leg muscles (Fig. 4, C and D, and fig. S3C). At the lower frequencies, both responses independently contributed to the elaboration of muscle activity in both flexor and extensor muscles (fig. S3D). At higher frequencies, the monosynaptic input likely reached motoneurons at the same time as the polysynaptic input from the preceding stimulation. Temporal convergence of monosynaptic and polysynaptic inputs onto

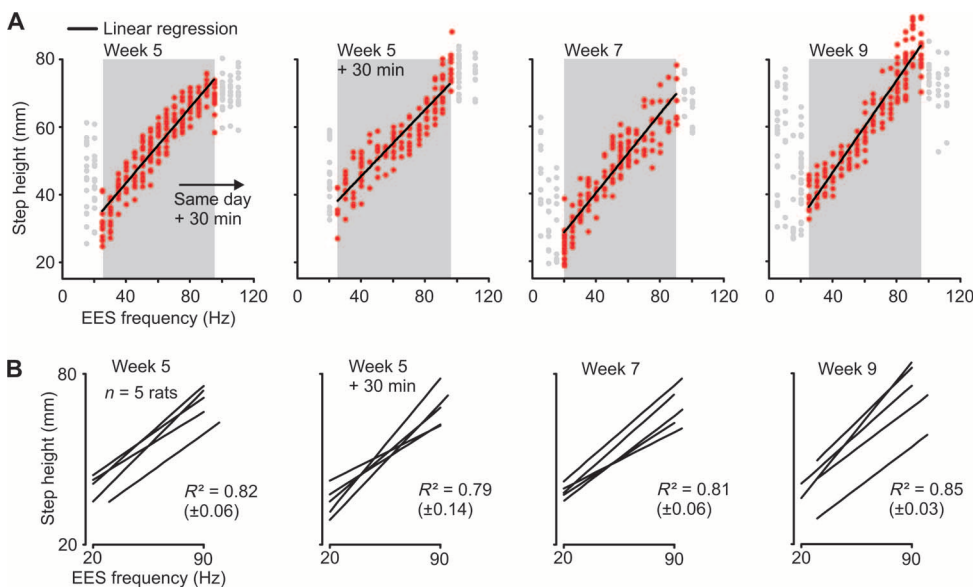


Fig. 2. Reproductive modulation of step height with EES frequency within and across days, and between rats. (A) Relationship between EES frequency and step height for a representative rat tested 30 min apart in the same session 5 weeks post-lesion, and at 7 and 9 weeks post-lesion. The linear regression (back line) was computed over the range of functional EES frequencies (red dots, shaded areas). Each dot represents a gait cycle. (B) Plots reporting the linear regressions from five rats recorded in the same conditions as in (A).

motoneurons eventually led to a single, medium-latency response, which accounted for the increase in the amplitude of this response with larger EES frequencies (fig. S3, C and D).

The graded increase in the number and amplitude of motor responses led to a linear enhancement of the overall bilateral EMG activity in extensor and flexor ankle muscles (Fig. 4E and fig. S3D). In turn, the concurrent modulation of ankle extensors in the stance leg and flexor muscles in the swing leg accounted for the progressive tuning of step height when adjusting EES frequency (Fig. 4E). These results indicate that tuning of EES frequency mediates a progressive and reproducible modulation of monosynaptic and polysynaptic reflex circuits, which promotes predictive adjustment of leg movements during locomotion in rats.

Closed-loop EES achieves high-fidelity control of leg movements

Linear tuning of step height with increase in EES frequency opened the intriguing possibility to automate leg movement control in real time through closed-loop modulation of EES frequency. To test this hypothesis, we designed a technological platform that combined (i) online monitoring of kinematics, ground reaction force, and muscle activity in real time; (ii) signal-processing algorithms to reconstruct locomotor states, including limb endpoint trajectory, gait phases, and whole-body position; and (iii) a computational infrastructure to embed control policies in the feedback loop to adjust EES frequency based on current and desired stepping behaviors (Fig. 5A, fig. S4, and movie S1). Optimization of communication protocols and information-processing time allowed the entire loop to operate in less than 20 ms (see Materials and Methods), which was appropriate for real-time control of neuromodulation during gait despite the fast rhythm of stepping in rats (cycle duration, 810 ± 156 ms, SD).

We used this real-time platform to implement a closed-loop control policy capable of adjusting step height in real time during locomotion. The continuous flow of kinematic information was discretized per gait cycle and merged into a single variable (step height) that was used to automatically adjust EES frequency during the next gait cycle (Fig. 5A). The controller adjusted stimulation to maintain the maximum elevation of the foot within a reference band, whose upper and lower bounds (± 5 mm) were selected to account for the intrinsic variability of step height during continuous locomotion (4.6 ± 0.9 mm, SD). This single-input single-output (SISO) control structure integrated parallel loops combining adaptive feed-forward prediction and feedback correction (Fig. 5A and fig. S4).

The feed-forward model was derived from the linear correlation between step height and EES frequency recorded for each rat at the beginning of each session (Fig. 2). The slope and intercept values of the model were iteratively updated after each gait cycle to account for time-varying changes in stepping behavior. A proportional-integral (PI) feedback loop complemented the feed-forward model predictions to minimize the discrepancy between the desired and actual step height (movie S1). This architecture achieved a high degree of control over a broad range of step heights during both steady and constantly changing locomotor states (Fig. 5, B and C).

To quantify the degree of step height control, we designed a comprehensive suite of testing paradigms, in which the reference band was displaced through a range of fixed increments or decrements after each step, or after a series of steps (Fig. 5C). These tasks tested the performances of the controller during steady-state (fig. S5A) and dynamic (fig. S5, B and C) behaviors over the entire range of step height modulations. Despite these multifaceted challenges, the controller successfully tuned EES frequency to instantly adjust step height to varying reference bands (movie S2). Precision of step height control significantly increased in variability (fig. S5D) when imposing adjustments that reached the physiological limits of the studied biomechanical system.

Closed-loop EES prevents rapid fatigue during continuous locomotion

We next sought to evaluate the ability of closed-loop EES to improve key aspects of gait performance. Human patients with SCI exhibit a rapid exhaustion of locomotor output during continuous stepping on a treadmill (21), which is also observed in injured rats (22). During noncontrolled EES (40 Hz), rats with complete SCI showed a progressive decrease in the amplitude of muscle activity during stepping (Fig. 6, A and B), which led to a graded decrease in step height until the animals collapsed (Fig. 6C).

Instead, closed-loop control of step height doubled the duration of stepping before collapse compared to noncontrolled EES (Fig. 6C). The controller continuously increased EES frequency over time, which limited the decrease in the amplitude of muscle activity (Fig. 6B), and

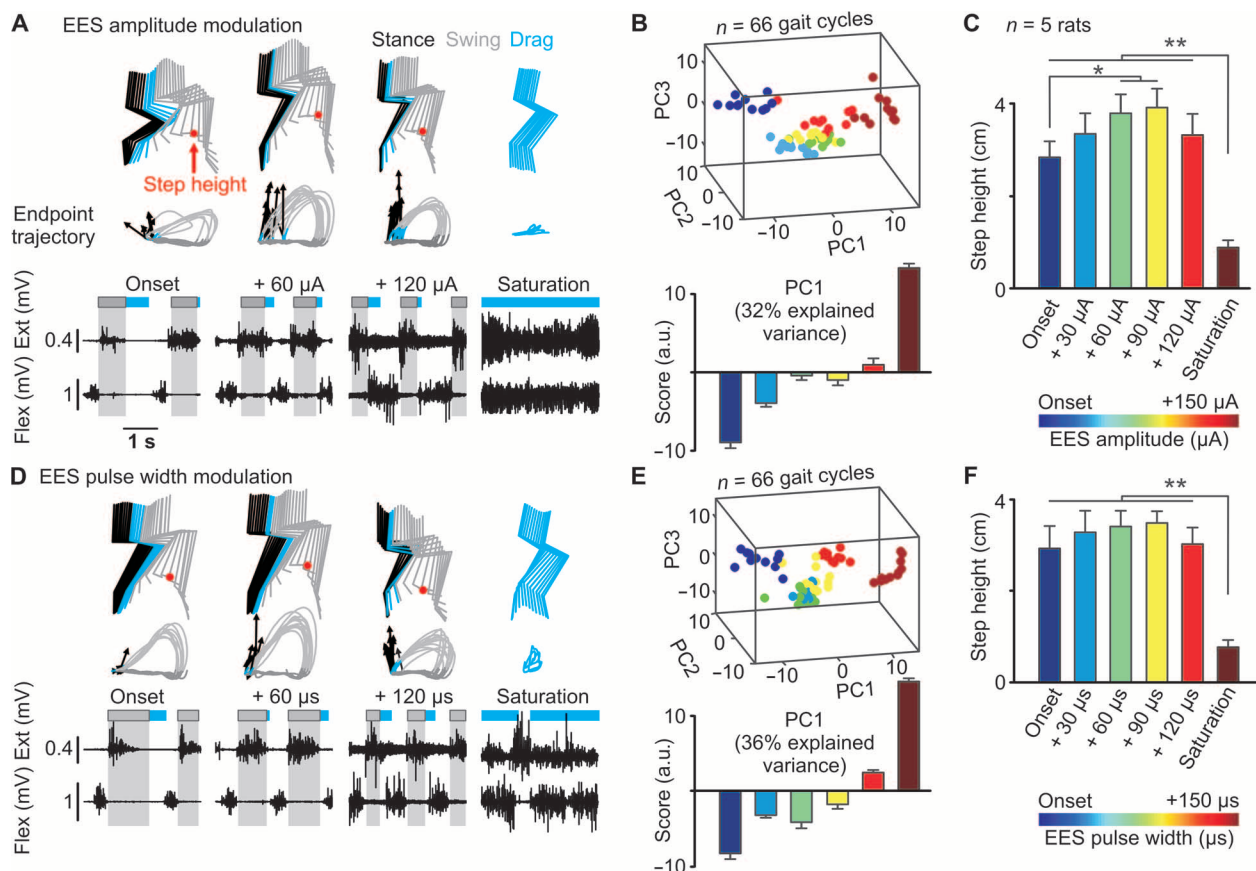


Fig. 3. EES amplitude and pulse width mediate limited tuning of leg movements during locomotion. (A) EES amplitude was gradually increased by fixed increments of 60 μA from the onset of EES-induced stepping, until saturation. EES frequency was kept constant at 40 Hz. Stick diagram decomposition of hindlimb movements, successive limb endpoint trajectories, and alternating flexor (Flex) and extensor (Ext) EMG activity are displayed for each experimental condition using the same convention as in Fig. 1. (B) PC analysis was applied on all the gait variables measured in a representative rat during EES amplitude changes shown in (A). The bar

enabled rats to maintain step height within the constant reference band for extended durations despite exhaustion (Fig. 6C and movie S3). Under controlled conditions, 100% of the tested rats ($n = 3$) performed at least 1000 successive steps without failure over the duration of the testing session.

Closed-loop EES enables locomotion across combinations of staircases

We lastly aimed to illustrate the practical impact of closed-loop EES to restore walking during more natural locomotor conditions. For this, we positioned the rats overground in a robotic interface that moved the rats forward along a runway while providing constant-force support in the vertical (25% of body weight) and mediolateral (rigid, 100%) directions (Fig. 7A). We interposed staircases of various heights (1.3 to 3.5 cm), lengths (12 to 25 cm), and numbers (one to four stairs) along the runway to test the ability of closed-loop EES to modulate step height to accommodate leg movements during stair climbing. The reference band was set at a constant height during locomotion along the horizontal surface until crossing a predefined distance from

graph reports the score for each EES amplitude along PC1 for all tested rats ($n = 5$). (C) Histogram plots reporting changes in step height in response to modulation of EES amplitude. (D) EES pulse width was gradually increased by fixed increments of 60 μs in the same rat and under the same conditions as (A). (E) PC analysis was applied on all the gait variables measured during EES pulse width changes shown in (D). (F) Histogram plots reporting changes in step height in response to modulation of EES pulse width. * $P < 0.05$, ** $P < 0.01$, repeated-measures analysis of variance (ANOVA) with Bonferroni post hoc analysis. Data are means \pm SEM ($n = 5$).

the staircase (1.5 cm) where the reference band was raised to an appropriate height (3 cm above staircase height) to pass the staircase. During noncontrolled EES, rats tumbled against and failed to pass the lower staircase (Fig. 7A). In contrast, closed-loop EES enabled the rats ($n = 3$) to climb all of the tested staircase combinations successfully in 99 of 100 successive attempts ($P < 0.001$ versus noncontrolled EES, Kruskal-Wallis test) (Fig. 7, A and B, and movie S4).

Automated tuning of EES frequency during the stance phase preceding the staircase significantly augmented vertical ground reaction forces proportional to the displacement of the reference band (Fig. 7B), which generated the adequate foot trajectory to overcome the staircase. The same precision of step height control was obtained during sequences of staircases, which required a continuous adjustment of EES frequency to pass the successive stairs while stabilizing upward and downward movements of the body after each step (fig. S6). These combined results show the ability of the developed neuromodulation algorithms to achieve real-time adjustment of leg kinematic and ground reaction forces with adequate precision to restore complex walking behaviors in paralyzed rats.

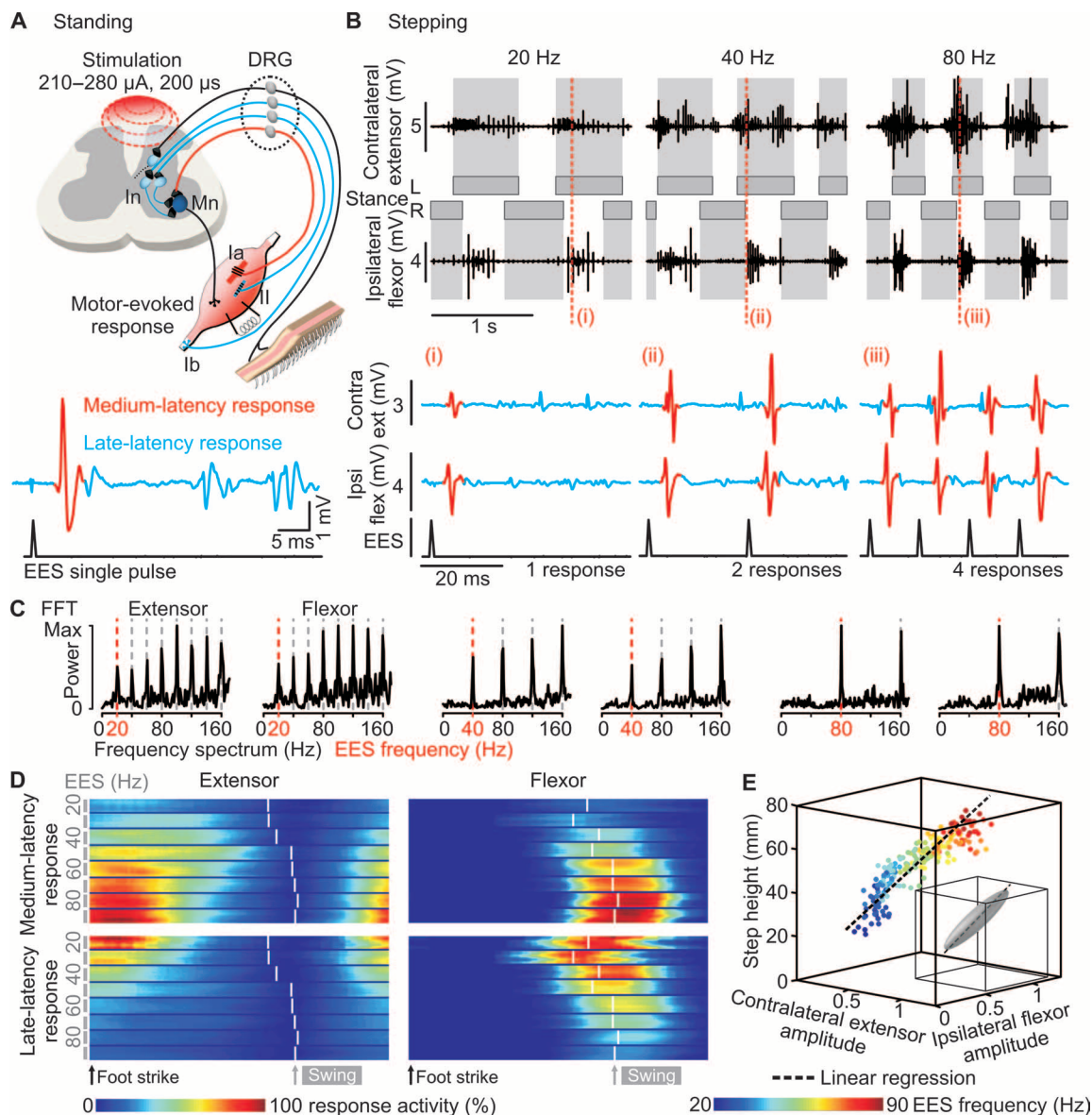


Fig. 4. EES frequency modulates specific reflex circuits. (A) Schematic of neural structures recruited by EES. In, interneuron; Mn, motoneuron; DRG, dorsal root ganglion; Ib, group Ib fibers conveying force feedback; Ia and II, group Ia and group II fibers conveying muscle length-related feedback. A single pulse of EES evokes a medium-latency response (red) and a late-latency response (blue) in leg muscles through activation of proprioceptive segmental circuits. (B) Sequence of EMG activity recorded in the contralateral extensor (medial gastrocnemius) and ipsilateral flexor (tibialis anterior) muscles during continuous stepping at three different EES frequencies. The lower traces show, for each frequency, motor responses evoked in extensor (ext) and flexor (flex) muscles at distinct moments of the gait cycle (i, ii, and iii), but over the same duration. (C) Power spectrum

of EMG bursts for flexor and extensor muscles at different stimulation frequencies. The red and gray vertical lines indicate EES frequency and its harmonic multiples, respectively. (D) Color-coded modulation of the amplitude of medium- and late-latency responses in flexor and extensor muscles over the course of a gait cycle for EES frequencies ranging from 20 to 90 Hz, with a 10-Hz increment. The white lines indicate the end of stance for each frequency. (E) Three-dimensional (3D) linear correlation between color-coded EES frequency and normalized EMG amplitude of contralateral extensor and ipsilateral flexor muscles. Each point represents an individual gait cycle. The robustness of the correlation was calculated through PC analysis as the amount of explained variance by PC1. All panels report data recorded in the same representative rat (representative of $n = 5$).

DISCUSSION

Open-loop regulation of spinal sensorimotor circuits with neuromodulation therapy improves motor control after SCI (7, 8, 14, 23). Here, we demonstrate that closed-loop neuromodulation yielded superior control of leg movement compared to continuous stimulation, enabling rats

with complete SCI to perform complex locomotor tasks with precision and fluidity. Although the current demonstration is in rodents, research platforms for human spinal cord stimulation (16) and a newly developed robotic interface (24) provide the technological infrastructure to achieve immediate translation of our control algorithms into neuromodulation therapies to facilitate robot-assisted training in humans with SCI.

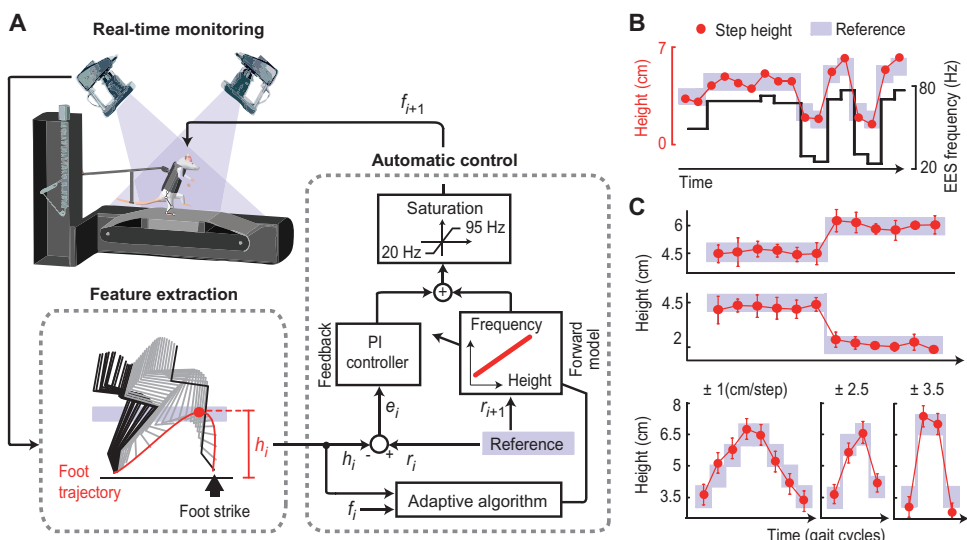


Fig. 5. Real-time control of step height during locomotion. (A) The architecture of the closed-loop system combined real-time monitoring of kinematic information and automated control policies. After each foot strike, the signal-processing algorithm measured the step height (red dot, h_i), which was fed into the control loop. The control structure integrated parallel loops combining feedback correction (PI controller) and a predictive forward model. This predictive component was elaborated from the linear relationship between EES frequency and step height, and was updated at each iteration through an adaptive algorithm (see Materials and Methods). The controller combined the error (e_i) correction based on the current reference (r_i), and the prediction to generate the adjustment of EES frequency (f_{i+1}) to adjust the current frequency (f_i) and thus maintain the maximum step height within the user-defined reference band (r_{i+1} , shaded areas). A saturation function was inserted to constrain EES within the functional range of frequencies. (B) Example of successive step heights and concomitant EES frequencies during a random sequence of reference band changes for one rat. (C) Mean values \pm SEM ($n = 15$ trials) of successive step heights for various combinations of steady and constant-changing reference bands (shaded area).

EES of lumbosacral circuits facilitates locomotion through the recruitment of proprioceptive afferent fibers, which engages two complementary mechanisms (17). First, the propagation of the tonic neural drive elicited along myelinated afferent fibers activates central pattern-generating networks (25, 26). Second, each stimulation pulse elicits a medium- and late-latency response in leg muscles, which corresponds to the activation of monosynaptic and polysynaptic reflex circuits, respectively (13, 17, 19). Central pattern-generating networks modulate the gain of these reflex circuits according to the state of the locomotor system (19, 27). In turn, the successive motor responses compose the bursts of leg muscle activity during locomotion (17, 19). Here, we found that spinally evoked motor responses remain locked to the stimulation rate over a large range of frequencies, enabling fine-tuning of muscle activity through linear adjustment of stimulation. Likewise, frequency-dependent modulation of intraspinal microstimulation delivered in cervical segments near-linearly adjusts the amount of grasp force in anesthetized nonhuman primates (28). This principle underlies natural muscle force production, which primarily relies on the modulation of motoneuron firing rate (29).

We leveraged this mechanistic framework to achieve real-time control of lower limb kinematics and vertical ground reaction forces during continuous locomotion. This control policy allowed paralyzed rats to produce a broad range of foot trajectories during continuous locomotion, and to climb combinations of staircases. Frequency-dependent tuning functions were consistent across days and across rats, which supported the design of algorithms with robust performances. This treat-

ment paradigm engages central pattern-generating networks (30). In addition, each pulse elicits monosynaptic and polysynaptic motor responses, which are modulated according to the phase of the movement. Because the human spinal cord exhibits similar responses to EES (23, 31), our approach—frequency-dependent tuning of muscle activity—could translate into a neuromodulation therapy to improve motor control and rehabilitation in patients with SCI.

Previous closed-loop neuromodulation therapies for restoring locomotion using electrical stimulation of muscles (32, 33) or spinal structures (9) have sought to elaborate the motor command extrinsically through finite-state control of discrete stimulation sequences. This type of control policies enabled stepping-like movements, but was not able to modulate muscle activity to produce movement over a broad range of natural gait trajectories. Moreover, rapid muscle fatigue prevented locomotor execution over extended durations (32, 33), which limited the use of this therapeutic strategy for rehabilitation in humans with SCI (34). Instead, our neuromodulation therapy exploits the intrinsic capacities of sensorimotor circuits embedded in the spinal cord to generate coordinated movements. Thus, we superimposed a

simple control policy onto the ongoing motor program to achieve continuous, high-fidelity control of leg movements over extended periods of time.

Our control policy combined feedback signals and feed-forward models that relied on a global parameter capturing the targeted locomotor behavior. For this purpose, we extracted spatiotemporal features from lower limb endpoint trajectories. There is evidence that central nervous system circuits may elaborate an explicit representation of limb endpoint kinematics (35). Moreover, neurobehavioral experiments have suggested that the limb endpoint is the primary variable used to coordinate locomotion in animal models (36) and humans (37). We thus monitored and controlled step height, which was the most robust parameter to account for frequency-dependent modulation of gait. In addition, lower limb endpoint is a neurally relevant variable to encode and organize leg movements. This type of control policy establishes a framework to design a corticospinal neuroprosthesis through which neuronal modulations from the motor cortex will directly modulate electrical spinal cord stimulation to adjust lower limb kinematics and improve locomotor recovery (38). Current wearable and implantable motion sensors can generate the necessary feedback to incorporate automated closed-loop control policies into neuromodulation therapies for use outside laboratory environments (39). For this purpose, industrial development of clinically viable neuromodulation platforms has established the appropriate neurotechnology to personalize stimulation algorithms based on feedback signals (16).

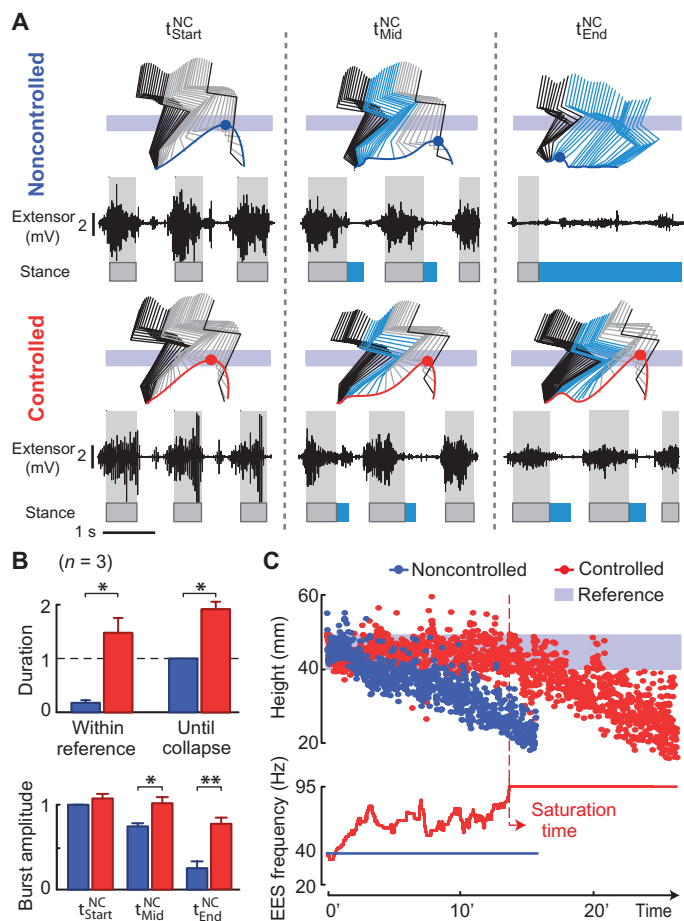


Fig. 6. Closed-loop EES compensates for exhaustion. (A) Stick diagram decomposition of hindlimb movements and extensor muscle activity for both noncontrolled and controlled conditions at three different time points: beginning, middle, and end of the noncontrolled session. Conventions are the same as in Fig. 1C. The gray- and cyan-shaded areas indicate the duration of the stance and drag phases, respectively. The reference (gray band) was set on the basis of the average step height measured across rats. (B) Histogram plots reporting the durations of stepping until collapse and within the reference band, and the amplitude of extensor muscle activity (medial gastrocnemius, MG) for the three time points shown in (A) during noncontrolled and controlled conditions for all the rats ($n = 3$ rats). (C) Representative examples of successive step heights and EES frequency modulation during a continuous sequence of stepping under noncontrolled and controlled conditions. The vertical dotted line corresponds to the saturation time when EES frequency reached the maximum allowed value for the controller, that is, 95 Hz (Fig. 5A). Each data point corresponds to a gait cycle. Data are means \pm SEM. * $P < 0.05$, ** $P < 0.01$, Kruskal-Wallis test.

Current knowledge of human spinal cord properties in response to electrical neuromodulation (23, 31) suggests that the control policies developed in our study could translate into clinical applications for facilitating neurorehabilitation (8, 23). Existing technological platforms for closed-loop neuromodulation of the human nervous system (16) can readily be interfaced with real-time kinematic feedback to tune EES in clinical settings. Moreover, our results in rats (40) compelled the development of a robotic body weight support system that can provide patients with adjustable, multidirectional support during overground

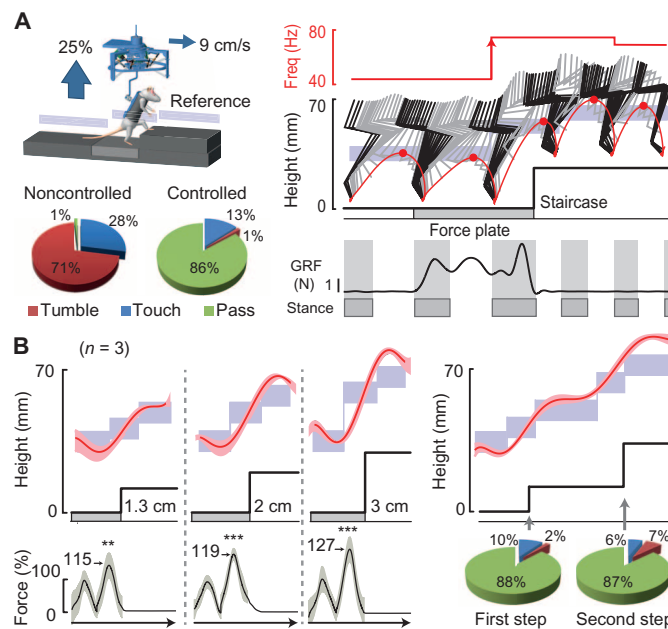


Fig. 7. Real-time control of locomotion across staircases. (A) Rats with complete SCI were attached to a robotic postural interface that provided adjustable, constant-force support in the vertical and mediolateral directions while moving the animal forward at a constant speed (9 cm/s). The reference band was displaced when crossing a virtual line located 1.5 cm away from each staircase. Stick diagram decomposition of hindlimb movements is shown together with EES frequency modulation during a representative execution along a staircase. Changes in vertical ground reaction forces (GRFs) when stepping onto the force plate are displayed at the bottom. Shaded areas indicate the occurrence of stance. The pie plots report the percentage of trials during which the rats ($n = 3$ rats) tumbled, touched, or passed the staircase across 100 successive repetitions under noncontrolled and controlled conditions. (B) Polynomial fit of step height values during locomotion along staircases of various heights and numbers. The concurrent vertical ground reaction forces measured during the step preceding and coinciding with the staircase are displayed at the bottom. Automated tuning of EES frequency significantly augmented vertical ground reaction forces proportional to the displacement of the reference band (** $P < 0.01$, *** $P < 0.005$, Kruskal-Wallis test for each staircase). Data are averages ($n = 3$ rats, 20 trials per rat) and SEM (shaded areas). The pie plots report the percentage of success for the first and second staircases over 20 successive trials.

locomotion within a large workspace (24). Thus, our developed algorithms can be implemented to facilitate rehabilitation during robot-assisted locomotion on a treadmill and overground in patients with SCI. Closed-loop neuromodulation of spinal circuits has the potential to improve motor control and prevent rapid fatigue during robot-assisted training in individuals with incomplete SCI, such as ASIA-C (American Spinal Injury Association grade C) patients, which are essential factors to promote activity-dependent plasticity and recovery with rehabilitation (8, 41).

In rats with complete SCI, continuous weight-bearing stepping only emerged in the presence of agonists to specific serotonergic receptor subtypes. Monoaminergic replacement therapies are necessary to mediate locomotor permissive states of spinal circuits deprived of any source of modulation (42). Consequently, closed-loop neuromodulation therapies in humans with severe injuries will be contingent on the development of safe and efficacious monoaminergic replacement strategies,

which are under exploration (43), but do not yet exist for general use in people. However, open-loop electrical neuromodulation of spinal circuits instantly restored fine control over joint-specific movements in patients with chronic motor paralysis (23). These results suggest that the therapeutic effects of neuromodulation therapies that we demonstrated in rodent models (7) also applied in humans with severe SCI.

Neuromodulation therapies of the brain and spinal cord target distinct neural structures, but share common principles, including the growing need for closed-loop regulation (1, 2, 44). Our results provide a conceptual and technical framework for the broad development of closed-loop neuromodulation therapies to improve function after neurological disorders.

MATERIALS AND METHODS

Study design

The study was segregated into two experimental groups. Characterization of relationships between EES frequency and gait pattern modulation was conducted on a group of five rats that participated in all of the testing sessions over a period of 3 weeks, starting 5 weeks post-lesion. After comprehensive analysis of EES characterization and neuromodulation algorithm development, we generated an additional group of three rats that were tested daily over a period of 4 weeks, starting 5 weeks post-lesion. All experiments involving real-time control of EES were carried out with those three rats. This sample size was selected on the basis of the robustness of EES modulation effects and to obtain enough statistical power to demonstrate significant differences between closed- and open-loop neuromodulation. All the tested rats are presented in the study. No statistical outliers were excluded. One animal from the second group had to be excluded from PC analysis owing to a mechanical failure in one of the four EMG wires; however, this rat could be included for analysis in all other figures where unilateral EMG signals were sufficient for data analysis. All measurements were obtained using objective readouts with high-precision equipment. Blinding during data acquisition and analysis was not possible because of the obvious effects of EES modulation.

Animals and animal care

All procedures and surgeries were approved by the Veterinarian Office Vaud, Switzerland. The experiments were conducted on adult female Lewis rats (~200 g of body weight, Centre d'Elevage R. Janvier). Rats were housed individually on a 12-hour light-dark cycle, with access to food and water ad libitum.

Surgical procedure and post-surgical care

All surgical procedures have been described in detail previously (7, 40) and are elaborated in the Supplementary Methods

Locomotor training

Rats were attached to an automated, servo-controlled body weight support system (Robomedica), and positioned over a motorized treadmill belt for bipedal locomotion. The animals were trained every other day, 20 min per session for 4 weeks, starting 8 days post-SCI. Locomotor training was enabled by the combination of EES at S1 and L2, and systemic administration of agonists to 5HT_{1A/7} (8-OH-DPAT, 0.05 to 0.1 mg/kg body weight) and 5HT_{2A/C} (quipazine, 0.2 to 0.3 mg/kg body weight) receptor subtypes (42). Treadmill belt speed was set at 9 cm/s.

Kinematic, ground reaction force, reflex analysis, and EMG recording procedures as well as data and PC analyses are described in the Supplementary Materials.

Real-time platform for closed-loop adjustment of EES

The platform was implemented within a multithreaded C++ code (Visual Studio 2010, Microsoft) running on a quad core Microsoft Windows 7 computer. Stimulation patterns were applied via an RZ5 processing unit (Tucker-Davis Technologies) connected to an MS16 Stimulus Isolator (Tucker-Davis Technologies). The integrated Vicon recording system generated raw 3D positions of the markers, which were imported into the C++ environment in (soft) real time via Ethernet using the DataStream SDK software. We developed a custom algorithm for online interpolation of missing markers through triangulation and relabeling of each marker to the appropriate joint landmark. All signals were filtered online using least mean squares adaptive filters. Specific gait events such as foot strike, toe-off, or predetermined timings during each gait cycle were automatically detected using online kinematic classification of limb endpoint trajectories. These timings triggered controller calculations and model updates (fig. S3). To evaluate the delay of the entire platform, we sent concomitant pulses at opposite ends of the loop, and calculated the discrepancy between both signals after each iteration, for more than 100 successive cycles.

Control structure for closed-loop adjustment of EES

We modeled stepping patterns as a discrete-time, SISO system (stimulation frequency/step height). The continuous flow of kinematic information was discretized by gait cycles using foot strike events, which separated consecutive gait cycles and defined the set of sampling times $K = \{k_1, k_2 \dots k_n\}$. These events triggered the update of the stimulation frequency, which was applied using zero-order hold control until the next event. The maximum step height during each gait cycle (defined as $h_i = \max(h_t), t \in [k_{i-1}, k_i]$) served as feedback signal for closed-loop corrections. Stimulation values were set identically for both electrodes and effectively acted as a unique value. The controller used an adaptive input-output forward model built from the linear correlations between stimulation frequency and step height. Regression estimates (slope \hat{a}_i and intercept \hat{b}_i) were initially set for each subject based on offline analyses. These values were iteratively updated at every gait cycle using online adaptive filters (least mean squares):

$$\hat{a}_{i+1} = \hat{a}_i + \mu h_i e_i$$

where $\mu = 0.1$ is the forgetting factor, and e_i is the error between recorded and desired outputs at time i . This feed-forward control loop enabled to predict and anticipate the necessary changes in stimulation output. It was combined with a PI feedback loop to correct for unmodeled discrepancies. Values for the proportional (k_p) and integral (k_i) corrections were set manually for each rat on the first experimental session ($k_p = 0.2$ to 0.35 , $k_i = 0.1$ to 0.15), and kept constant during the duration of the recordings. The final stimulation frequency was computed on the basis of the combined feedback and feed-forward components to track a user-defined reference value r_{i+1} for the maximum foot height during the next gait cycle:

$$f_{i+1} = (r_{i+1} - \hat{b}_{i+1})/\hat{a}_{i+1} + (k_p e_i + k_i E_i)$$

where E_i is the cumulative error at time i , and is iteratively calculated as $E_i = i^{-1} \sum_{j=1}^i E_{i-1} + 1/i e_i, i > 0$. The reference included a dead band

($db = 5$ mm), which was included above and below the reference value to account for the inherent variability in stepping when calculating tracking errors: $e_i = \max(0, |r_i - h_i| - db)$. Final stimulation values were applied within the range of values efficient to promote functional locomotor movements, spanning from 20 Hz onset to 95 Hz saturation (movie S1). The amplitude of the current delivered through each electrode was calibrated at the beginning of each experimental session to obtain optimal facilitation of locomotion at baseline frequency based on visual observation. The real-time platform and control structure are represented and further explained in fig. S4.

Treadmill paradigm

Rats were tested in the same conditions as training. Serotonin agonists were administered 10 min before recording onset. Various experimental conditions were tested during each session that lasted 60 min. The first series of experiments evaluated the functional effects of varying amplitude, pulse width, and frequency of EES. For each session, optimal features for the three parameters of EES to promote robust stepping patterns were searched through visual observations. After this preparatory phase, two features were maintained constant, whereas the tested feature was randomly modulated with fixed increments. A minimum of 10 gait successive cycles were recorded for each experimental condition.

The second series of experiments aimed to evaluate the robustness of the developed control policies. Two testing paradigms were designed to challenge real-time control of foot height. During the first paradigm, termed step increment, the reference band was displaced by a fixed increment (0.5 to 2.5 cm) or decrement (0.5 to 1.5 cm), and maintained at this new reference for six consecutive steps. During the second paradigm, termed triangular waveform, the reference band was gradually displaced by a fixed increment (0.5 to 1.5 cm) or decrement (0.5 to 2.5 cm) at each step until the maximum (7.5 cm) or minimum (3.5 cm) limit of the locomotor system was met. When reaching the limit, the direction of the reference band displacement was inverted (fig. S5).

Locomotor exhaustion

Kinematic and EMG activities were recorded during continuous stepping on a treadmill until exhaustion of locomotor movements. For each rat, recordings stopped when the animal was not able to move the limb forward; both hindlimbs were dragging along the treadmill belt. On the first day, stepping was enabled by serotonin agonists and continuous EES applied overlying L2 and S1 spinal segments at a fixed frequency of 40 Hz. On the second day, the controller was set to modulate EES frequency to maintain step height within a reference band fixed at 4.5 cm. These experiments took place at 7 weeks post-SCI, when substantial exhaustion of locomotor activity occurs clearly (22). The duration of stepping within the reference band, and until exhaustion of locomotion, was measured for each rat and condition.

Staircase paradigm

Rats were positioned in a robotic support system (40) that provided a constant force against the direction of gravity (25% of body weight) while moving the rat forward at a fixed velocity (9 cm/s) along a horizontal runway (Fig. 7). Staircases of various heights (1.3 to 3.5 cm), lengths (12 to 25 cm), and numbers (one or four stairs) were interposed along the runway. For each rat, 100 (single) or 20 (successive) trials were performed along each type of staircase paradigms under noncontrolled or controlled conditions. The percentage of trials dur-

ing which the rat tumbled, touched, or passed the entire staircase was evaluated offline using video recordings.

Statistics

All data are reported as means \pm SEM, unless otherwise specified. Repeated-measures ANOVAs were used to evaluate differences between normally distributed data (Kolmogorov-Smirnov test) from the various experimental conditions. The two-tailed Kruskal-Wallis test was used for nonparametric evaluations. Post hoc differences were assessed using the Bonferroni test. The statistical α level $P < 0.05$ was considered significant.

SUPPLEMENTARY MATERIALS

www.sciencetranslationalmedicine.org/cgi/content/full/6/255/255ra133/DC1
Methods

Fig. S1. Completeness of the SCI.

Fig. S2. Modulation of EES frequency tunes multiple aspects of gait patterns.

Fig. S3. Modulation of EES frequency tunes mono- and polysynaptic responses in flexor and extensor muscle during locomotion.

Fig. S4. Real-time monitoring and control platform.

Fig. S5. High-fidelity control of complex foot trajectory.

Fig. S6. Execution along staircases of various heights and lengths.

Table S1. List of computed kinematic, kinetic, and EMG parameters.

Movie S1. Real-time monitoring and control platform.

Movie S2. Closed-loop neuromodulation achieves high-fidelity control of leg movements.

Movie S3. Closed-loop neuromodulation prevents rapid fatigue during continuous locomotion.

Movie S4. Closed-loop neuromodulation enables locomotion across staircases.

REFERENCES AND NOTES

1. A. M. Lozano, N. Lipsman, Probing and regulating dysfunctional circuits using deep brain stimulation. *Neuron* **77**, 406–424 (2013).
2. D. Borton, S. Micera, R. Millán Jdel, G. Courtine, Personalized neuroprosthetics. *Sci. Transl. Med.* **5**, 210rv212 (2013).
3. P. Krack, A. Batir, N. Van Blercom, S. Chabardes, V. Fraix, C. Arduin, A. Koudsie, P. D. Limousin, A. Benazzouz, J. F. LeBas, A. L. Benabid, P. Pollak, Five-year follow-up of bilateral stimulation of the subthalamic nucleus in advanced Parkinson's disease. *N. Engl. J. Med.* **349**, 1925–1934 (2003).
4. B. Rosin, M. Slovik, R. Mitelman, M. Rivlin-Etzion, S. N. Haber, Z. Israel, E. Vaadia, H. Bergman, Closed-loop deep brain stimulation is superior in ameliorating parkinsonism. *Neuron* **72**, 370–384 (2011).
5. P. A. Tass, L. Qin, C. Hauptmann, S. Dovero, E. Bezard, T. Boraud, W. G. Meissner, Coordinated reset has sustained aftereffects in Parkinsonian monkeys. *Ann. Neurol.* **72**, 816–820 (2012).
6. D. T. Brocker, B. D. Swan, D. A. Turner, R. E. Gross, S. B. Tatter, M. M. Koop, H. Bronte-Stewart, W. M. Grill, Improved efficacy of temporally non-regular deep brain stimulation in Parkinson's disease. *Exp. Neurol.* **239**, 60–67 (2013).
7. R. van den Brand, J. Heutschi, Q. Barraud, J. DiGiovanna, K. Bartholdi, M. Huerlimann, L. Friedli, I. Vollenweider, E. M. Morand, S. Duis, N. Dominici, S. Micera, P. Musienko, G. Courtine, Restoring voluntary control of locomotion after paralyzing spinal cord injury. *Science* **336**, 1182–1185 (2012).
8. S. Harkema, Y. Gerasimenko, J. Hodes, J. Burdick, C. Angeli, Y. Chen, C. Ferreira, A. Willhite, E. Rejc, R. G. Grossman, V. R. Edgerton, Effect of epidural stimulation of the lumbosacral spinal cord on voluntary movement, standing, and assisted stepping after motor complete paraplegia: A case study. *Lancet* **377**, 1938–1947 (2011).
9. B. J. Holinski, D. G. Everaert, V. K. Mushahwar, R. B. Stein, Real-time control of walking using recordings from dorsal root ganglia. *J. Neural Eng.* **10**, 056008 (2013).
10. R. Fuentes, P. Petersson, W. B. Siesser, M. G. Caron, M. A. Nicoletti, Spinal cord stimulation restores locomotion in animal models of Parkinson's disease. *Science* **323**, 1578–1582 (2009).
11. G. Fénelon, C. Goujon, J. M. Gurruchaga, P. Cesaro, B. Jarraya, S. Palfi, J. P. Lefaucheur, Spinal cord stimulation for chronic pain improved motor function in a patient with Parkinson's disease. *Parkinsonism Relat. Disord.* **18**, 213–214 (2012).

12. J. T. Paz, T. J. Davidson, E. S. Frechette, B. Delord, I. Parada, K. Peng, K. Deisseroth, J. R. Huguenard, Closed-loop optogenetic control of thalamus as a tool for interrupting seizures after cortical injury. *Nat. Neurosci.* **16**, 64–70 (2013).
13. K. Minassian, B. Jilge, F. Rattay, M. M. Pinter, H. Binder, F. Gerstenbrand, M. R. Dimitrijevic, Stepping-like movements in humans with complete spinal cord injury induced by epidural stimulation of the lumbar cord: Electromyographic study of compound muscle action potentials. *Spinal Cord* **42**, 401–416 (2004).
14. G. Courtine, Y. Gerasimenko, R. van den Brand, A. Yew, P. Musienko, H. Zhong, B. Song, Y. Ao, R. M. Ichiyama, I. Lavrov, R. R. Roy, M. V. Sofroniew, V. R. Edgerton, Transformation of non-functional spinal circuits into functional states after the loss of brain input. *Nat. Neurosci.* **12**, 1333–1342 (2009).
15. V. F. Lyalka, L. J. Hsu, A. Karayannidou, P. V. Zelenin, G. N. Orlovsky, T. G. Deliagina, Facilitation of postural limb reflexes in spinal rabbits by serotonergic agonist administration, epidural electrical stimulation, and postural training. *J. Neurophysiol.* **106**, 1341–1354 (2011).
16. P. Afshar, A. Khambhati, S. Stanslaski, D. Carlson, R. Jensen, D. Linde, S. Dani, M. Lazarewicz, P. Cong, J. Giftakis, P. Stypulkowski, T. Denison, A translational platform for prototyping closed-loop neuromodulation systems. *Front. Neural Circuits* **6**, 117 (2013).
17. M. Capogrosso, N. Wenger, S. Raspopovic, P. Musienko, J. Beauparlant, L. Bassi Luciani, G. Courtine, S. Micera, A computational model for epidural electrical stimulation of spinal sensorimotor circuits. *J. Neurosci.* **33**, 19326–19340 (2013).
18. P. Gad, I. Lavrov, P. Shah, H. Zhong, R. R. Roy, V. R. Edgerton, Y. Gerasimenko, Neuromodulation of motor-evoked potentials during stepping in spinal rats. *J. Neurophysiol.* **110**, 1311–1322 (2013).
19. I. Lavrov, C. J. Dy, A. J. Fong, Y. Gerasimenko, G. Courtine, H. Zhong, R. R. Roy, V. R. Edgerton, Epidural stimulation induced modulation of spinal locomotor networks in adult spinal rats. *J. Neurosci.* **28**, 6022–6029 (2008).
20. J. Ladenbauer, K. Minassian, U. S. Hofstoetter, M. R. Dimitrijevic, F. Rattay, Stimulation of the human lumbar spinal cord with implanted and surface electrodes: A computer simulation study. *IEEE Trans. Neural Syst. Rehabil. Eng.* **18**, 637–645 (2010).
21. V. Dietz, R. Müller, Degradation of neuronal function following a spinal cord injury: Mechanisms and countermeasures. *Brain* **127**, 2221–2231 (2004).
22. J. Beauparlant, R. van den Brand, Q. Barraud, L. Friedli, P. Musienko, V. Dietz, G. Courtine, Undirected compensatory plasticity contributes to neuronal dysfunction after severe spinal cord injury. *Brain* **136**, 3347–3361 (2013).
23. C. A. Angeli, V. R. Edgerton, Y. P. Gerasimenko, S. J. Harkema, Altering spinal cord excitability enables voluntary movements after chronic complete paralysis in humans. *Brain* **137**, 1394–1409 (2014).
24. H. Vallery, P. Lutz, J. von Zitzewitz, G. Rauter, M. Fritschi, C. Everarts, R. Ronsse, A. Curt, M. Bolliger, S. B. Pai, *Multidirectional transparent support for overground gait training*, IEEE International Conference on Rehabilitation Robotics (ICORR), Seattle, WA, 24 to 26 June 2013.
25. D. A. McCreary, Spinal circuitry of sensorimotor control of locomotion. *J. Physiol.* **533**, 41–50 (2001).
26. Y. Gerasimenko, R. Gorodnichev, E. Machueva, E. Pivovarova, D. Semyenov, A. Savochin, R. R. Roy, V. R. Edgerton, Novel and direct access to the human locomotor spinal circuitry. *J. Neurosci.* **30**, 3700–3708 (2010).
27. G. Courtine, S. J. Harkema, C. J. Dy, Y. P. Gerasimenko, P. Dyhre-Poulsen, Modulation of multisegmental monosynaptic responses in a variety of leg muscles during walking and running in humans. *J. Physiol.* **582**, 1125–1139 (2007).
28. J. B. Zimmermann, K. Seki, A. Jackson, Reanimating the arm and hand with intraspinal microstimulation. *J. Neural Eng.* **8**, 054001 (2011).
29. D. Kernell, Principles of force gradation in skeletal muscles. *Neural Plast.* **10**, 69–76 (2003).
30. K. Minassian, I. Persy, F. Rattay, M. M. Pinter, H. Kern, M. R. Dimitrijevic, Human lumbar cord circuitries can be activated by extrinsic tonic input to generate locomotor-like activity. *Hum. Mov. Sci.* **26**, 275–295 (2007).
31. Y. Gerasimenko, R. R. Roy, V. R. Edgerton, Epidural stimulation: Comparison of the spinal circuits that generate and control locomotion in rats, cats and humans. *Exp. Neurol.* **209**, 417–425 (2008).
32. G. P. Braz, M. Russold, G. M. Davis, Functional electrical stimulation control of standing and stepping after spinal cord injury: A review of technical characteristics. *Neuromodulation* **12**, 180–190 (2009).
33. C. L. Lynch, M. R. Popovic, Functional electrical stimulation. *IEEE Contr. Syst. Mag.* **28**, 40–50 (2008).
34. E. C. Field-Fote, Combined use of body weight support, functional electric stimulation, and treadmill training to improve walking ability in individuals with chronic incomplete spinal cord injury. *Arch. Phys. Med. Rehabil.* **82**, 818–824 (2001).
35. G. Bosco, R. E. Poppele, Proprioception from a spinocerebellar perspective. *Physiol. Rev.* **81**, 539–568 (2001).
36. G. Courtine, R. R. Roy, J. Hodgson, H. McKay, J. Raven, H. Zhong, H. Yang, M. H. Tuszynski, V. R. Edgerton, Kinematic and EMG determinants in quadrupedal locomotion of a non-human primate (Rhesus). *J. Neurophysiol.* **93**, 3127–3145 (2005).
37. Y. P. Ivanenko, A. d'Avella, R. E. Poppele, F. Lacquaniti, On the origin of planar covariation of elevation angles during human locomotion. *J. Neurophysiol.* **99**, 1890–1898 (2008).
38. D. Borton, M. Bonizzato, J. Beauparlant, J. DiGiovanna, E. M. Moraud, N. Wenger, P. Musienko, I. R. Minev, S. P. Lacour, R. Millán Jdel, S. Micera, G. Courtine, Corticospinal neuroprostheses to restore locomotion after spinal cord injury. *Neurosci. Res.* **78**, 21–29 (2014).
39. B. Mariani, S. Rochat, C. J. Büla, K. Aminian, Heel and toe clearance estimation for gait analysis using wireless inertial sensors. *IEEE Trans. Biomed. Eng.* **59**, 3162–3168 (2012).
40. N. Dominici, U. Keller, H. Vallery, L. Friedli, R. van den Brand, M. L. Starkey, P. Musienko, R. Riener, G. Courtine, Versatile robotic interface to evaluate, enable and train locomotion and balance after neuromotor disorders. *Nat. Med.* **18**, 1142–1147 (2012).
41. V. R. Edgerton, G. Courtine, Y. P. Gerasimenko, I. Lavrov, R. M. Ichiyama, A. J. Fong, L. L. Cai, C. K. Otoshi, N. J. K. Tillakaratne, J. W. Burdick, R. R. Roy, Training locomotor networks. *Brain Res. Rev.* **57**, 241–254 (2008).
42. P. Musienko, R. van den Brand, O. Märzendorfer, R. R. Roy, Y. Gerasimenko, V. R. Edgerton, G. Courtine, Controlling specific locomotor behaviors through multidimensional monoaminergic modulation of spinal circuitries. *J. Neurosci.* **31**, 9264–9278 (2011).
43. I. Steuer, P. Rouleau, P. A. Guertin, Pharmacological approaches to chronic spinal cord injury. *Curr. Pharm. Des.* **19**, 4423–4436 (2013).
44. C. Ethier, E. R. Oby, M. J. Bauman, L. E. Miller, Restoration of grasp following paralysis through brain-controlled stimulation of muscles. *Nature* **485**, 368–371 (2012).

Acknowledgments: We thank D. Borton for helpful advice on the manuscript, S. Duis and K. Bartholdi for help with animal care, A. Vuaridel for data processing, and J. Gandar and A. Kuck for their contribution to real-time platform development. **Funding:** A Starting Grant from the European Research Council (ERC 261247, Walk Again), the European Community's Seventh Framework Program (CP-IP 258654, NeuWALK), the International Paraplegic Foundation, the Bertarelli Foundation, and funding from the National Center of Competence in Research (NCCR) in Robotics and NanoTera.ch program of the Swiss National Science Foundation (SpineRepair). **Author contributions:** N.W., E.M.M., S.R., and M.B. performed the in vivo experiments. N.W., E.M.M., and G.C. analyzed the data. N.W. and E.M.M. conducted the statistical analysis. P.M. implanted the epidural electrodes and placed the SCI, whereas N.W. and G.C. inserted the EMG electrodes. N.W., E.M.M., J.D., M.M., S.M., and G.C. conceived the experiments. N.W., E.M.M., and G.C. prepared the figures with the help of the other authors. N.W., E.M.M., and G.C. wrote the manuscript, and all the authors contributed to its editing. G.C. supervised all aspects of the work. **Competing interests:** Ongoing European patent application (no. 13191003.6) on the stimulation algorithms. The authors declare no other competing interests. **Data and materials availability:** Raw data and custom-developed C++ and TDT (Tucker-Davis Technologies) codes will be made available through material transfer agreement upon request to G.C.

Submitted 18 December 2013

Accepted 5 May 2014

Published 24 September 2014

10.1126/scitranslmed.3008325

Citation: N. Wenger, E. M. Moraud, S. Raspopovic, M. Bonizzato, J. DiGiovanna, P. Musienko, M. Morari, S. Micera, G. Courtine, Closed-loop neuromodulation of spinal sensorimotor circuits controls refined locomotion after complete spinal cord injury. *Sci. Transl. Med.* **6**, 255ra133 (2014).

Supplementary Materials for

Closed-loop neuromodulation of spinal sensorimotor circuits controls refined locomotion after complete spinal cord injury

Nikolaus Wenger, Eduardo Martin Moraud, Stanisa Raspopovic, Marco Bonizzato, Jack DiGiovanna, Pavel Musienko, Manfred Morari, Silvestro Micera, Grégoire Courtine*

*Corresponding author. E-mail: gregoire.courtine@epfl.ch

Published 24 September 2014, *Sci. Transl. Med.* **6**, 255ra133 (2014)
DOI: 10.1126/scitranslmed.3008325

This PDF file includes:

Methods

Fig. S1. Completeness of the SCI.

Fig. S2. Modulation of EES frequency tunes multiple aspects of gait patterns.

Fig. S3. Modulation of EES frequency tunes mono- and polysynaptic responses in flexor and extensor muscle during locomotion.

Fig. S4. Real-time monitoring and control platform.

Fig. S5. High-fidelity control of complex foot trajectory.

Fig. S6. Execution along staircases of various heights and lengths.

Table S1. List of computed kinematic, kinetic, and EMG parameters.

Legends for movies S1 to S4

Other Supplementary Material for this manuscript includes the following:

(available at

www.sciencetranslationalmedicine.org/cgi/content/full/6/255/255ra133/DC1)

Movie S1 (.avi format). Real-time monitoring and control platform.

Movie S2 (.avi format). Closed-loop neuromodulation achieves high-fidelity control of leg movements.

Movie S3 (.avi format). Closed-loop neuromodulation prevents rapid fatigue during continuous locomotion.

Movie S4 (.avi format). Closed-loop neuromodulation enables locomotion across staircases.

SUPPLEMENTARY METHODS

Surgical procedure and post-surgical care

Surgical interventions were performed under general anesthesia and aseptic conditions. All 8 animals examined in this study exhibited a complete transection of the mid-thoracic spinal cord (~ spinal segment T7). The completeness of the spinal cord transections was verified during surgery by two independent surgeons by lifting the cut ends of the cord (14). Gel foam was inserted into the gap created by the transection as a coagulant and to separate the cut ends of the spinal cord. The transections led to permanent and complete paralysis of the hindlimbs in all the tested rats ($n=8$) (Fig. 1C). The spinal cord tissue was kept postmortem for histological evaluations in order to verify lesion completeness (fig. S1). The tissue was stained against glial fibrillary acidic protein (GFAP) and no remaining neural tissue was observed at the site of the lesion.

Stimulating electrodes were created by removing a small part (1 mm notch) of insulation from Teflon-coated stainless steel wires (AS632, Cooner Wire). These were subsequently secured during surgery at the midline overlying spinal level L2 and S1 by suturing the wires to the dura. A common ground wire (1 cm of Teflon removed at the distal end) was inserted subcutaneously over the right shoulder. Bipolar intramuscular EMG electrodes (AS632; Cooner Wire) were implanted using the same wire type, into the tibialis anterior and medial gastrocnemius muscles, bilaterally. All electrode wires were connected to a percutaneous amphenol connector (Omnetics Connector Corporation) cemented to the skull of the rat. The rats then received a complete transection of the spinal cord (~T7). The proper location of the epidural and EMG electrodes was verified post-mortem, along with the extent and location of the lesion.

Kinematic, ground reaction force, and electromyographic recordings

Bilateral hindlimb kinematics were recorded using 12 infrared motion capture cameras (200 Hz; Vicon). Reflective markers were attached bilaterally overlying iliac crest, greater trochanter (hip), lateral condyle (knee), lateral malleolus (ankle) and the distal end of the fifth metatarsal (limb endpoint) (Fig. 1A). Nexus (Vicon) was used to obtain 3D coordinates of the markers. The body was modeled as an interconnected chain of rigid segments, and joint angles were generated accordingly. EMG signals (12.207 kHz) were amplified, filtered (10–5,000-Hz bandpass) and recorded synchronized to kinematic and ground reaction force data. Vertical ground reaction forces were measured using a biomechanical force plate (2 kHz; HE6X6, AMTI) located below the treadmill belt, or along the runway. Video recordings (200

Hz) were obtained using two cameras (Basler Vision Technologies) oriented at 90° and 270° with respect to the direction of locomotion.

A minimum of 10 step cycles was extracted for each experimental condition and rat. A total of 147 parameters quantifying gait, kinematics, ground reaction force, and EMG features were computed for each limb and gait cycle according to methods described in detail previously (14, 39, 42, 43). These parameters provide a comprehensive quantification of gait patterns ranging from general features of locomotion to fine details of limb motion. The entire list of 147 computed parameters is described in table S1.

Reflex analysis

EES-evoked motor potentials were recorded in TA and MG muscles. Each pulse of stimulation elicits a medium-latency and late-latency response, which were determined based on their respective latency (17), as illustrated in Fig. 4A. The peak amplitude of each response was measured through custom-made software in Matlab. Spectral analysis of EMG activity by fast Fourier transformation (FFT) was performed on the identified bursts of EMG activity recorded from the TA and MG muscles. Spectral peaks in frequency ranges from 0 to 160 Hz were calculated. Burst amplitude was calculated as the mean of the rectified EMG signal during stance and swing phase for MG and TA muscle, respectively. The area under the curve of the rectified EMG signal was calculated separately for the monosynaptic and polysynaptic responses. Both responses were aligned separately along the normalized gait cycle and their response activity calculated using a moving average with a 150 ms window size. Results are reported in percentage of the maximum value across all tested frequencies.

Principal component analysis

The various experimental conditions led to substantial modulation of gait patterns, which were evident in the modifications of a large proportion of the computed parameters. In order to extract the modulated gait characteristics in response to changes in stimulation features, we implemented a multi-step statistical procedure based on principal component (PC) analysis (14, 42). PC analyses were applied on data from all individual gait cycles for all the rats together. Data were analyzed using the correlation method, which adjusts the mean of the data to zero and the standard deviation to 1. This is a conservative procedure that is appropriate for variables that differ in their variance (e.g. kinematic vs. EMG data).

SUPPLEMENTARY FIGURES

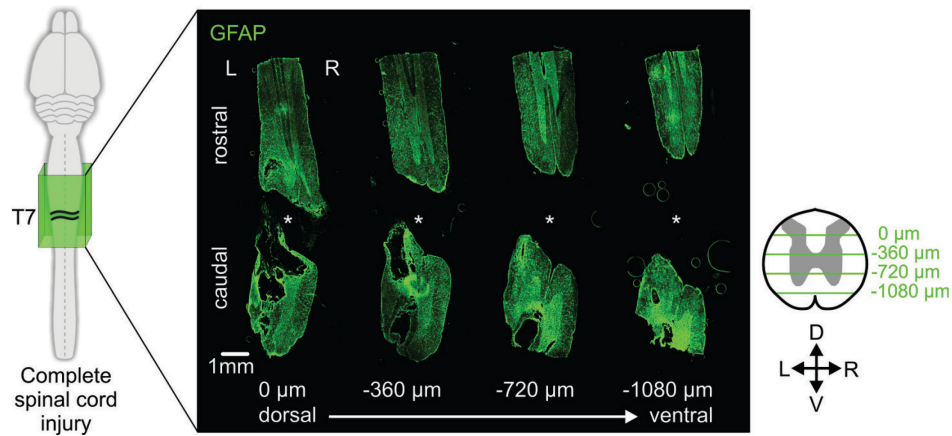


Fig. S1. Completeness of the SCI. Rats received a complete transection of the spinal cord around mid-thoracic segment T7. The completeness and location of the lesion was verified macroscopically during surgery by two independent surgeons, and post-mortem through histological evaluations. The photographs show a series of histological sections stained against glial fibrillary acidic protein (GFAP) in a representative rat. The site of lesion is marked with an asterisk (*). Images were obtained on coronal sections taken at regular intervals (360 μm) from the dorsal to ventral aspects of the spinal cord. Histological slice thickness, 30 μm . L, left; R right; D, dorsal; V, ventral.

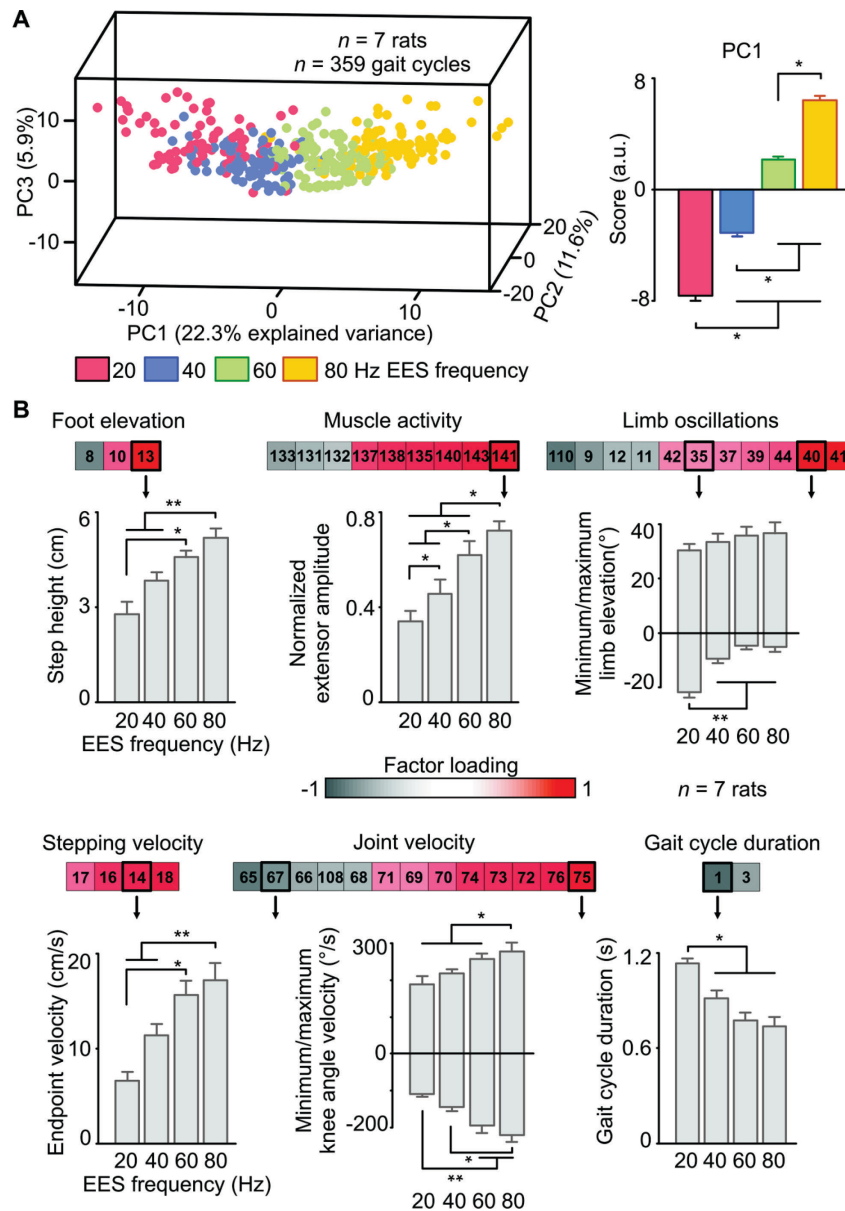


Fig. S2: Modulation of EES frequency tunes multiple aspects of gait patterns. (A) PC analysis applied on all 147 computed parameters (table S1) from all the gait cycles recorded in 7 rats for EES frequencies set at 20, 40, 60, and 80 Hz. Each data point is a gait cycle represented in the 3D space defined by PC1 to PC3. (B) Histogram plots reporting the mean values of scores on PC1 for the various EES frequencies. The variables with high factor loadings on PC1 ($|value| > 0.5$) were grouped into functional clusters. Numbers refer to the computed variables in table S1. The histogram plots report, for each functional cluster, the mean values of a representative variable at the different EES frequencies. The arrows refer to the variable illustrated in the histogram plots. Data are means \pm SEM. * $P < 0.05$, ** $P < 0.01$, Repeated measure ANOVA followed by Newman-Keuls post-hoc tests.

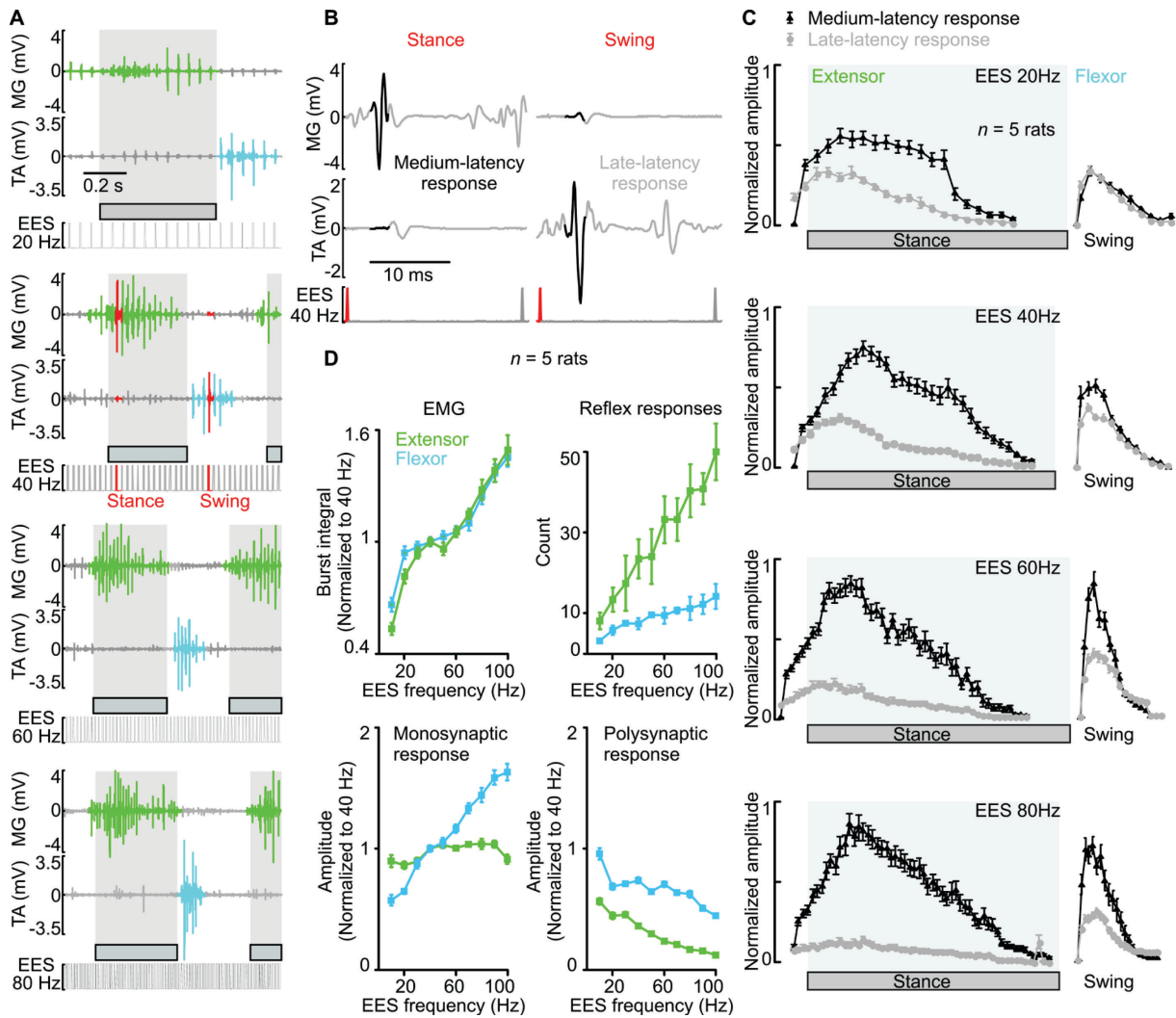


Fig. S3: Modulation of EES frequency tunes mono- and polysynaptic responses in flexor and extensor muscle during locomotion. (A) EMG activity recorded in extensor (MG) and flexor (TA) muscles during a representative gait cycle under EES frequencies set at 20, 40, 60, and 80 Hz. The bursts of EMG activity extracted for further analysis are represented in green and blue for extensor and flexor muscles, respectively. (B) Color-coded medium-latency and late-latency reflex responses elicited in extensor and flexor muscles in response to a pulse of EES during stance and swing. Responses are identified based on their respective latencies. The example is extracted from panel (A) during EES at 40 Hz. (C) Mean amplitude (\pm SEM) of each EES-induced monosynaptic (black) and polysynaptic (grey) response over the course of the stance phase for extensor muscles and swing for flexor muscles. EMG bursts were built from a succession of modulated monosynaptic and polysynaptic responses. Ten EMG bursts were analyzed per muscle, condition, and rat ($n = 5$). The amplitude of responses was normalized to the maximum amplitude recorded for each rat over all the experimental conditions. (D) Mean values (\pm SEM) of EMG burst integrals, of the total number of induced motor responses per burst, and of the averaged amplitude of monosynaptic and polysynaptic responses over the entire bursts in extensor and flexor muscles for the different EES frequencies. Data are for $n = 5$ rats.

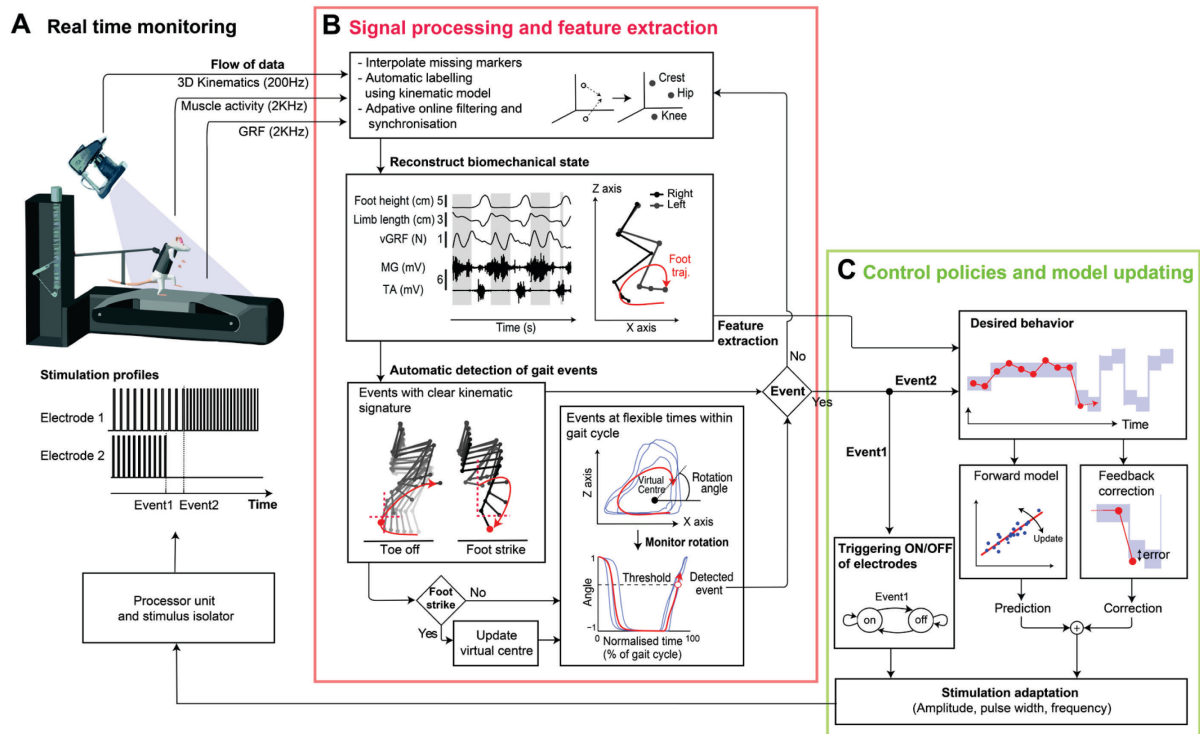


Fig. S4: Real-time monitoring and control platform. (A) The flow of kinematics, EMG, and kinetic information was continuously monitored in real-time through the integrated system Vicon. (B) All the signals were filtered online using adaptive filters (least mean squares). To deal with missing kinematic information owing to occlusion of markers, the coordinates of each marker were interpolated by triangulation. The different sources of information were synchronized to reconstruct the complete biomechanical state of the locomotor system. The signal-processing system then combined two complementary algorithms to automatically detect key gait events and extract meaningful features integrated into control policies. First, gait events with clear-cut kinematic signatures (foot strike and toe off,) were detected online based on a threshold of foot elevation in the sagittal plane. Second, custom-made algorithms monitored the circular trajectory of the foot around a virtual center updated after each cycle. The rotation angle of the foot trajectory along this circular path allowed to trigger stimulation or updated features of stimulation at any time of the gait cycle. (C) Both sets of events triggered controller calculations, which derived the appropriate corrections of EES parameters. The combination of feedback and feed-forward information generated corrections of EES frequency in order to achieve a desired locomotor output. Forward models were automatically updated after each gait cycle to account for putative time-varying characteristics of the system. Each electrode may also be turned on and off at specific times within the gait cycle to reinforce specific aspects of locomotion.

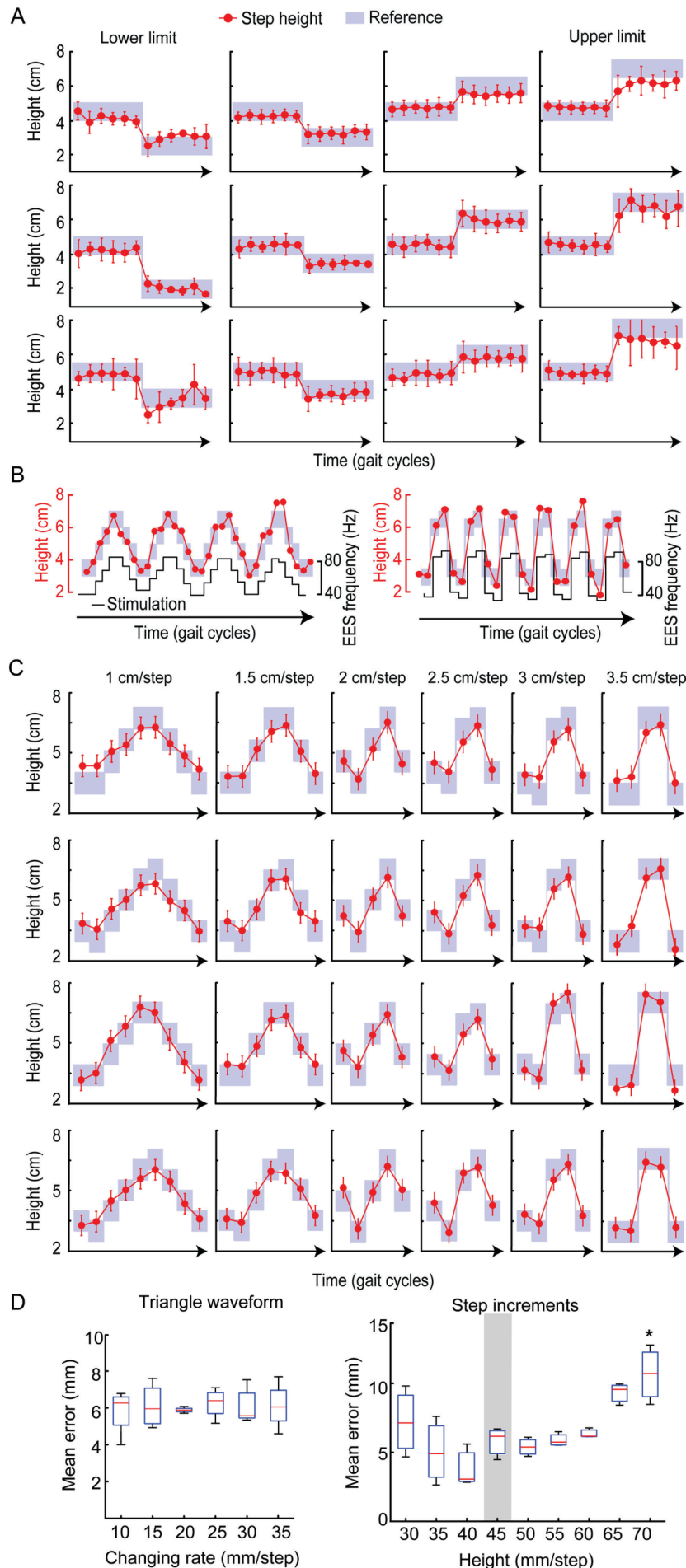


Fig. S5: High-fidelity control of complex foot trajectory.

(A) Step-increments. Data are mean step heights (\pm SD) during stepping with constant-shift of the reference band upward or downward with small and large increments/decrements until reaching steady-state (6 consecutive steps). Each horizontal panel corresponds to a distinct rat ($n = 3$). (B) Representative trials showing the step height performance during a tracking task of a periodic triangular waveform (piecewise linear increments or decrements at different rates) during stepping on a treadmill. (C) Triangle waveforms. Mean values of step heights (\pm SD) during the same type of executions shown in (B), but for the entire range of tested increment/decrement values, from left to right. Each horizontal panel corresponds to a distinct rat ($n = 4$ rats shown). (D) Boxplots reporting the median value, SD, and 95% confidence intervals for step height errors for each experimental condition. * $P < 0.05$ for the marked condition versus all the other conditions (Kruskal-Wallis test).

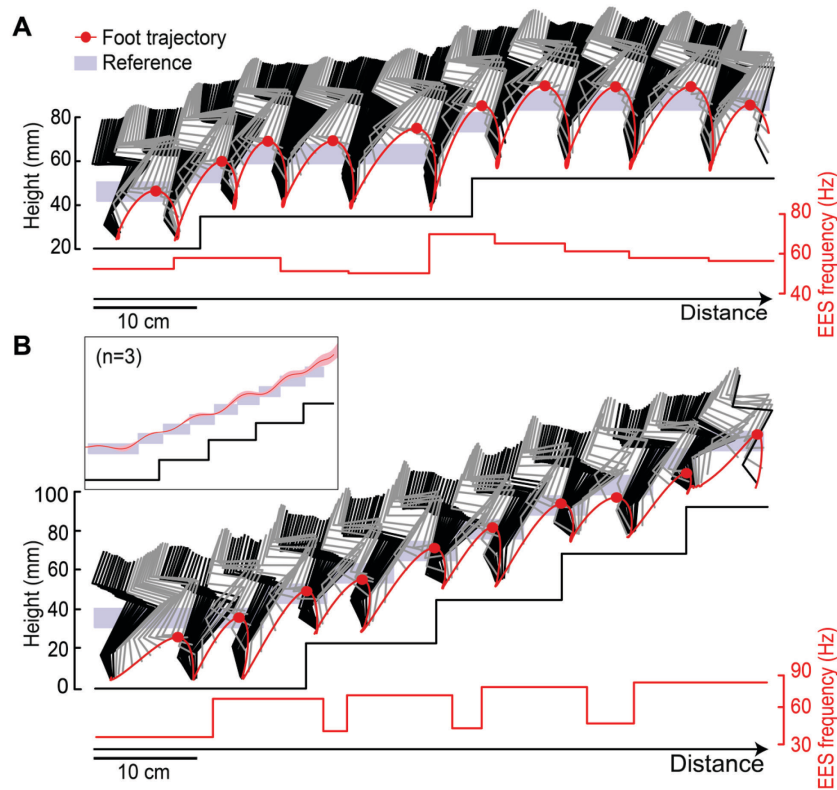


Fig. S6: Execution along staircases of various heights and lengths. (A) Representative stick diagram decomposition of hindlimb movement and limb endpoint trajectory during stance (black) and swing (grey) while walking along a succession of two staircases (1.7-cm height, 25-cm length) under controlled condition. The red dots indicate the maximum elevation of the foot during swing, defined as step height. The positions of the reference band and changes in EES frequency are represented by the shaded area and red signal, respectively. (B) Same representation as in (A) for an execution along a succession of 4 staircases (2-cm height, 12-cm length). The inset displays the mean foot trajectories (\pm SD) averaged over 20 successive repetitions for 3 rats.

SUPPLEMENTARY TABLE

Table S1: List of computed kinematic, kinetic, and EMG parameters.

Parameters	Parameter number	Detailed explanation
Kinematics		
Temporal features		
	1	Cycle duration
	2	Cycle velocity
	3	Stance duration
	4	Swing duration
	5	Relative stance duration (percent of the cycle duration)
Limb endpoint (Metatarsal phalange) trajectory		
	6	Interlimb temporal coupling
	7	Duration of double stance phase
	8	Stride length
	9	Step length
	10	3D limb endpoint path length
	11	Maximum backward position
	12	Minimum forward position
	13	Step height
	14	Maximum speed during swing
	15	Relative timing of maximum velocity during swing
	16	Acceleration at swing onset
	17	Average endpoint velocity
	18	Orientation of the velocity vector at swing onset
	19	Dragging
	20	Relative dragging duration (percent of swing duration)
Stability		
<i>Base of support</i>	21	Positioning of the foot at stance onset with respect to the pelvis
	22	Stance width
Trunk and pelvic position and oscillations	23	Maximum hip sagittal position
	24	Minimum hip sagittal position
	25	Amplitude of sagittal hip oscillations
	26	Variability of sagittal crest position
	27	Variability of sagittal crest velocity
	28	Variability of vertical hip movement
	29	Variability of sagittal hip movement
	30	Variability of the 3D hip oscillations
	31	Length of pelvis displacements in the forward direction
	32	Length of pelvis displacements in the medio-lateral direction
	33	Length of pelvis displacements in the vertical direction
	34	Length of pelvis displacements in all directions
Joint angles and segmental oscillations		
<i>Backward</i>	35	Crest oscillations
	36	Thigh oscillations
	37	Leg oscillations
	38	Foot oscillations
	39	Whole limb oscillations
<i>Forward</i>	40	Crest oscillations
	41	Thigh oscillations
	42	Leg oscillations
	43	Foot oscillations
	44	Whole limb oscillations
<i>Flexion</i>	45	Hip joint angle
	46	Knee joint angle
	47	Ankle joint angle
<i>Abduction</i>	48	Whole limb abduction
	49	Foot abduction
<i>Extension</i>	50	Hip joint angle

	51	Knee joint angle
	52	Ankle joint angle
<i>Adduction</i>	53	Whole limb adduction
	54	Foot adduction
<i>Amplitude</i>	55	Crest oscillations
	56	Thigh oscillations
	57	Leg oscillations
	58	Foot oscillations
	59	Whole limb oscillations
	60	Hip joint angle
	61	Knee joint angle
	62	Ankle joint angle
	63	Whole limb medio-lateral oscillations
	64	Foot abduction/adduction
Velocity		
<i>Minimum</i>	65	Whole limb oscillation velocity
	66	Hip joint angle velocity
	67	Knee joint angle velocity
	68	Ankle joint angle velocity
<i>Maximum</i>	69	Whole limb oscillation velocity
	70	Hip joint angle velocity
	71	Knee joint angle velocity
	72	Ankle joint angle velocity
<i>Amplitude</i>	73	Whole limb angle velocity
	74	Hip joint angle velocity
	75	Knee joint angle velocity
	76	Ankle joint angle velocity
Inter-limb coordination		
<i>PC analysis</i>	77	Degree of linear coupling between joint oscillations
<i>FFT</i>	78	Temporal coupling between crest and thigh oscillations
<i>decomposition</i>	79	Temporal coupling between thigh and leg oscillations
	80	Temporal coupling between leg and foot oscillations
	81	Correlation between crest and thigh oscillations
	82	Correlation between thigh and leg oscillations
	83	Correlation between leg and foot oscillations
<i>Crosscorrelation</i>	84	Correlation between hip and knee oscillations
	85	Correlation between knee and ankle oscillations
	86	Correlation between ankle and MTP oscillations
	87	Temporal lag between backward positions of crest and thigh oscillations
	88	Temporal lag between forward positions of crest and thigh oscillations
<i>Relative coupling</i>	89	Temporal lag between backward positions of thigh and leg oscillations
	90	Temporal lag between forward positions of the thigh and leg oscillations
	91	Temporal lag between backward positions of leg and foot oscillations
	92	Temporal lag between forward positions of leg and foot oscillations
<i>Inter-segmental coordination compared to</i>	93	Lag of the cross correlation function between hindlimb oscillations
	94	Maximum R-value of the cross correlation function between hindlimb oscillations
	95	Lag of the cross correlation function between hip oscillations
	96	Maximum R-value of the cross correlation function between hip oscillations
<i>Able-bodied rats</i>	97	Lag of the cross correlation function between knee oscillations
	98	Maximum R-value of the cross correlation function between knee oscillations

	99	Lag of the cross correlation function between ankle oscillations
	100	Maximum R-value of the cross correlation function between ankle oscillations
	101	Lag of the cross correlation function between endpoint oscillations
	102	Maximum R-value of the cross correlation function between endpoint oscillations
	103	Phase of the first harmonic of the FFT of the hip elevation angle
	104	Amplitude of the first harmonic of the FFT of the hip elevation angle
	105	Phase of the first harmonic of the FFT of the knee elevation angle
	106	Amplitude of the first harmonic of the FFT of the knee elevation angle
	107	Phase of the first harmonic of the FFT of the ankle elevation angle
	108	Amplitude of the first harmonic of the FFT of the ankle elevation angle
Left-right	109	Phase of the first harmonic of the FFT of the endpoint elevation angle
hindlimb	110	Amplitude of the first harmonic of the FFT of the endpoint elevation angle
coordination	111	Phase of the first harmonic of the FFT of the hindlimb elevation angle
	112	Amplitude of the first harmonic of the FFT of the hindlimb elevation angle
	113	Lag of the cross correlation function between crest and thigh limb elevation angles
Hindlimb	114	Lag of the cross correlation function between thigh and hindlimb elevation angles
coordination	115	Lag of the cross correlation function between hip and thigh elevation angles
	116	Lag of the cross correlation function between hindlimb and foot elevation angles
	117	Lag of the cross correlation function between thigh and ankle elevation angles
	118	Lag of the cross correlation function between ankle and foot elevation angles

Kinetics

	119	Medio-lateral forces
	120	Anteroposterior forces
	121	Vertical forces
	122	Weight-bearing level

EMG

Timing (relative to cycle duration, paw contact to paw contact)

<i>Extensor ipsilateral</i>	123	Relative onset of ipsilateral MG EMG burst
<i>Flexor ipsilateral</i>	124	Relative end of ipsilateral MG EMG burst
<i>Extensor contralateral</i>	125	Relative onset of ipsilateral TA EMG burst
<i>Flexor contralateral</i>	126	Relative end of ipsilateral TA EMG burst
<i>Extensor ipsilateral</i>	127	Relative onset of contralateral MG EMG burst
<i>Flexor ipsilateral</i>	128	Relative end of contralateral MG EMG burst
<i>Extensor contralateral</i>	129	Relative onset of contralateral TA EMG burst
<i>Flexor contralateral</i>	130	Relative end of contralateral TA EMG burst
Duration		
<i>Extensor ipsilateral</i>	131	Duration of ipsilateral MG EMG burst
<i>Flexor ipsilateral</i>	132	Duration of ipsilateral TA EMG burst
<i>Extensor contralateral</i>	133	Duration of contralateral MG EMG burst

<i>Flexor contralateral</i>	134	Duration of contralateral TA EMG burst
Amplitude		
<i>Extensor ipsilateral</i>	135	Mean amplitude of ipsilateral MG EMG burst
	136	Integral of ipsilateral MG EMG burst
	137	Root mean square of ipsilateral MG EMG burst
<i>Flexor ipsilateral</i>	138	Mean amplitude of ipsilateral TA EMG burst
	139	Integral of ipsilateral TA EMG burst
	140	Root mean square of ipsilateral TA EMG burst
<i>Extensor contralateral</i>	141	Mean amplitude of contralateral MG EMG burst
	142	Integral of contralateral MG EMG burst
	143	Root mean square of contralateral MG EMG burst
<i>Flexor contralateral</i>	144	Mean amplitude of contralateral TA EMG burst
	145	Integral of contralateral TA EMG burst
	146	Root mean square of contralateral TA EMG burst
Muscle coactivation	147	Co-contraction of flexor and extensor muscle

SUPPLEMENTARY VIDEOS

Movie S1: Real-time monitoring and control platform. The platform to monitor whole-body kinematics, muscle activity, and ground reaction forces in real-time involves an integrated system that interfaces the reconstructed biomechanical state of the rat with control algorithms. Spatial and temporal features of gait are extracted *online* to trigger feedback and feed-forward adjustments of stimulation parameters in order to maintain step height within a desired range. .

Movie S2: Closed-loop neuromodulation achieves high-fidelity control of leg movements. The experimental procedure promoted locomotion in paralyzed rats. We imposed small changes and large changes in step height, as well as maintenance of stable references. The controller successfully tuned stimulation frequency in order to automatically adjust step height.

Movie S3: Closed-loop neuromodulation prevents rapid fatigue during continuous locomotion. We compared the evolution of the stepping patterns and muscle activity during non-controlled and controlled neuromodulation of spinal circuits. After 9 minutes, rats demonstrated a graded decrease in step height because of fatigue, which was corrected under controlled stimulation conditions.

Movie S4: Closed-loop neuromodulation enables locomotion across staircases. Closed-loop neuromodulation allowed the rats to adjust limb kinematic and ground reaction forces in order to restore locomotion across single and combinations of staircases in paralyzed rats. Automated tuning of EES frequency produced adequate foot trajectory to overcome the staircase. By contrast, non-controlled rats were unable to climb the staircase.

Nature Methods

Translational neuroprosthetic toolbox for modulation of spinal circuits in space and time

Nikolaus Wenger^{1,*}, Eduardo Martin Moraud^{2,*}, Pavel Musienko^{1,3,*}, Jerome Gandar^{1,&}, Marco Capogrosso^{3,&}, David Borton^{1,&}, Quentin Barraud¹, Nadia Dominici¹, Ivan R. Minev⁴, Arthur Hirsch⁴, Natasha Pavlova¹, Alexandre Larmagnac⁵, Leonie Asboth¹, Laetitia Baud¹, Simone Duis¹, Julie Kreider¹, Andrea Mortera², Qin Li⁸, Jack DiGiovanna², Rubia van den Brand¹, Janos Vörös⁵, Jocelyne Bloch⁷, Peter Detemple⁶, Stéphanie P. Lacour⁴, Erwan Bézard⁸, Silvestro Micera^{2,9}, and Grégoire Courtine^{1,7, CA}

*,& equal contribution

AUTHOR AFFILIATION

1. Center for Neuroprosthetics and Brain Mind Institute, School of Life Sciences, Swiss Federal Institute of Technology (EPFL), Lausanne, Switzerland.
2. Motor Physiology Laboratory, Pavlov Institute of Physiology, St. Petersburg, Russia.
3. Translational Neural Engineering Lab, Center for Neuroprosthetics and Institute of Bioengineering, School of Bioengineering, EPFL, Lausanne, Switzerland
4. Center for Neuroprosthetics and Institute of Bioengineering, EPFL, Lausanne, Switzerland.
5. Swiss Federal Institute of Technology (ETH), Zurich, Switzerland.
6. IMM, Mainz, Germany
7. Centre Hospitalier Universitaire Vaudois (CHUV), Lausanne, Switzerland.
8. Motac Neuroscience, Beijing, China.
9. The BioRobotics Institute, Scuola Superiore Sant' Anna, Pisa, Italy

CONTACT

METHODOLOGIES FOR SPINAL CIRCUIT NEUROMODULATION

Grégoire Courtine, PhD

Professor, International Paraplegic Foundation Chair in Spinal Cord Repair

Center for Neuroprosthetics and Brain Mind Institute

SWISS FEDERAL INSTITUTE OF TECHNOLOGY (EPFL)

CH-1015 Lausanne

gregoire.courtine@epfl.ch

RUNNING TITLE

METHODOLOGIES FOR SPINAL CIRCUIT NEUROMODULATION

ABSTRACT

Continuous neuromodulation of the spinal cord improves motor control after various neurological disorders. However, technical and conceptual limitations have restricted the development of more effective stimulation protocols. Here, we introduce a mechanistic framework that steered hardware and software development to achieve electrical neuromodulation of spinal circuits in freely behaving mice, rats, and monkeys. We introduce spatial selectivity and temporal structure in neuromodulation therapies that are adjusted based on continuous movement feedback. These algorithms resolved limb-specific impairments and alleviated locomotor deficits in multiple rodent or primate models of spinal cord injuries and Parkinson's disease. Our results provide comprehensive resources and new methods to manipulate spinal circuits in space and time for basic neuroscience research and translational medicine.

INTRODUCTION

Various neurological disorders disrupt the communication matrix between supraspinal centers and spinal circuits, which leads to a range of motor disabilities. Neuromodulation strategies provide access to surviving circuits and pathways to alleviate these deficits^{1, 2}. In particular, electrical spinal cord neuromodulation have mediated striking improvement of motor functions in animal models and patients with spinal cord injury^{3, 4} and Parkinson's disease⁵⁻⁷.

Movement production requires the activation of spatially distributed motor circuits following precise temporal sequences that are continuously adjusted through sensory feedback⁸. However, current neuromodulation therapies deliver stimulation to restricted spinal cord locations, and remain constant throughout motor execution³⁻⁷. Here, we hypothesized that neuromodulation therapies integrating spatial selectivity and temporal structure matching natural circuit dynamics will mediate superior facilitation of movement after neuromotor disorders.

The design of spatiotemporal neuromodulation therapies requires three non-

METHODOLOGIES FOR SPINAL CIRCUIT NEUROMODULATION

trivial methodological developments. First, spatial selectivity relies on chronic implants integrating multiple electrodes^{4, 9, 10} that provide access to the distributed matrix of spinal motor circuits. Second, temporal structure necessitates dedicated software to interface real-time extraction of motor circuit dynamics with closed-loop control policies¹¹. Third, the integrated design of hardware, software, and algorithms is contingent on a mechanistic framework that steer these developments.

Here, we addressed these issues simultaneously. We conducted anatomical, computational, and behavioral experiments to extract spinal motor circuit dynamics during movement. These results guided the mechanistic development of chronic implants and computational algorithms to access spatially distributed circuits following precise temporal sequences. We introduce a translational neuroprosthetic toolbox for spatiotemporal neuromodulation of spinal circuits that improved gait performances in various rodent and non-human primate models of spinal cord injury and Parkinson' s disease.

RESULTS

Natural spinal motor circuit dynamics

We injected a retrograde tracer into pairs of antagonist muscles spanning hindlimb joints to reconstruct the anatomical distribution of motoneurons in the spinal cord (**Fig. 1A**). We then recorded the electromyographic (EMG) activity from all traced muscles in conjunction with hindlimb kinematics during natural locomotion in healthy rats (**Fig. 1B**). Muscle activity was projected onto the reconstructed motoneuron matrix to visualize spatiotemporal map of motoneuron activation during gait (**Fig. 1B**). To decompose this map into functional modules, we applied a non-negative matrix factorization onto pooled muscle activity signals across gait cycles. We found that 2 basic, sinusoidal-shaped muscle synergies were sufficient to reconstruct more than 71% of the original signals (**Fig. 1C**). Analysis of weights of each muscle onto each synergy revealed that the first synergy was exclusively related to extensor muscle activity. This synergy was activated during stance and prior to foot strike (**Fig. 1C**). The second synergy primarily combined activity of flexor muscles, and was activated during stance-to-swing transition and throughout swing (**Fig. 1C**). Extraction of motoneuron activation sub-maps associated with each synergy revealed that extensor- and flexor-related functional modules emerged in spatially restricted locations along lumbar segments. Gaussian clustering analysis identified these 2 spatial locations mathematically, which we termed extensor and flexor hotspots (**Fig. 1D**). The temporal structure underlying the activation of these hotspots was captured into the spatiotemporal sequence of hindlimb endpoint trajectories (**Fig. 1D** and **Movie S1**). These results uncovered the spatial location and temporal structure of spinal motor circuit dynamics during natural locomotion in healthy rats.

Translational chronic implants

We combined well-established and innovative neurotechnologies to develop an array of spinal implants for mice, rats, and monkeys (**Fig. 2**). We customized each implant to

the anatomy of the spinal cord and vertebral structures. We reconstructed lumbosacral segments and their dorsal roots in 3D (**Supplementary Figure 1**), and extracted vertebra morphology through computerized tomography imaging (**Fig. 2**).

Gold conducting tracks were patterned onto thin polyimide films (20-40 μ m thick) whose mechanical structure was adjusted to conform the curvilinear surface of the spinal cord (**Fig. 2A,D** and **Supplementary Figure 2**). The implants accommodate up to 16 platinum-coated electrodes to deliver electrical current.

To enable bio-integration into the subdural space, we also designed soft implants using silicone substrate (120 μ m in thickness) and stretchable gold interconnects (35nm in thickness)¹² (**Fig 2B** and **Supplementary Figure 3**). The same technology was exploited to miniaturize epidural implants for mice (**Fig. 2C**).

We next developed dedicated surgical and electrophysiological procedures for inserting and positioning the implants overlying targeted regions of the epidural or subdural space (**Supplementary Figure 4**). To stabilize implants and ensure safe interactions with the biological environment, we conceived a vertebral orthosis adjusted for each species (**Fig. 2** and **Supplementary Figure 4**). In addition, micro-holes were punctuated throughout the implants using a laser, which triggered conjunctive tissue growth that maintains implant positioning over time (**Supplementary Figure 2**).

Repeated impedance and electrophysiological evaluations over several months demonstrated long-term functionality of the implants *in vivo* (**Supplementary Figure 5**). Regular imaging *in vivo* (**Fig. 2**), and neuro-inflammatory assessment after explantation (**Supplementary Figure 6**) revealed bio-integration of both subdural and epidural implants (**Movie S1**).

Implants tailored to achieve spatial selectivity

We showed that epidural spinal cord stimulation primarily recruits myelinated afferent fibers in the dorsal roots¹³. In turn, the elicited neural volley engages motoneurons trans-synaptically through segmental reflex circuits¹³⁻¹⁵. These results

suggest that the recruitment of specific dorsal roots may provide access to selective motor circuits embedded in distinct spinal segments. We tested this hypothesis in order to tailor implants. First, we reconstructed the 3D location of dorsal roots innervating each lumbar segment (**Supplementary Figure 1**), and integrated these reconstructions into a hybrid computational model of the spinal cord¹³. Second, we iterated computerized simulations that predicted optimal rostrocaudal and mediolateral locations of electrodes to access the identified extensor and flexor hotspots (**Supplementary Figure 7**). We found that electrodes located 1.00mm lateral to the border between L2 and L3 segments, and 0.75mm lateral to S1 segment provided optimal access to dorsal roots projecting to flexor and extensor hotspots, respectively (**Fig. 3A**). Third, we performed acute electrophysiological experiments that confirmed model predictions (**Fig. 3B**). Delivery of electrical stimulation through the chronic, tailored implants elicited the predicted unilateral movements of extension and flexion in mice, rats, and monkeys ($p < 0.05$, **Fig. 3C** and **Movie S2**). To confirm the ability of implants to activate motor circuits, we delivered continuous electrical stimulation in healthy mice, rats, and monkeys during natural locomotion. We found that stimulation substantially enhanced the output of hindlimb motor neurons in all the tested species (**Supplementary Figure 8**).

Computational infrastructure for spatiotemporal neuromodulation

We next exploited an advanced real-time control platform¹⁶ to support the development of novel spatiotemporal neuromodulation therapies. We elaborated signal-processing algorithms that detected the timing of any desired locomotor event based on real-time kinematic recordings of bilateral hindlimb endpoint trajectories (**Fig. 4A**). User-defined events triggered adjustments of stimulating electrode configurations through a finite-state machine parallel logic infrastructure (**Fig. 4A**, see **Methods**). The entire loop operated below 20ms, which was appropriate to reproduce the spatial and temporal structure of natural motor circuit dynamics during gait. This

platform provided the technological framework to adjust neuromodulation therapies based on high-fidelity spatiotemporal movement feedback.

Spatiotemporal neuromodulation restores superior walking in paralyzed rats

We leveraged these combined developments to test whether spatiotemporal neuromodulation mediates superior facilitation of locomotion than current stimulation protocols. Adult rats received a complete mid-thoracic spinal cord transection, EMG electrodes into 8 hindlimb muscles, and a tailored polyimide implant inserted epidurally overlying lumbosacral segments. Five weeks post-lesion, all the tested rats exhibited complete hindlimb paralysis when positioned bipedally in a robotic bodyweight support system (**Fig. 4A-B**). The concurrent delivery of serotonergic replacement therapy and continuous electrical stimulation applied to midline of L2/L3 and S1 segments instantly enabled the rats to walk (**Fig. 4B**). The underlying map of motoneuron activation markedly differed from those observed in healthy rats (**Fig. 4B**). In contrast, optimized spatiotemporal modulation (**supplementary Fig. 10**) distributed over electrodes accessing flexion and extension hotspots (**Fig. 4A**) led to motoneuron activation maps that resembled those recorded in healthy rats. Stimulation applied at the correct place with the correct timing enabled paralyzed rats to perform coordinated locomotion with normal level of weight bearing for extended periods of time (**Fig. 4B** and **Movie S4**). Control algorithms exhibited high level of reliability in the detection and triggering of stimulation events (**supplementary Fig. 10**). Nearly all gait parameters significantly improved during spatiotemporal compared to continuous neuromodulation ($p < 0.05$; **supplementary Fig. 10**).

Spatiotemporal neuromodulation resolves limb-specific impairments

We next demonstrate advantages of implants located below the dura mater, in intimate vicinity of spinal tissue (**Fig. 5A**). Computerized simulations revealed that subdural stimulation leads to a more focused voltage field compared to epidural stimulation, suggesting increased spatial selectivity (**Fig. 5B**). Electrophysiological experiments confirmed that subdural stimulation requires reduced current compared to epidural stimulation ($p < 0.05$, **Fig. 5D**). Moreover, the range of current amplitudes through which motor responses remained restricted to one side was significantly larger for subdural compared to epidural location ($p < 0.05$, **Fig. 5C-D**). To illustrate the advantage of this spatial selectivity, we selected a spinal cord injury model leading to unilateral deficits. Adult rats received a lateral thoracic hemisection that rendered the hindlimb ipsilateral to lesion paralyzed (**Fig. 5E**). In the presence of serotonergic replacement therapy, spatiotemporal modulation delivered through the lateral electrodes of the subdural implant promoted coordinated, weight bearing plantar stepping of the paralyzed hindlimb with improved bilateral gait characteristics compared to continuous stimulation (**Fig. 5F-G** and **supplementary Fig. 10** and **Movie S3**).

Neuromodulation reduces gait deficits in animal models of Parkinson's disease

We then sought to demonstrate the versatility of our translational neuroprosthetic toolbox to improve locomotion after neuromotor disorders. We focused on Parkinson's disease since previous work showed that neuromodulation of the spinal cord alleviates gait deficits in pathogenic rodent⁵ and marmoset models. The reported strategy combined large electrodes to generate broad electrical fields that engage ascending fibers running in the dorsal columns¹⁷. This neural drive disrupts aberrant low-frequency synchronous corticostriatal oscillations induced by dopamine depletion⁵.

Here, we conducted similar experiments in more clinically relevant models of Parkinson's disease, both in rats and rhesus monkeys¹⁸⁻²⁰. High-resolution kinematic analyses revealed that both rats and monkeys exhibited the hallmarks of Parkinsonian

syndromes during gait, including periods of freezing, slow motion, and reduced joint excursions (**Fig. 6**, **Supplementary Fig. 13** and **Movie S4**). We performed computerized simulations to identify optimal electrode configurations to generate large voltage fields over the entire extent of lumbar segments (**Fig. 6B**). Continuous neuromodulation of lumbar segments using tailored epidural implants (**Fig. 6B**) immediately ameliorated locomotor execution in both rats and monkeys (**Fig. 6D,G** and **Movie S4**). Neuromodulation led to improved gait timing ($p < 0.05$, **Fig. 6C**), enhanced muscle activity ($p < 0.05$, **Fig. 6F**), and increased amplitude of limb movements ($p < 0.05$, **Fig. 6G** and **Supplementary Fig. 13**).

DISCUSSION

A variety of neural implants integrating myriad electrode contacts have been designed to access the distributed matrix of nerve fibers and neurons within the brain and spinal cord. Empirical, labor-intensive experiments have guided the elaboration of stimulation protocols to maximize therapeutic effects with these implants. However, current stimulation protocols remain rudimentary.

Here, we conceived a translational neuroprosthetic toolbox derived from biological principles to support the development of advanced spinal cord stimulation protocols. We designed neuromodulation therapies integrating spatial selectivity and temporal structure that closely matched the natural dynamics of spinal motor circuits during gait. Compared to current stimulation protocols, spatiotemporal neuromodulation of spinal circuits significantly improved gait execution. Rats with partial or complete spinal cord injury regained full weight-bearing locomotion that closely resembled gait patterns observed in healthy rats.

Using neuroanatomical and functional experiments, we identified the temporal activation profile of spatially restricted hotspots related to extensor versus flexor muscle synergies. The same spinal circuit dynamics have been derived from walking patterns of humans. These hotspots reflect the final motor command, which is

elaborated within nearby interneuronal networks containing distinct cellular nodes that encode muscle synergies related to extension versus flexion. These muscle synergy encoders receive dense synaptic contacts from muscle proprioceptive afferents. Epidural electrical stimulation activates interneurons and motoneurons indirectly through the recruitment of proprioceptive afferent fibers within the dorsal roots. Therefore, we reasoned that implants tailored to activate the proprioceptive afferents projecting to the identified hotspots would engage muscle synergy encoders related to extension versus flexion. By analogy, the recruitment of auditory afferent pathways related to specific tones has guided the development of cochlear implants to restore hearing. Tailored implants targeting specific dorsal roots induced the predicted movements of flexion versus extension on the left and right hindlimbs in mice, rats, and monkeys. This refined strategy only required a few electrodes that were optimally located based on neuroanatomical reconstructions and computerized simulations. In turn, the reduced number of electrodes supported the development of highly reliable hardware. Both epidural and subdural implants displayed long-term functionality and biocompatibility.

The temporal activation profiles of hotspots were captured in the angular trajectory of the foot. Thus, a single parameter provided a simplified and highly reliable feedback signal to design the control software. In turn, optimized algorithms to monitor bilateral foot trajectories in real-time enabled a single input to trigger multiple outputs with high fidelity. Wearable and implanted wireless sensors provide off-the-shelf solutions to monitor foot trajectories in natural environments. This signal can be readily integrated within commercially available platforms to control neuromodulation therapies in real-time.

Continuous neuromodulation of lumbar segments ameliorated many gait characteristics during locomotion in clinically relevant models of Parkinson's disease, both in rats and monkeys. These results illustrate the potential of our translational neuroprosthetic toolbox to support the design of spinal neuromodulation therapies across neuromotor disorders and species. These results also stress the importance of developing new medical devices integrating hardware

METHODOLOGIES FOR SPINAL CIRCUIT NEUROMODULATION

and software that are specifically tailored to improve motor functions with spinal neuromodulation therapies in humans.

Our results provide comprehensive resources and new methods to manipulate spinal circuits in space and time for basic neuroscience research and translational medicine.

EXPERIMENTAL PROCEDURES

IMPLANT DESIGNS

PDMS based implants for mice and rats (Fig. 2, S3)

Soft implants were fabricated using elastic components including silicone (PDMS) and thin gold films (thickness < 1 μ m) that maintain electrical conduction at large tensile strains¹². A silicone membrane (100 μ m, PDMS) is first deposited on a carrier wafer. Following curing, conductive gold interconnects (35nm thickness) are evaporated through a temporary stencil. A second layer of silicone membrane (20 μ m, PDMS) serves as electrical passivation. The passivation layer contains openings co-located with the tips of the gold interconnects, which form active sites for the electrodes. A platinum-based coating is deposited onto the active sites to ensure effective charge injection in tissue. Finally, stainless steel wires with silicone rubber insulation (AS-632, Cooner Wire) are soldered to the implant using a soft conductive paste. The resulting connector is flooded with fast cure silicone to ensure long-term stability. Soft implants include electrode arrays with 3-2-3 electrode configuration in rats, and a 2-2-2 electrode configuration in mice. The process flow and features of both implants are detailed in **fig. S3**.

ANIMAL MODELS AND SURGICAL PROCEDURES

Animal groups and surgical procedures

All surgical procedures conducted in rodents were performed in accordance with Swiss federal legislation and under the guidelines established at EPFL. Local Swiss Veterinary Offices approved all the procedures. Experiments were performed on Lewis rats (LEW/ORLj) with initial weight of 180-200g, and on C57Bl/6J mice with initial weight of 20-25g. Both rats and mice were ordered from Janvier Labs in France.

Experiments in non-human primates were performed in accordance with the European Union directive of September 22, 2010 (2010/63/EU) on the protection of animals used for scientific purposes in an AAALAC-accredited facility following acceptance of study design by the Institute of Lab Animal Science (Chinese Academy of Science, Beijing, China) IACUC and were approved by the Institutional Animal Care and Use Committee of Bordeaux (CE50) under the license number 50120102-A. Food and water were available ad libitum. Animal care was supervised daily by veterinarians skilled in the healthcare and maintenance of nonhuman primates. Two male rhesus monkeys (*Macaca mulatta*, Beijing, PR of China), aged 5 years and 8 years old, and weighting 6.1 kg and 5.4 kg participated in this study. The animals were housed in individual primate cages allowing visual contacts and interactions with monkeys housed in adjacent cages.

Animal groups

(Fig.1) A group of 7 healthy rats were recorded during continuous quadrupedal locomotion on a treadmill to record the simultaneous activity of hindlimb muscles and whole-body kinematics. Prior to surgery rats were handled and trained daily in the locomotor tasks for three weeks.

(Fig.3) Three groups of healthy animals combining 3 mice, 5 rats, and 2 monkeys were recorded in suspended conditions to measure motor evoked responses in implanted muscles, and hindlimb kinematics. Recordings were obtained in suspended conditions. Whole body kinematic and EMG activity was recorded in the same animals during continuous quadrupedal locomotion on a treadmill without and with continuous neuromodulation of the sacral spinal cord (40Hz, 0.15-0.3 ms, 100-300 μ A in rodents, 2 mA in monkeys).

(Fig. 4) Evaluation of spatiotemporal neuromodulation therapies after complete SCI was conducted in a total of 7 rats that were first implanted with a polyimide implant over lumbosacral segments, and with bipolar electrodes into 12 muscles to record EMG activity. After 14 days of recovery from surgery, they received a complete SCI.

METHODOLOGIES FOR SPINAL CIRCUIT NEUROMODULATION

They underwent rehabilitation for 5 weeks, starting 7 days post-SCI, prior to experimental testing.

(Fig. 5) Evaluation of spatiotemporal neuromodulation therapies after lateral hemisection SCI was conducted in a total of 5 rats that were first implanted with a soft implant over lumbosacral segments, and with bipolar electrodes into antagonist muscles of the left and right ankles to record EMG activity. After 14 days of recovery from surgery, they received a lateral hemisection SCI. Experimental testing were conducted between 7 and 14 days post-SCI.

(Fig. 6) Evaluation of neuromodulation therapies in rodent model of Parkinson' s disease was conducted in a total of 7 rats that were first implanted with a polyimide implant over lumbosacral segments, and with bipolar electrodes into antagonist muscles of the left and right ankles to record EMG activity. After 14 days of recovery from surgery, whole-body kinematic and EMG activity was recorded during continuous quadrupedal locomotion on a treadmill, along a straight runway, and over the irregularly spaced rungs of a horizontal ladder. After baseline recordings, AAV-alphasyn was injected bilaterally into the striatum (See below). Locomotor performance was monitored weekly until motor deficits emerged, around 2/3 months post-injection. Only 4 rats showed significant gait impairments, which correlated with a near complete depletion of dopaminergic neurons in the striatum. Experimental testing was conducted over 1-2 weeks in the same conditions as baseline, both without and with continuous neuromodulation therapies.

(Fig. 6) Evaluation of neuromodulation therapies in non-human primate model of Parkinson' s disease was conducted in 2 rhesus monkeys that were first implanted with a polyimide implant over lumbosacral segments, an implanted pulse generator (Synaptix, Belgium), and a wireless system to monitor EMG activity of 8 implanted muscles in the right hindlimb. After 14 days of recovery from surgery, whole-body kinematic and EMG activity was recorded during continuous quadrupedal locomotion on a treadmill at various speeds. They received repeated injections of MPTP until reaching stable score of Parkinson' s disease, respectively PD6 and PD8.

METHODOLOGIES FOR SPINAL CIRCUIT NEUROMODULATION

Experimental testing was conducted over 1-2 weeks in the same conditions as baseline, both without and with continuous neuromodulation therapies.

Surgical procedures

General surgical procedures for the majority of procedures carried out in the various experiments performed in this study have been described previously ^{3, 18}. All the interventions were performed under full general anesthesia with isoflurane in oxygen-enriched air (1-2%). After surgery, rodents were placed in an incubator for optimized recovery from anesthesia. Monkeys were placed in warm sheets until full recovery from anesthesia.

Implantation of intra-muscular electrodes

To record EMG activity, bipolar electrodes were implanted into 10 flexor and extensor muscles spanning each joint of the right hindlimb, and 2 ankle muscles of the left hindlimb. The following muscles were implanted: gluteus medius, iliopsoas, vastus lateralis, semi-tendinosis, biceps femoris, gastronemius medialis, gastronemius lateralis, tibialis anterior, extensor digitorum longus, flexor hallucinis longus. Methods have been described in details previously ⁹. Briefly, recording electrodes were fabricated by removing a small part (1mm notch) of insulation from each the implanted wire (AS631, Coonerwires). A common ground wire (1cm of Teflon removed at the distal end) was inserted subcutaneously over the right shoulder. All electrode wires were connected to a percutaneous amphenol connector (Omnetics Connector Corporation) cemented to the skull of the rat. The proper location of EMG electrodes was verified post-mortem.

Implantation of neural implants into the epidural or subdural space (fig. SX)

Under sterile conditions, a dorsal midline skin incision was made and the muscles covering the dorsal vertebral column were removed. A partial laminectomy was performed at vertebrae levels L3-L4 and T12-T13 to create entry and exit points for the implant. To access the intrathecal space, a 3mm long mediolateral incision was

METHODOLOGIES FOR SPINAL CIRCUIT NEUROMODULATION

performed in the dura mater at both laminectomy sites. A loop of surgical suture (Ethilon 4.0) was inserted through the rostral (T12-T13) dura mater incision and pushed horizontally along the subdural space until the loop emerged through the caudal (L3-L4) dura mater incision. The extremity of the implant was then folded around the suture loop. The loop was then retracted gently to position the implant over the spinal cord. A small portion of the implant protruded beyond the rostral dura mater incision and could be manipulated with fine forceps to adjust the mediolateral and rostrocaudal positioning of the implant. Electrophysiological testing was performed intra-operatively to fine-tune positioning of electrodes with respect to hotspots for flexion and extension (**Fig. 3**). The protruded extremity of the implant became encapsulated within connective tissues, which secured positioning of the implant in the chronic stages.

The soft-to-wires (and microfluidic) connector was secured to the bone using a newly developed vertebral orthosis. The connector was first positioned above the vertebral bone. Four micro-screws (Precision Stainless Steel 303 Machine Screw, Binding Head, Slotted Drive, ANSI B18.6.3, #000-120, 0.125) were inserted into the bone of rostral and caudal vertebrae. Surgical suture (Ethilon 4.0) was used to form a cage around the micro-screws and connector. The walls of the cage were plastered using freshly mixed dental cement (ProBase Cold, Ivoclar Vivadent) extruded through a syringe. After solidification of the dental cement, the electrical wires and microfluidic tube were routed sub-cutaneously to the head of the rat, where the Omnetics electrical connector and the microfluidic access port were secured to the skull using dental cement.

The same procedure was used to insert and stabilize the implants in monkeys. The titanium-based connector was secured to the vertebral bone with titanium screws. The wires were routed sub-cutaneously and connected to an implanted pulse generator (Synaptix, Belgium) inserted into a pouch created between inter-costal muscles. The stimulator allowed delivery of continuous constant-current stimulation through wireless connection.

Spinal cord injury

Rats received a complete transection of the mid-thoracic spinal cord, or a lateral hemisection at the level of segment T7/T8). Under Isoflurane/Dorbene anesthesia, a dorsal midline skin incision was made from vertebral level T5 to L2 and the underlying muscles were removed. A partial laminectomy was performed around T8 vertebra to expose the spinal cord. The exposed spinal cord was then cut with customized tools. All the lesions used in this study were reconstructed post-mortem. Nissl-stained sections were assembled in the Neurolucida image analysis software (MBF Bioscience, USA) to reconstruct the lesion in 3D (e.g. **Fig. 4**).

Animal models of Parkinson's disease

After baseline recordings, rats were rendered parkinsonian with bilateral lesion of the substantia nigra compacta using an AAV2-9 vector expressing human A53T α -synuclein under the control of synapsin I promoter (7.0×10^{12} vg/ml). Sham rats received an AAV2-9 vector expressing the green fluorescent protein (GFP; 2.85×10^{12} vg/ml). Under isoflurane anesthesia, rats were placed in a stereotaxic frame (Kopf, USA) and received two bilateral intranigral injections (Anteroposterior: -5.1 and -5.4; Mediolateral: ± 2.2 and ± 2 ; Dorsoventral: -7.8, in mm from bregma) of either vector as previously described²¹. Hindlimb akinesia was assessed using kinematic analysis during locomotion along a straight runway, and along the irregularly spaced rungs of a horizontal runway.

After baseline recordings, the monkeys were rendered parkinsonian with MPTP-hydrochloride (0.2mg/kg, i.v., Sigma) dissolved in saline, as previously described¹⁸. Daily (9 a.m.) assessment of parkinsonism was performed in home cages for 30 min by two blinded observers using a validated rating scale 1-4 assessing tremor, general level of activity, body posture (flexion of spine), vocalization, freezing and frequency of arm movements and rigidity (for each upper limb). Following stabilization of the

MPTP-induced syndrome (3 months), monkeys underwent a surgical intervention to insert EMG electrodes, spinal implants, and the implanted pulse generator.

Rehabilitation procedures after spinal cord injury

Rats with complete SCI were trained daily for 30min, starting 7 days post-injury. The neurorehabilitation program was conducted on a treadmill using a robotic bodyweight support system (Robomedica) that was adjusted to provide optimal assistance during bipedal stepping. To enable locomotion of the paralyzed legs, a serotonergic replacement therapy combining quipazine and 8-OHDPAT was administered systemically, and tonic electrical stimulation was delivered through the electrodes located overlying the midline of lumbar (L2) and sacral (S1) segments (40Hz, 0.2ms pulse duration, 50-200 μ A)⁹.

ANATOMICAL AND IMAGING PROCEDURES

Histology and explantation of spinal cords (Fig. 1, SX)

At the end of the experimental procedures, rats were perfused with Ringer's solution containing 100 000 IU/L heparin and 0.25% NaNO₂ followed by 4% phosphate buffered paraformaldehyde, pH 7.4 containing 5% sucrose. The spinal cords were dissected, post-fixed overnight, and transferred to 30% phosphate buffered sucrose for cryoprotection. After 4 days, the tissue was embedded and the entire lumbosacral tract sectioned in a cryostat at a 40 μ m thickness.

Anatomical reconstruction of motoneuron location (Fig. 1)

Rats (n = 20) received injections of Fluorogold (2% in sterile saline, 30-80 μ l per muscle) into the tibialis anterior muscle, and in the same surgery, into 1 or 2 additional muscles. The location of the retrogradely-traced motoneurons was reconstructed in 3D from serial spinal cord sections using Neurolucida (MBF

Bioscience). To merge reconstruction from several rats into a unified digital library, the tibialis anterior motor column was used as a landmark in each rat.

Histology of explanted spinal cord (fig. SX)

Astrocytic reactivity was revealed by performing immunohistological staining against glial fibrillary acidic protein (GFAP). Briefly, lumbosacral spinal cord coronal sections were incubated overnight in serum containing anti-Iba1 (1:1000, Abcam, USA) or anti-GFAP (1:1000, Dako, USA) antibodies. Immunoreactions were visualized with appropriate secondary antibodies labeled with Alexa fluor® 488 or 555. Sections were mounted onto microscope slides using anti-fade fluorescent mounting medium and covered with a cover-glass. The tissue sections were observed and photographed with a laser confocal fluorescence microscope (Leica, Germany). Immunostaining density was measured offline using 6 representative confocal images of lumbosacral segments per rat. Images were acquired using standard imaging settings that were kept constant across rats. Images were analyzed using custom-written Matlab scripts according to previously described methods³. Confocal output images were divided into square regions of interest (ROI), and densities computed within each ROI as the ratio of traced fibers (amount of pixels) per ROI area. Files were color-filtered and binarized by means of an intensity threshold. Threshold values were set empirically and maintained across sections, animals and groups. All the analyses were performed blindly.

3D reconstruction of vertebrae, spinal cord and dorsal roots (Fig. 3, fig. SX)

To assess spinal cord morphology, a Nissl staining was performed on 25 evenly spaced lumbosacral cross-sections separated by 0.8 mm, for each mice, rat, and monkeys. The slides were assembled into the NeuroLucida image analysis software (MBF Bioscience, USA) to reconstruct lumbosacral segments and dorsal roots in 3D.

μ-Computed Tomography (Fig. 2)

Repeated imaging of implants in vivo was conducted using the μ-computer

METHODOLOGIES FOR SPINAL CIRCUIT NEUROMODULATION

tomography scanner Skyscan 1076 (Bruker microCT, Kontich, Belgium). Scanner settings were adjusted to avoid artefacts induced by metallic parts of the spinal orthosis (0.5-1 mm aluminum filter, voltage 70-100 kV, current 100-140 μ A, exposure time 120-160 ms, rotation step 0.5 degree). The resultant projection images were reconstructed into 3D renderings of the model using NRecon and GPURecon Server (Bruker microCT, Kontich, Belgium). Rats and mice were kept under Isoflurane anesthesia during the scan to reduce motion artifacts. The spinal cord of monkeys was imaged post-mortem, before explantation. Segmentation and 3D model were constructed with Amira® (FEI Visualization Sciences Group, Burlington, USA).

COMPUTATIONAL MODEL

Hybrid computational model of epidural electrical stimulation (Fig 3, fig. SX)

We previously elaborated an advanced hybrid computational model of epidural electrical stimulation of the rat spinal cord¹³. The model combines (i) finite element modeling of the lumbosacral spinal cord that computes the electrical fields elicited by electrical spinal cord stimulation, and (ii) anatomically realistic anatomical structures to derive the type of fibers and neurons activated by the elicited current fields. For the present simulations, we integrated all the results from the traced motoneurons and reconstructed dorsal roots in the model.

MULTIMODAL RECORDINGS AND DATA ANALYSIS

Recordings of whole-body kinematics, kinetics, and muscle activity (Fig.1,3-6)

Procedures to record kinematics, kinetics, and muscle activity have been detailed previously, both for rodents⁹ and monkeys²². In rats, whole-body kinematics was recorded using the high-speed motion capture system Vicon (Vicon Motion Systems, UK), combining 12 infrared cameras (200 Hz). Reflective markers were attached bilaterally overlying iliac crest, greater trochanter (hip), lateral condyle (knee), lateral malleolus (ankle), distal end of the fifth metatarsal (limb endpoint) and the toe (tip).

3D position of the markers was reconstructed offline using Vicon Nexus software. The body was modeled as an interconnected chain of rigid segments, and joint angles were generated accordingly. EMG signals (2 kHz) were amplified, filtered (10–1000 Hz bandpass), stored and analyzed off-line. Ground reaction forces in the vertical, anteroposterior and mediolateral directions were monitored using a force plate (2 kHz, HE6X6, AMTI) located in the middle of the runways, or below the treadmill belt. Concurrent video recordings (200 Hz) were obtained using two cameras (Basler Vision Technologies) oriented at 90° and 270° with respect to the direction of locomotion. In monkeys, white paint was directly applied on the shaved skin overlying the following body landmarks (unilaterally, left side): the iliac crest, the greater trochanter (hip), the lateral condyle (knee), the lateral malleolus (ankle), the 5th metatarsophalangeal (mtp), the outside tip of the fifth digit (toe), and the scapula. High contrast images were acquired using four orthogonally positioned high-speed video cameras (Simi reality motion systems, Germany, 100 Hz). The Simi motion tracking software was subsequently utilized to obtain 3D spatial coordinates of the markers. The body was modeled as an interconnected chain of rigid segments, and the joint angles were computed accordingly.

Analysis of whole-body kinematics, kinetics, and muscle activity (Fig.1,3-6)

A minimum of 10 step cycles was typically extracted for each hindlimb in each experimental task and rat. A total of XXX parameters quantifying gait (n = 23), kinematics (n = 107), and EMG (n = 84) features were computed for each gait cycle using custom written Matlab scripts and according to methods described in details previously⁹. All the computed parameters are reported in **Supplementary Table 1**. To demonstrate the effects of experimental conditions, and extract parameters that captured the largest amount of variance across rats or between conditions, we implemented a principal component (PC) analysis. PC analyses were applied on all the computed parameters from all individual gait cycles for all the subjects together. Gait cycles were visualized in the new synthetic PC space, and PC scores were extracted to quantify differences between groups or conditions. Parameters highly correlated

(factor loadings) with experimentally relevant PCs were extracted, and regrouped into functional clusters, which were named for clarity. The same parameters and procedures were implemented in rats and monkeys.

Muscle Synergies (Fig. 1)

We applied a non-negative matrix factorization algorithm to compute muscle synergies²³. We applied the algorithm on the averaged EMG activity to derive the weighting components and temporal activation profiles of each synergy. Two muscle synergies were sufficient to account for more 71% of total EMG variance.

Spatiotemporal map of motor neuron activity (Fig. 1)

To visualize spatiotemporal map of motor neuron activity, EMG signals were mapped onto the estimated rostrocaudal location of motor columns²⁴. This approach provides an interpretation of the motor pool activation at a segmental level rather than at the individual muscle level. The maps were constructed by adding up the contributions of each muscle to the total activity at each spinal segment. The motor output pattern of each spinal segment S_i was estimated by the following equation:

$$S_i = \frac{\sum_{j=1}^{n_i} \left(\frac{MN_{ij}}{MN_j} \right) \cdot EMG_j}{\sum_{j=1}^{n_i} \left(\frac{MN_{ij}}{MN_j} \right)} \cdot N_i$$

where n_i is the number of EMG_js corresponding to the i th segment, EMG_j represents the normalized muscle activity, MN_{ij} is the number of motor neurons related to muscle j for the segment i , MN_j is the total number of motor neurons for the muscle j , N_i is the number of muscles innervated by the i th spinal segment. The center of activity (CoA) in the lumbosacral spinal cord was estimated using the following formula:

$$CoA = \frac{\sum_{j=1}^N S_j \times j}{\sum_{j=1}^N S_j}$$

where S_j is the estimated activity of the j th segment and N is the number of segments. Thus, CoA was expressed as its absolute position within the lumbosacral enlargement.

BEHAVIORAL RECORDINGS

Spatiotemporal neuromodulation in rats with SCI (Fig. 4-5, Fig SXX)

Electrochemical stimulation protocols were selected based on an extensive amount of previous studies in rats with complete and incomplete SCI^{3, 11}. The chemical stimulation used during training was administered systemically (complete SCI) or through the microfluidic channel integrated in the chronically implanted implant (lateral hemisection SCI). After a few minutes, epidural (complete SCI) subdural (lateral hemisection SCI) electrical stimulation currents were delivered between relevant electrode sites and an indifferent ground located subcutaneously. The intensity of electrical spinal cord stimulation was tuned (40Hz, 20-150 μ A, biphasic rectangular pulses, 0.2ms duration) to obtain optimal stepping visually.

To optimize the timing of stimulation onset and end for each relevant electrode, we performed a comprehensive mapping to link the timing of stimulation with functional effects.

Behavioral recordings in non-human primate models of Parkinson's disease (Fig.6)

Both monkeys were extensively trained prior to kinematic recordings. Treadmill locomotion was recorded on a custom motorized treadmill. A transparent Plexiglas chamber contained the subject while allowing synchronous recording of continuous locomotion. Before the lesion, video recordings of 10 to 15 steps were acquired for each treadmill speed while the monkey maintained a consistent position on the treadmill. After MPTP injections, monkeys could not produce continuous locomotion on the treadmill. They typically hit the back of the Plexiglas box. In these conditions, we recorded bouts of locomotion during which neuromodulation therapies were turned on and off over short periods of time. The treadmill belt was set at 1.6 km/h.

Statistical analysis

All data are reported as mean values \pm S.E.M. or when indicated in the text, as mean values \pm 1 S.D. Statistical evaluations were performed using one-way analysis of variance (ANOVA), paired Student' s t-test, or repeated-measure ANOVA. The Tukey' s multiple comparisons test was applied when appropriate.

AUTHOR CONTRIBUTION

N.W., E.M.M., P.M., J.D., L.A., M.M., and G.C performed the in vivo experiments. N.W., E.M.M., and G.C analyzed the data. N.W., E.M.M. conducted the statistical analysis. P.M. developed surgical methods for implantation. (ARRAY) developed the implant technology. J.K., Q.B. and N.P. conducted the anatomical evaluations. P.M., J.B., N.P., D.B., G.C. performed the surgeries. N.W., E.M.M., P.M., S.M., and G.C conceived experiments. Q.L., L.B., and S.D. were responsible for the animal models. M.C., A.M., and S.M. performed computational analyses. N.W., E.M.M., J.G., J.D., N.D. and G.C. analyzed the data. N.W., E.M.M., J.G. and G.C. prepared the figures with the help of the other authors. N.W., E.M.M., J.G., and G.C. wrote the manuscript and all the authors contributed to its editing. G.C. supervised all aspects of the work.

ACKNOWLEDGMENTS

We would like to thank Prof. D. Pioletti for providing access to the micro-computed tomography (CT) scanner. Funding was provided by the European Community's Seventh Framework Program [CP-IP 258654, NeuWALK]; a Starting Grant from the European Research Council [ERC 261247, Walk Again]; a Marie Curie Fellowship [331602, e-WALK], Wings for Life, and funding from the National Center of Competence in Research (NCCR) in Robotics and NanoTera.ch program of the Swiss National Science Foundation [SpineRepair].

CONFLICT OF INTEREST

G.C, N.W., M.C, A.L, J.V, S.M. and S.L hold various patents on electrode array designs, computational models for neuromodulation therapies, spatiotemporal neuromodulation algorithms, and robot-assisted rehabilitation enabled by neuromodulation therapies.

REFERENCES

1. Borton, D., Micera, S., Millan Jdel, R. & Courtine, G. Personalized neuroprosthetics. *Science translational medicine* **5**, 210rv212 (2013).
2. Lozano, A.M. & Lipsman, N. Probing and regulating dysfunctional circuits using deep brain stimulation. *Neuron* **77**, 406-424 (2013).
3. van den Brand, R. et al. Restoring voluntary control of locomotion after paralyzing spinal cord injury. *Science* **336**, 1182-1185 (2012).
4. Angeli, C.A., Edgerton, V.R., Gerasimenko, Y.P. & Harkema, S.J. Altering spinal cord excitability enables voluntary movements after chronic complete paralysis in humans. *Brain* (2014).
5. Fuentes, R., Petersson, P., Siesser, W.B., Caron, M.G. & Nicoletis, M.A. Spinal cord stimulation restores locomotion in animal models of Parkinson's disease. *Science* **323**, 1578-1582 (2009).
6. Hassan, S., Amer, S., Alwaki, A. & Elborno, A. A patient with Parkinson's disease benefits from spinal cord stimulation. *J Clin Neurosci* **20**, 1155-1156 (2013).
7. Agari, T. & Date, I. Spinal cord stimulation for the treatment of abnormal posture and gait disorder in patients with Parkinson's disease. *Neurologia medico-chirurgica* **52**, 470-474 (2012).
8. Kiehn, O. Locomotor circuits in the mammalian spinal cord. *Annual review of neuroscience* **29**, 279-306 (2006).
9. Courtine, G. et al. Transformation of nonfunctional spinal circuits into functional states after the loss of brain input. *Nature neuroscience* **12**, 1333-1342 (2009).
10. Gad, P. et al. Development of a multi-electrode array for spinal cord epidural stimulation to facilitate stepping and standing after a complete spinal cord injury in adult rats. *Journal of neuroengineering and rehabilitation* **10**, 2 (2013).
11. Wenger, N. et al. Closed-loop neuromodulation of spinal sensorimotor circuits controls refined locomotion after complete spinal cord injury. *Science translational medicine* **6**, 255ra133 (2014).
12. Lacour, S.P., Chan, D., Wagner, S., Li, T. & Suo, Z. Mechanisms of reversible stretchability of thin metal films on elastomeric substrates. *Applied Physics Letters* **88**, 204103-204101 - 204103-204103 (2006).
13. Capogrosso, M. et al. A computational model for epidural electrical stimulation of spinal sensorimotor circuits. *The Journal of neuroscience : the official journal of the Society for Neuroscience* **33**, 19326-19340 (2013).

METHODOLOGIES FOR SPINAL CIRCUIT NEUROMODULATION

14. Minassian, K. et al. Human lumbar cord circuitries can be activated by extrinsic tonic input to generate locomotor-like activity. *Hum Mov Sci* **26**, 275-295 (2007).
15. Lavrov, I. et al. Epidural stimulation induced modulation of spinal locomotor networks in adult spinal rats. *The Journal of neuroscience : the official journal of the Society for Neuroscience* **28**, 6022-6029 (2008).
16. Wenger, N. et al. Closed-loop neuromodulation of spinal sensorimotor circuits controls refined locomotion after complete spinal cord injury. *Science translational medicine* (in press).
17. Nicoletis, M.A., Fuentes, R., Petersson, P., Thevathasan, W. & Brown, P. Spinal cord stimulation failed to relieve akinesia or restore locomotion in Parkinson disease. *Neurology* **75**, 1484; author reply 1484-1485 (2010).
18. Bezard, E. et al. Relationship between the appearance of symptoms and the level of nigrostriatal degeneration in a progressive 1-methyl-4-phenyl-1,2,3,6-tetrahydropyridine-lesioned macaque model of Parkinson's disease. *The Journal of neuroscience : the official journal of the Society for Neuroscience* **21**, 6853-6861 (2001).
19. Boraud, T., Bezard, E., Bioulac, B. & Gross, C.E. Dopamine agonist-induced dyskinesias are correlated to both firing pattern and frequency alterations of pallidal neurones in the MPTP-treated monkey. *Brain* **124**, 546-557 (2001).
20. Fernagut, P.O. et al. Dopamine transporter binding is unaffected by L-DOPA administration in normal and MPTP-treated monkeys. *PloS one* **5**, e14053 (2010).
21. Engeln, M. et al. Levodopa gains psychostimulant-like properties after nigral dopaminergic loss. *Annals of neurology* **74**, 140-144 (2013).
22. Courtine, G. et al. Kinematic and EMG determinants in quadrupedal locomotion of a non-human primate (Rhesus). *Journal of neurophysiology* **93**, 3127-3145 (2005).
23. Dominici, N. et al. Locomotor primitives in newborn babies and their development. *Science* **334**, 997-999 (2011).
24. Yakovenko, S., Mushahwar, V., VanderHorst, V., Holstege, G. & Prochazka, A. Spatiotemporal activation of lumbosacral motoneurons in the locomotor step cycle. *Journal of neurophysiology* **87**, 1542-1553 (2002).

FIGURE LEGENDS

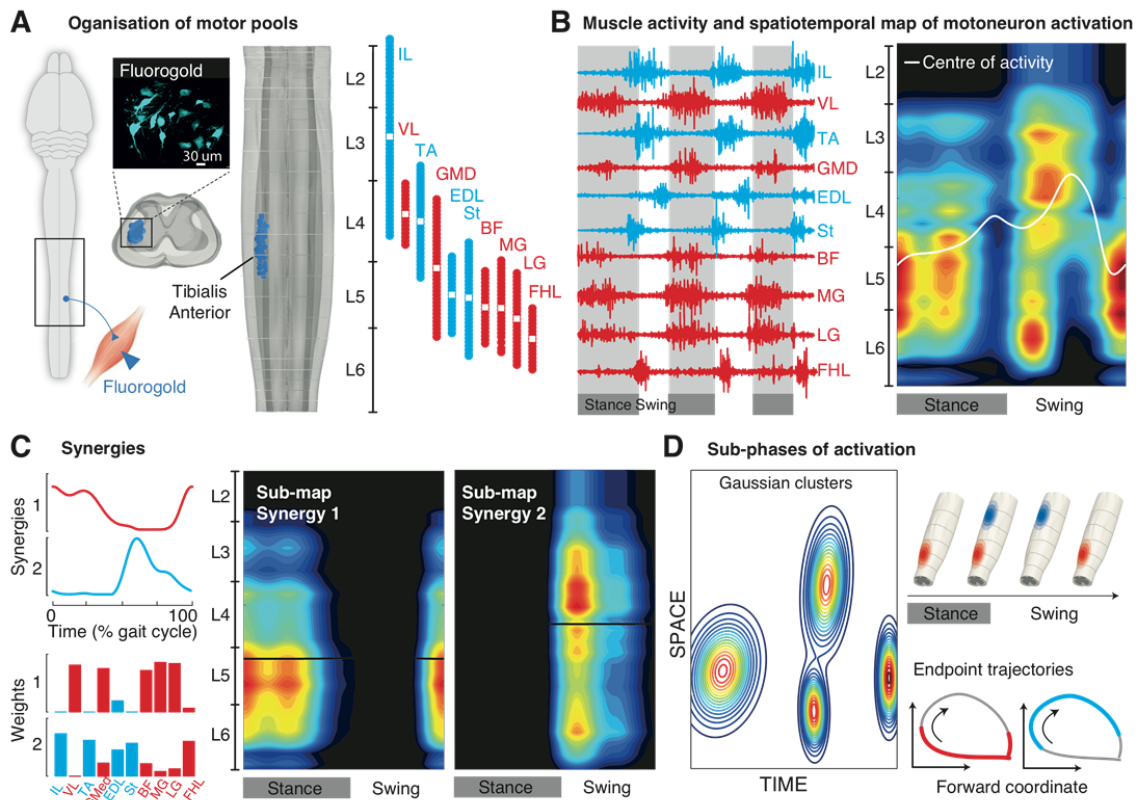


Figure 1: Spatial and temporal structure underlying circuit activation during locomotion.

(A) The retrograde tracer Fluorogold was injected into hindlimb muscles to label motoneurons, as shown in the photograph. The coronal and longitudinal views of lumbosacral segments display the 3D reconstruction of tibialis anterior (TA) motoneuron location. The same procedure was applied to gluteus medius (GMD), iliopsoas (IP), vastus lateralis (VL), semi-tendinosis (St), biceps femoris (BF), gastronectmius medialis (GM), gastronectmius lateralis (GL), extensor digitorum longus (EDL), and flexor hallucinis longus (FHL) muscles to reconstruct the matrix of hindlimb motoneurons within lumbar segments. The rostrocaudal location and center (white dot) of each motoneuron column is indicated in red and blue for extensor and flexor muscles, respectively. (B) Sequence of EMG activity from all the traced hindlimb muscles during locomotion in a healthy rat. Normalized EMG activity was projected onto the identified motoneuron matrix to derive the spatiotemporal map of motoneuron activation during gait. (C) Temporal activation profiles of muscle synergies 1 and 2, and corresponding weights of each muscle onto muscle synergy. Projection of each muscle synergy onto the weighted motoneuron matrix revealed spatiotemporal sub-maps of muscle synergy activation. (D) Spatially restricted hotspots emerging during stance and swing were extracted by applying a Gaussian cluster algorithm onto the spatiotemporal map of motoneuron activation. The sketches display the location of extensor and flexor related hotspots in relation with the spatiotemporal

pattern of limb endpoint trajectory. This analysis identified the main location and timing of motoneuron activation during gait, providing a spatiotemporal structure for neuromodulation therapies.

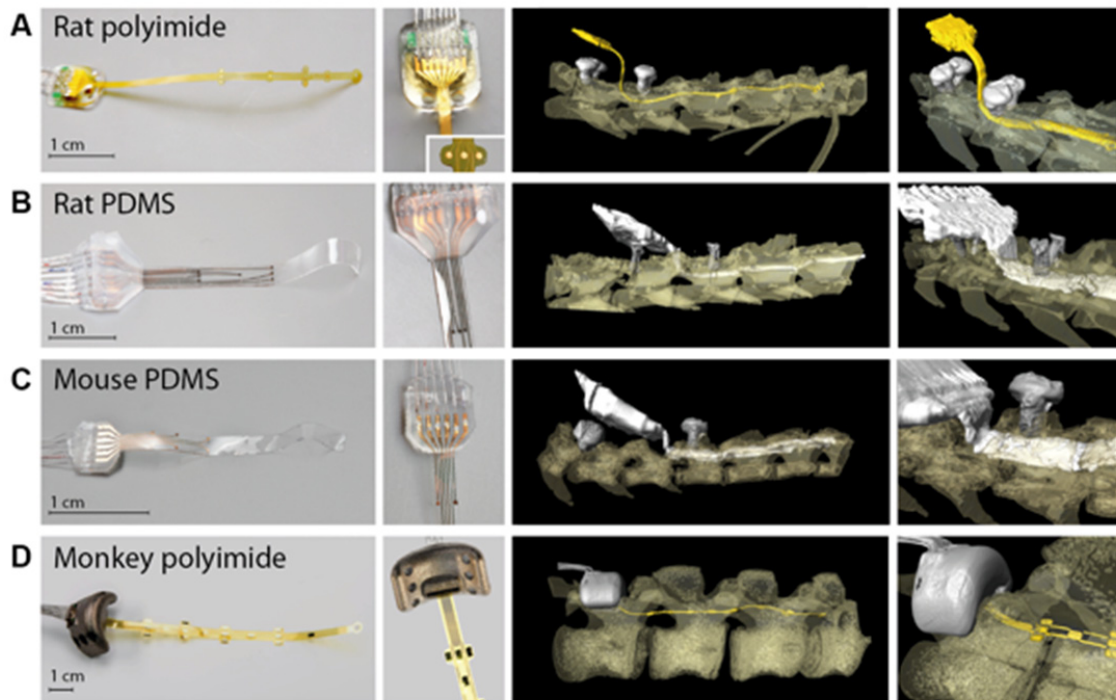


Figure 2: Hardware for spinal neural implants in mice, rats, and monkeys.

(A) Photographs, including zooms on electrodes and connector, showing polyimide-based implants (thickness, 40 μ m) combining 8 electrodes (diameter, 200 μ m) for epidural implantation in rats. The Reconstructed 3D μ -computed tomography (μ CT) scans of the implant inserted epidurally above lumbosacral segments. The scan was taken 7 weeks post-implantation. The polyimide implant is represented in yellow, while the vertebral orthosis (screws) is colored in white. (B) Photographs showing PDMS-based implants (thickness, 120 μ m) combining 8 electrodes (diameter, 300 μ m). The soft material conforms to delicate spinal tissue, allowing insertion into the subdural space in rats, as shown in the reconstructed μ CT scan taken 7 weeks post-implantation. (C) Photographs showing PDMS-based implants (thickness, 120 μ m) combining 6 electrodes (diameter, 300 μ m) for epidural implantation in mice. The 3D μ CT scan was taken 4 weeks post-implantation. (D) Photographs showing polyimide-based implants (thickness, XX μ m) combining 16 electrodes (diameter, 200x200 μ m) for epidural implantation in monkeys. The reconstructed 3D μ CT scan displays the implant inserted on the dorsal aspect of lumbar segments, and the titanium-based orthosis secured onto the L4 vertebra 3 months post-implantation.

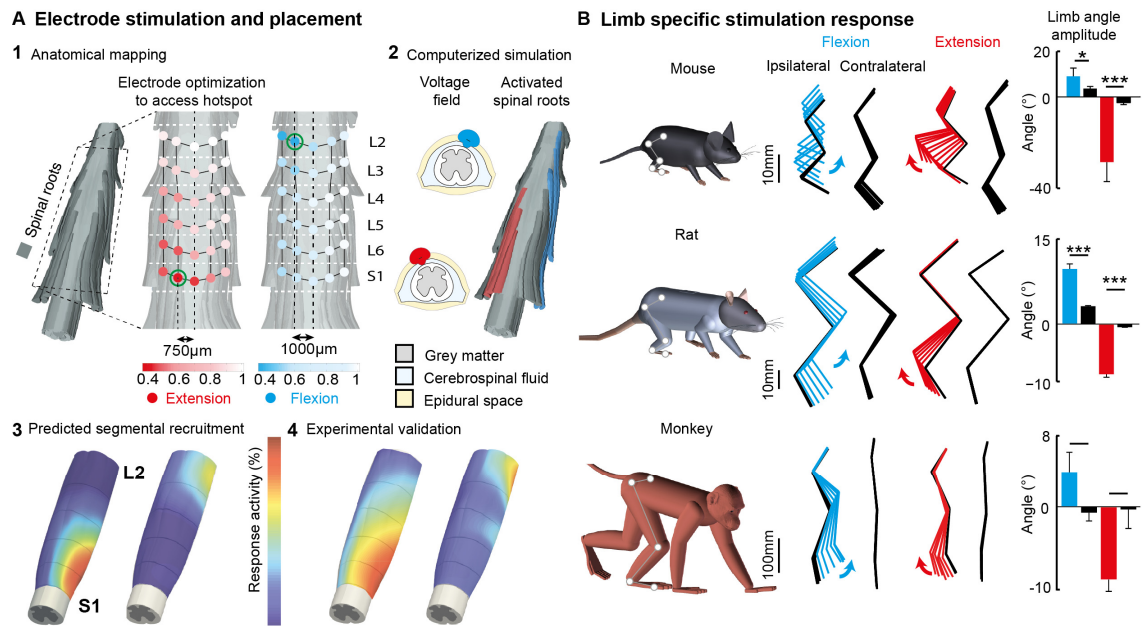


Figure 3: Identification of electrode locations to achieve spatial selectivity

(A) Serial anatomical, computational, and electrophysiological experiments, here shown for rats. (1) Dorsal roots innervating S1 to L1 segments were reconstructed in 3D. The location of hotspots, derived from Gaussian clustering, is displayed along lumbar segments. (2) Computerized simulations were iterated over a grid of electrodes covering the reconstructed lumbosacral segments and dorsal roots. A genetic algorithm identified the optimal mediolateral and longitudinal locations of electrodes (green circles) to preferentially activate dorsal roots projecting to extensor versus flexor related hotspots. (3) Computerized simulations showing isopotential 1V surface following stimulation (150µA) at each identified electrode location, including resulting dorsal root activation. (4) Spatial map of motoneuron activation predicted from computerized simulation. (5) Spatial map of motoneuron activation obtained by projecting motor responses evoked in 8 hindlimb muscles following a single pulse (0.5ms). **(B)** Mice (n = 3), rats (n = 3), and monkeys (n = 3) were chronically implanted with PDMS (mice) or polyimide (rats, monkeys) implants tailored for each species. Under ketamine anesthesia, a single pulse of stimulation was delivered at the hotspots to induce unilateral movements of extension (backward and upward due to passive leg flexion) or flexion (forward and upward). Stick diagram decompositions of bilateral hindlimb movements are shown for each site of stimulation and species. Histogram plots report mean amplitude of elicited displacements for hindlimb ipsilateral (color) and contralateral (black) to the stimulation side. *, significantly different at $p < 0.05$. Error bars, S.E.M.

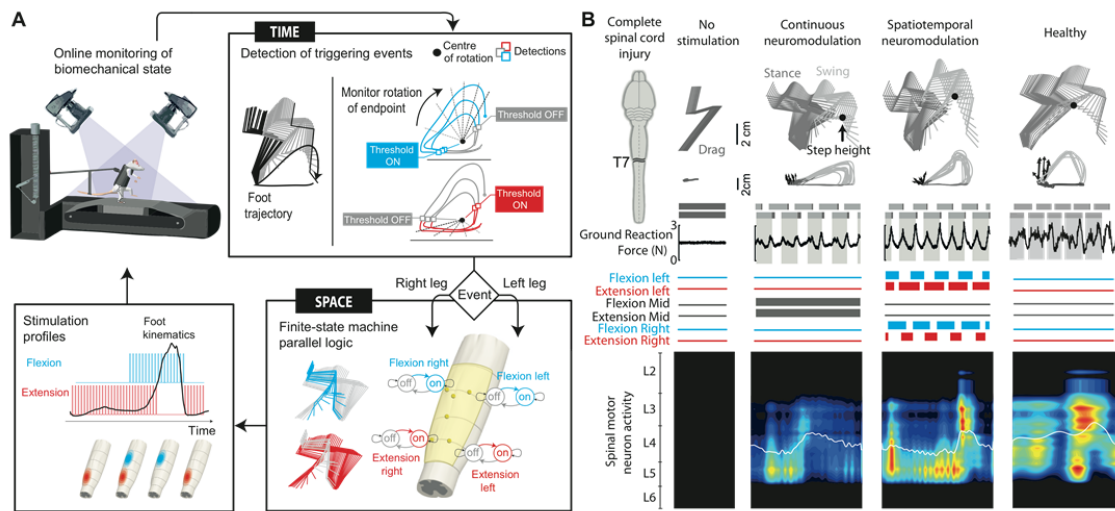


Figure 4: Reproduction of spatial and temporal structure of natural circuit activation during gait

(A) Computational platform to monitor the spatiotemporal trajectory of both left and right limb endpoints in real-time. Rats were supported in a robotic body weight support system above a moving treadmill belt. Angular displacement of the limb endpoint around the computed center of rotation was converted into angular coordinates (dotted grey lines). The activation of extensor- or flexor-related electrodes was triggered when the angular coordinate crossed the defined threshold. The temporal response of control algorithms operated below 20ms. **(B)** Rats with complete transection of thoracic segment T7 ($n = 5$) were tested without stimulation, with continuous neuromodulation applied over the midline of lumbar and sacral segments, and during spatiotemporal neuromodulation over the lateral aspects of the same segment. For each condition, a stick diagram decomposition of hindlimb movements is shown together limb endpoint trajectories, stance and swing phases of both hindlimbs, and vertical ground reaction forces during a sequence of 8 successive steps. The time at which each electrode is turned on and off is displayed below each sequence. The spatiotemporal maps of motoneuron activation were calculated over the entire locomotor sequence. Correlation coefficients between activation profiles of each segment were computed between injured ($n = 5$) and healthy ($n = 5$) rats, reported in each map.

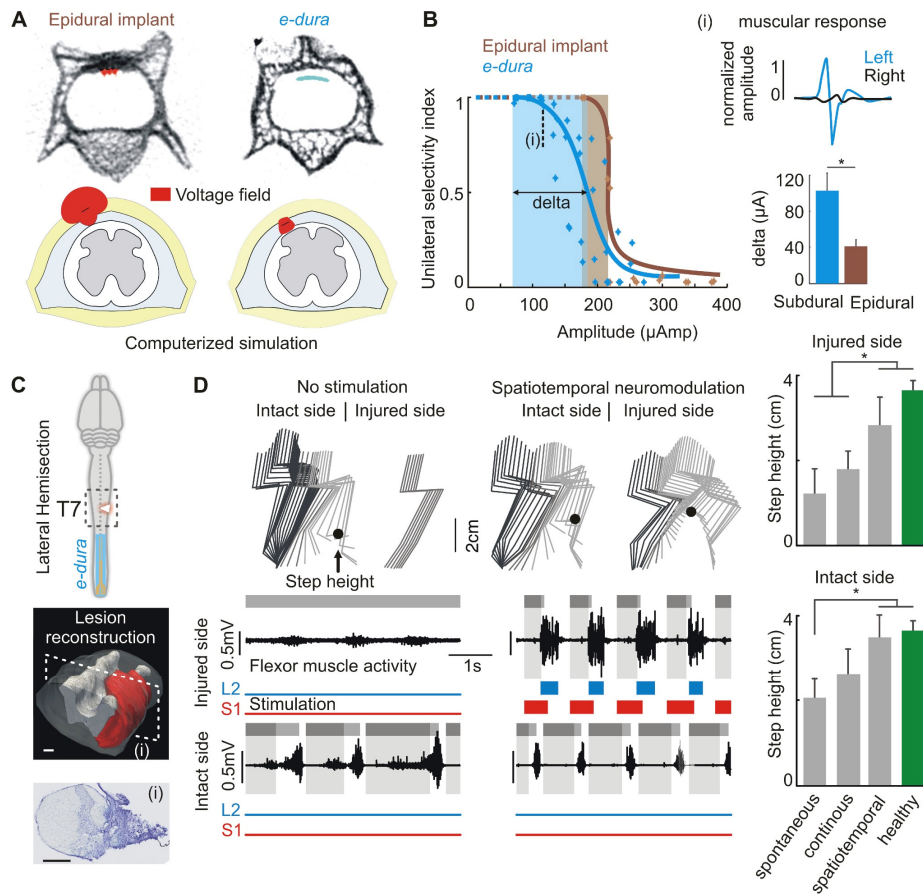


Figure 5: Subdural implants increase efficacy of spatiotemporal neuromodulation

(A) Coronal sections of μ -computed tomography scans taken from chronic (5 weeks) epidural and subdural implants. Computerized simulations display isopotential volume at 1 V following for epidural and subdural stimulations ($150\mu\text{A}$). (B) Relationships between stimulation amplitude and the degree of left-right selectivity obtained with epidural versus subdural implants. The selectivity was calculated from recordings of flexor and extensor muscles of the ankle during acute experiments in the same rats ($n = 3$). Representative responses recorded in left and right ankle muscles following subdural stimulation of left S1 hemi-segment at intensity (i). The histogram plot reports the mean range (+ S.E.M.) over which left-right selectivity remained within functional values (above 0.5) for epidural and subdural stimulation. (C) Scheme, photograph of a Nissl stained coronal section, and 3D reconstruction of the lateral hemisection at T7. The subdural implant was inserted 2 weeks prior to lesion. (D) After 2 weeks of recovery, rats were tested during stepping on a treadmill without stimulation and during spatiotemporal neuromodulation under the same conditions as in Fig. 4. Stick diagram decomposition of bilateral hindlimb movements is shown together with the activity of the tibialis anterior muscles from the injured and intact sides. Conventions are the same as in Fig. 4. (E) Histogram plots reporting the mean (S.E.M.) step height for both hindlimbs under the different experimental conditions. The bar mounted with a sign (*) links conditions that are statistically different at $p < 0.05$.

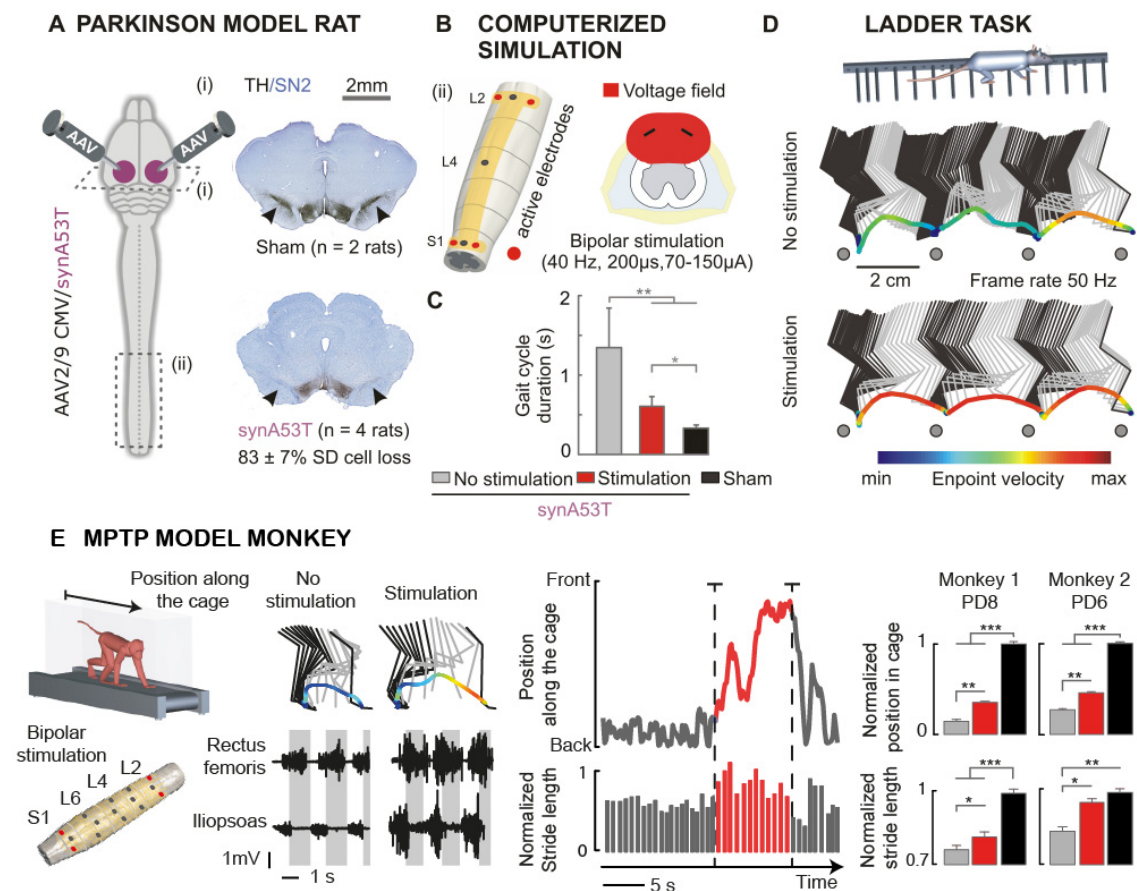
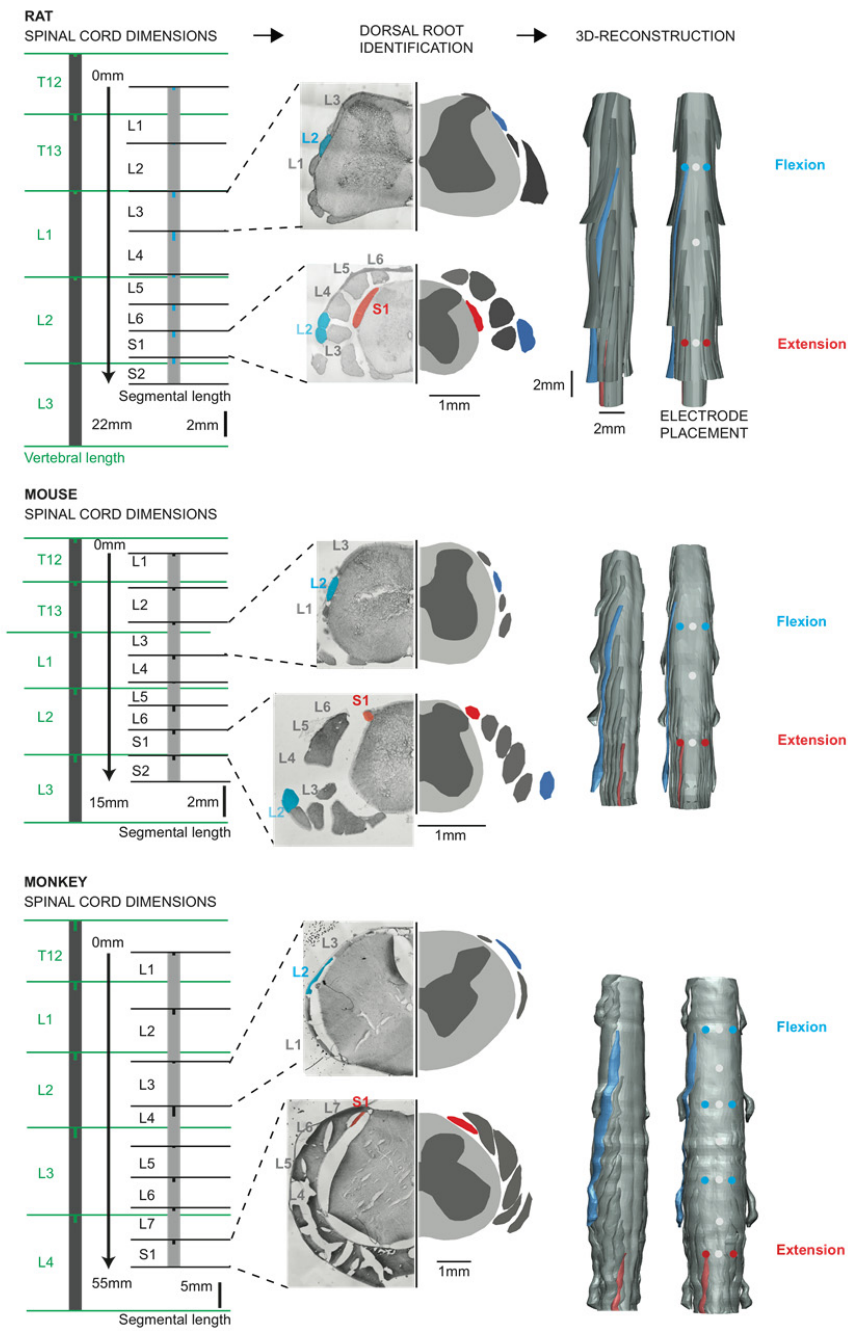


Figure 6: Spinal cord neuromodulation improves gait execution in rodent and primate models of Parkinson's disease

(A) Diagram illustrating the bilateral viral-mediated lesion of substantia nigra to render rats Parkinsonian. Histological quantification of tyrosine hydroxylase (TH) positive cell density in the striatum (arrowheads) and substantia nigra compacta of sham and lesioned rats. (B) Tailored implants and electrode configurations derived from computerized simulations to activate dorsal column fibers bilaterally. The coronal section shows isopotential 1V surface resulting from stimulation (150µA) using the identified bipolar electrode configurations. (C) Quantification of gait cycle duration in sham rats, and lesioned rats without stimulation and during continuous neuromodulation of lumbosacral segments. (D) Sick diagram decomposition of hindlimb movements during a locomotor sequence along a horizontal ladder. Hindlimb kinematics is illustrated for the same rat without and with stimulation. The velocity of limb endpoint trajectories is color-coded to highlight the increased movement speed during stimulation. (E) Tailored implants and electrode configurations to deliver electrical spinal cord neuromodulation in MPTP-treated monkeys during continuous locomotion on a treadmill. Sick diagram decomposition of hindlimb movements together with EMG activity of hip flexor and extensor muscles without and with stimulation in monkey #2. (F) Position of the body along the forward axis of the treadmill enclosure and successive stride lengths while monkey #2 is walking continuously and the stimulation is turned on (red) and off. (G)



Histogram plots reporting the position within the enclosure and stride length (10 trials, X gait cycles) computed for monkeys #1 and #2 before the lesion and after reaching stable Parkinson's disease (PD) scores, indicated for each monkey. *: $p < 0.05$; **: $p < 0.01$; ***: $p < 0.001$; error bars: S.E.M.

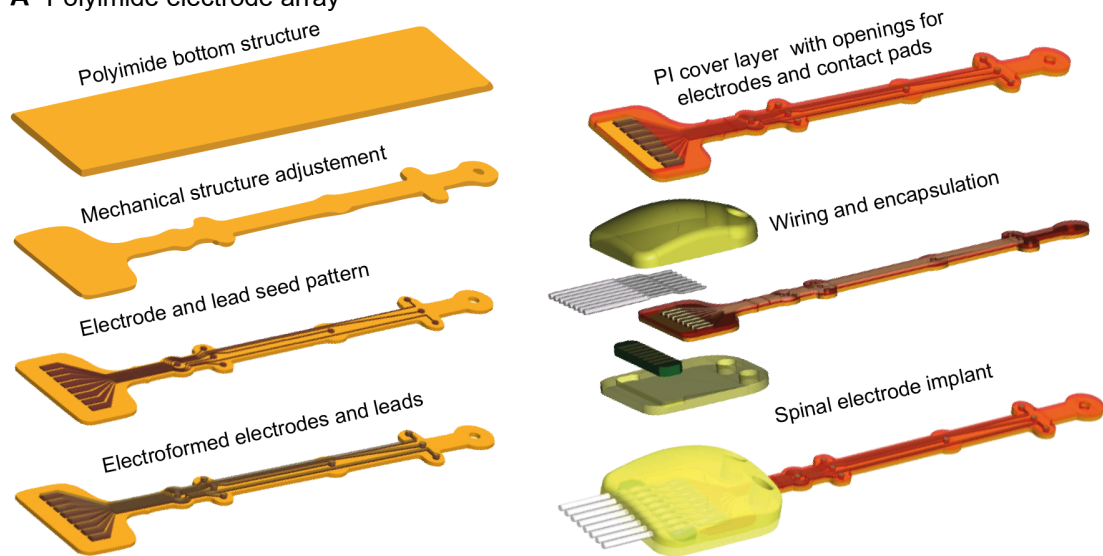
Supplementary Figure 1: Measurement and reconstruction of vertebra, spinal segments, and dorsal roots in mice, rats, and monkeys.

(A) Diagram illustrating the bilateral viral-mediated lesion of substantia nigra to render rats Parkinsonian. Histological quantification of tyrosine hydroxylase

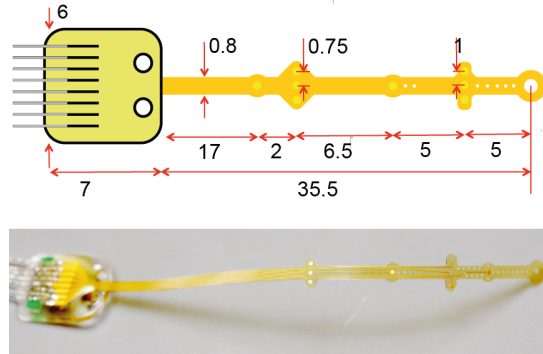
(TH) positive cell density in the striatum (arrowheads) and substantia nigra compacta of sham and lesioned rats. (B) Tailored implants and electrode configurations derive

Array fabrication process

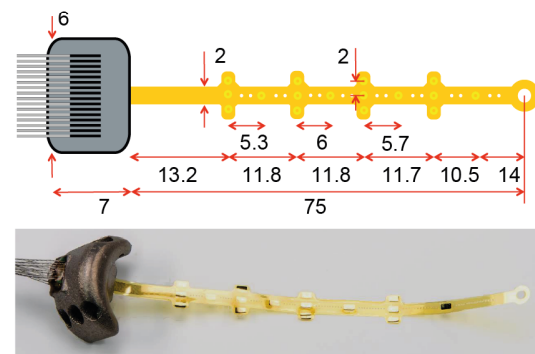
A Polyimide electrode array



B Mask layout for rat epidural array



Mask layout for Monkey array

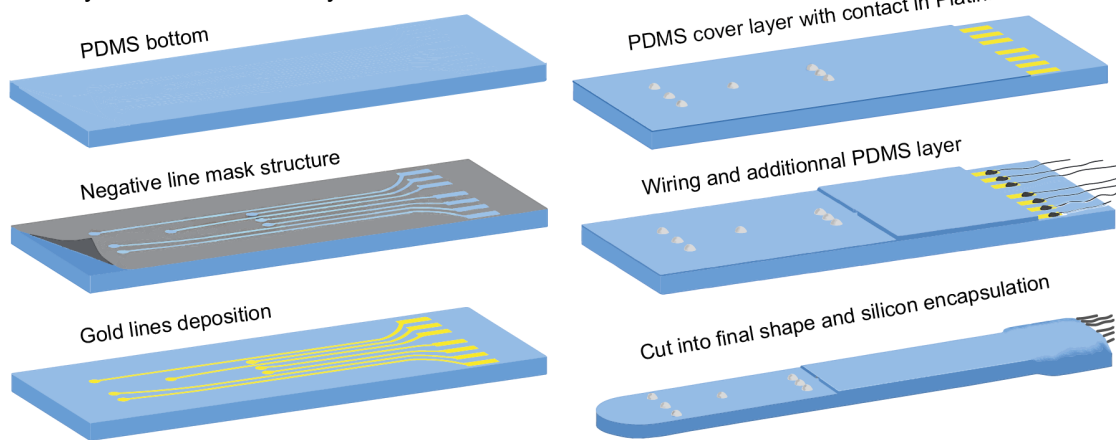


Supplementary Figure 2: Design and fabrication of polyimide-based implants for rats and monkeys

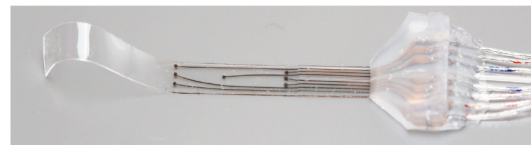
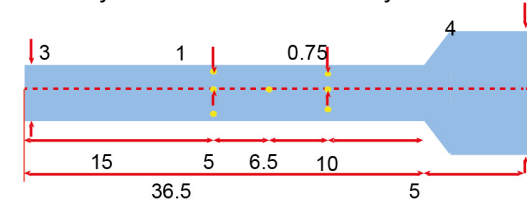
(A) Diagram illustrating the bilateral viral-mediated lesion of substantia nigra to render rats Parkinsonian. Histological quantification of tyrosine hydroxylase (TH) positive cell density in the striatum (arrowheads) and substantia nigra compacta of sham and lesioned rats. (B) Tailored implants and electrode configurations derive

B PDMS electrode array

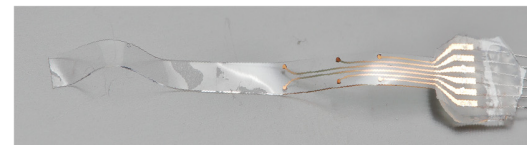
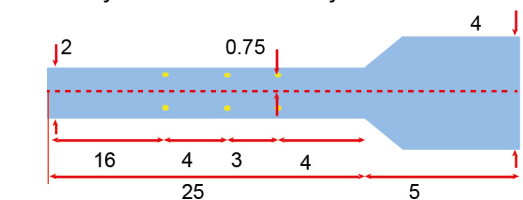
A Polyimide electrode array



Mask layout for rat subdural array



Mask layout for mouse array



.Supplementary Figure 2: Design and fabrication of PDMS-based implants for rats and mice

(A) Diagram illustrating the bilateral viral-mediated lesion of substantia nigra to render rats Parkinsonian. A flexible stencil is laid over a silicone elastomer (PDMS) membrane. The stencil contains the negative of the desired pattern of electrode interconnects.

The interconnects are metallized through the stencil using thermal deposition of gold. The resultant conductive tracks are 35nm in thickness and remain conductive even if the silicone membrane is stretched.

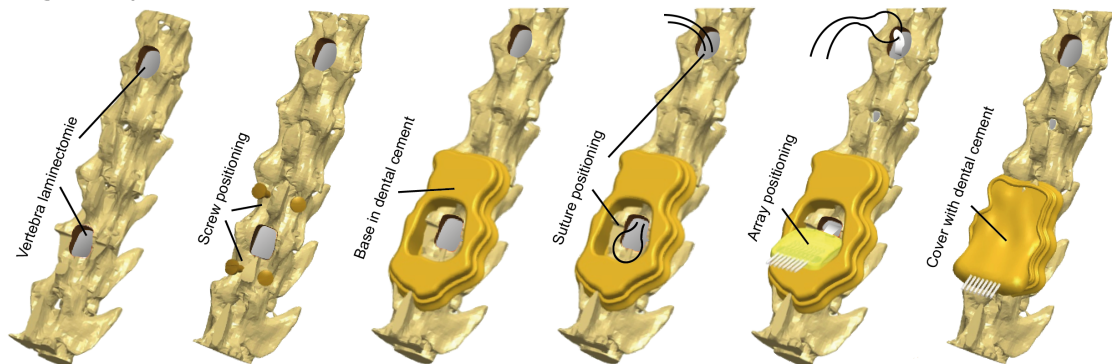
The gold interconnects are passivated using another silicone elastomer (PDMS) membrane containing holes above the active electrode sites. A Platinum based coating is deposited at the active electrode sites forming bumps for better contact with tissue

An additional thin silicone membrane (PDMS) is bonded to the stack. It contains a downward facing groove, thus forming a microfluidic channel. The channel opening is close to the first three active electrode sites and is used to deliver drugs intrathecally.

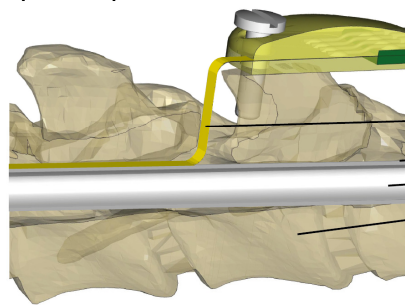
Wire bonding of the array to external electronics is realized with a soft soldering paste.

The connector side of the implant is embedded in quick-set silicone. The implant is cut into its final shape. The implant thickness over the microfluidic portion is approximately 180µm and over the active electrode sites, approximately 130µm

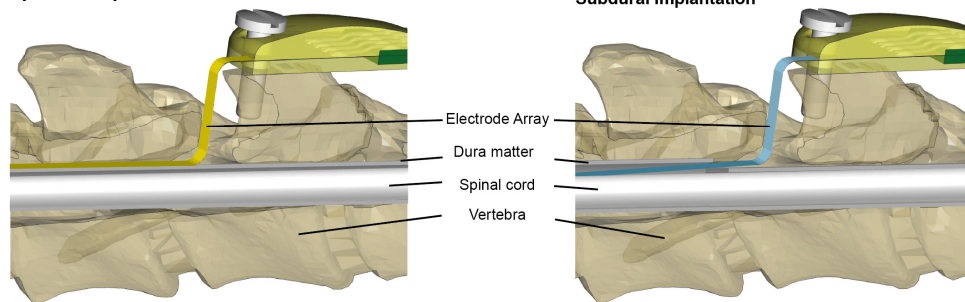
Surgical implantation



Epidural implantation



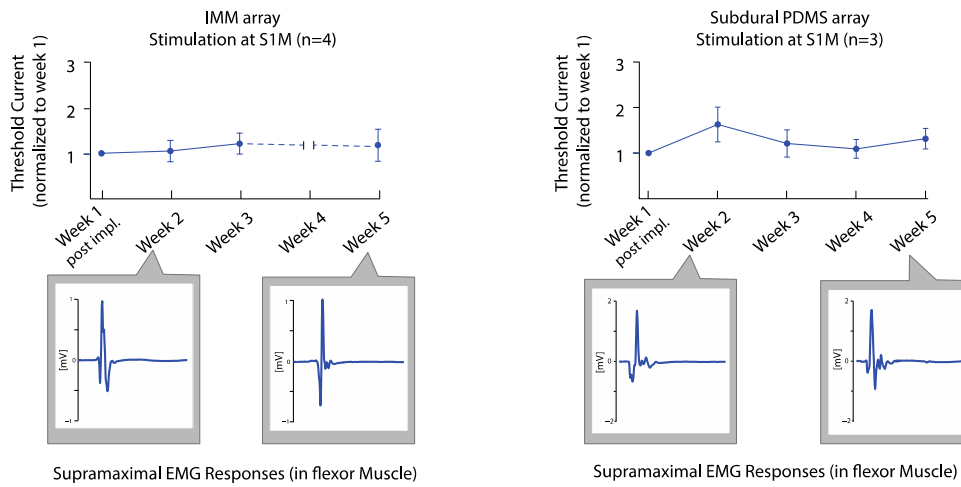
Subdural implantation



Supplementary Figure 4: Surgical procedures for insertion of epidural and subdural implants

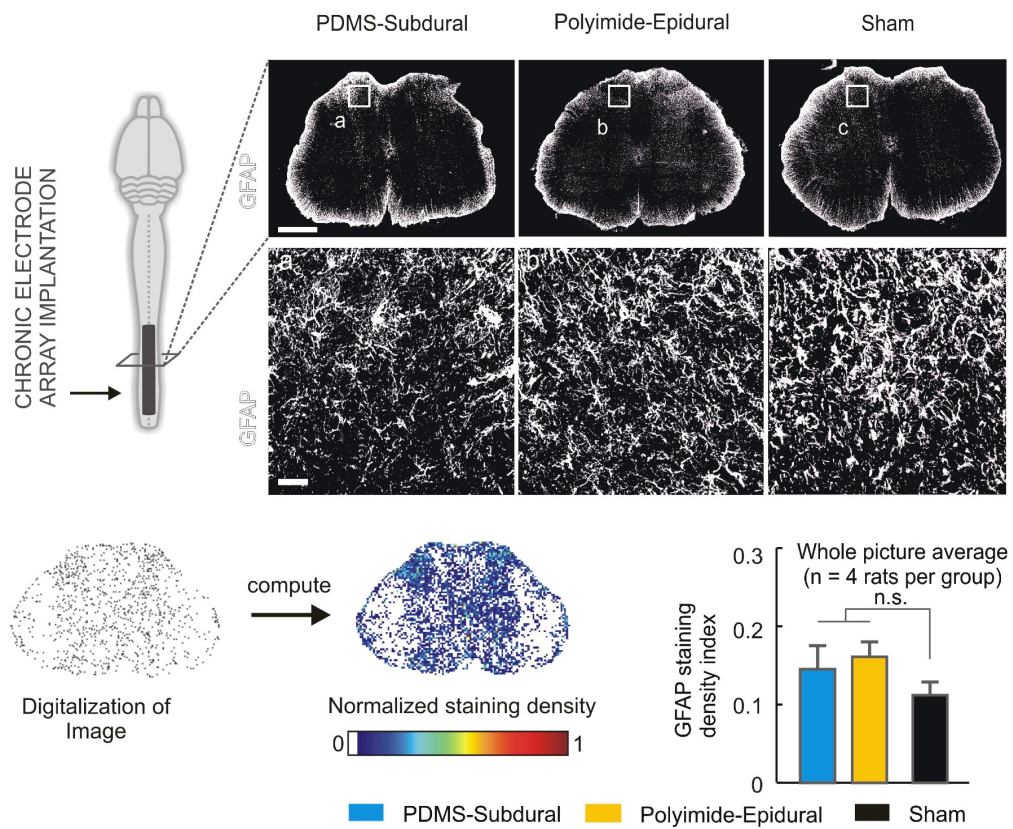
(A) Under sterile conditions, a dorsal midline skin incision was made and the muscles covering the dorsal vertebral column were removed. A partial laminectomy was performed at vertebrae levels L4-L5 (A) and T12-T13 to create entry and exit points for the implant. For subdural implantation to access the intrathecal space, a 3mm long mediolateral incision was performed in the dura mater at both laminectomy sites. A loop of surgical suture (Ethilon 4.0) was inserted through the rostral (T12-T13) dura mater incision and pushed horizontally along the subdural space until the loop emerged through the caudal (L4-L5) dura mater incision. The extremity of the implant was then folded around the suture loop. The loop was then retracted gently to position the implant over the spinal cord. For epidural implantation the extremity of the polyamide implant had the special hole for the fixation and passing in the epidural space by the surgical suture (Ethilon 4.0). For both epidural and subdural technique, a small portion of the implant protruded beyond the rostral dura mater incision and could be manipulated with fine forceps to adjust the mediolateral and rostrocaudal positioning of the implant. Electrophysiological testing was performed intra-operatively to fine-tune positioning of electrodes with respect to lumbar and sacral segments. The soft-to-wires connector was secured to the bone using a newly developed vertebral orthosis. Four micro-screws (Precision Stainless Steel 303 Machine Screw, Binding Head, Slotted Drive, ANSI B18.6.3, #000-120, 0.125) were inserted into the bone of rostral and caudal vertebrae in the entry point laminectomy (B). The walls of the cage were plastered using freshly mixed dental cement (ProBase Cold, Ivoclar Vivadent) extruded through a syringe (C). The connector was positioned above the vertebral bone on the dental cement niche (D). After additional covering of the electrode array connector (E) and solidification of the dental cement,

the electrical wires was routed sub-cutaneously to the head of the rat, where the Omnetics electrical connector was secured to the skull using dental cement



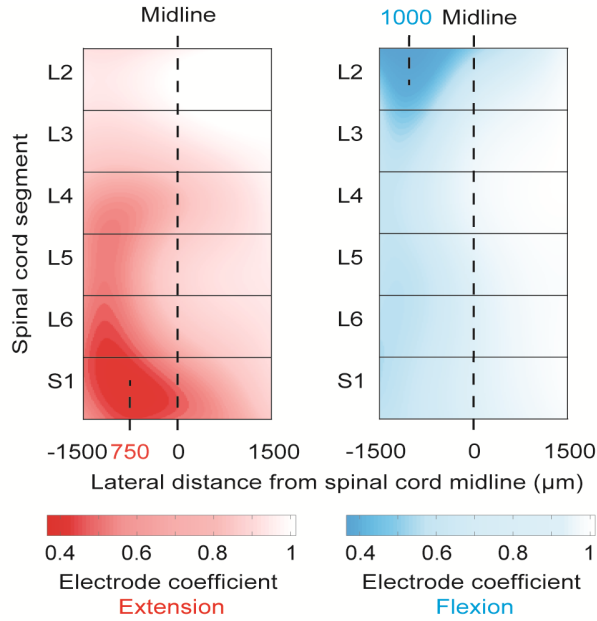
Supplementary Figure 5: Long-term functional of epidural and subdural implants

(A) Diagram illustrating the bilateral viral-mediated lesion of substantia nigra to render rats Parkinsonian. Histological quantification of tyrosine hydroxylase (TH) positive cell density in the striatum (arrowheads) and substantia nigra compacta of sham and lesioned rats. (B) Tailored implants and electrode configurations derive



Supplementary Figure 6: Biocompatibility of epidural and subdural implants in rats.

(A) Diagram illustrating the bilateral viral-mediated lesion of substantia nigra to render rats Parkinsonian. Histological quantification of tyrosine hydroxylase (TH) positive cell density in the striatum (arrowheads) and substantia nigra compacta of sham and lesioned rats. (B) Tailored implants and electrode configurations derive



Calculation of electrode coefficient (f_j^k)

$$f_j^k = \frac{(\sigma_j^k + \mu_C / (\mu_C + \mu_L) + I_{th} / I_{max} + 1/2 \cdot (\sigma_{j-1}^k + \sigma_{j+1}^k))}{4}$$

$$\sigma_j^k = \frac{\sum_{i \in A}^{N_{seg}} n_i^{k,j}}{\sum_{i \in S_L}^{N_{seg}} n_i^{k,j}}$$

$n_i^{k,j}$ = number of fibers stimulated by electrode k, j at segment i

$A = S_L \setminus T$

S_L = set of ipsilateral segment

S_C = set of contralateral segments

T = set of target segments

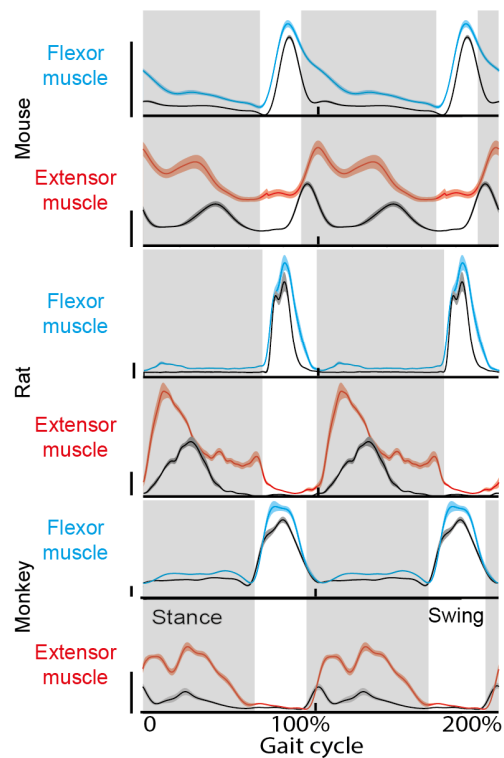
$$\mu_C = \sum_{i \in S_C}^{N_{seg}} n_i^{k,j}$$

$$\mu_L = \sum_{i \in S_L}^{N_{seg}} n_i^{k,j}$$

Supplementary Figure 7: Computerized simulations identifying electrode locations

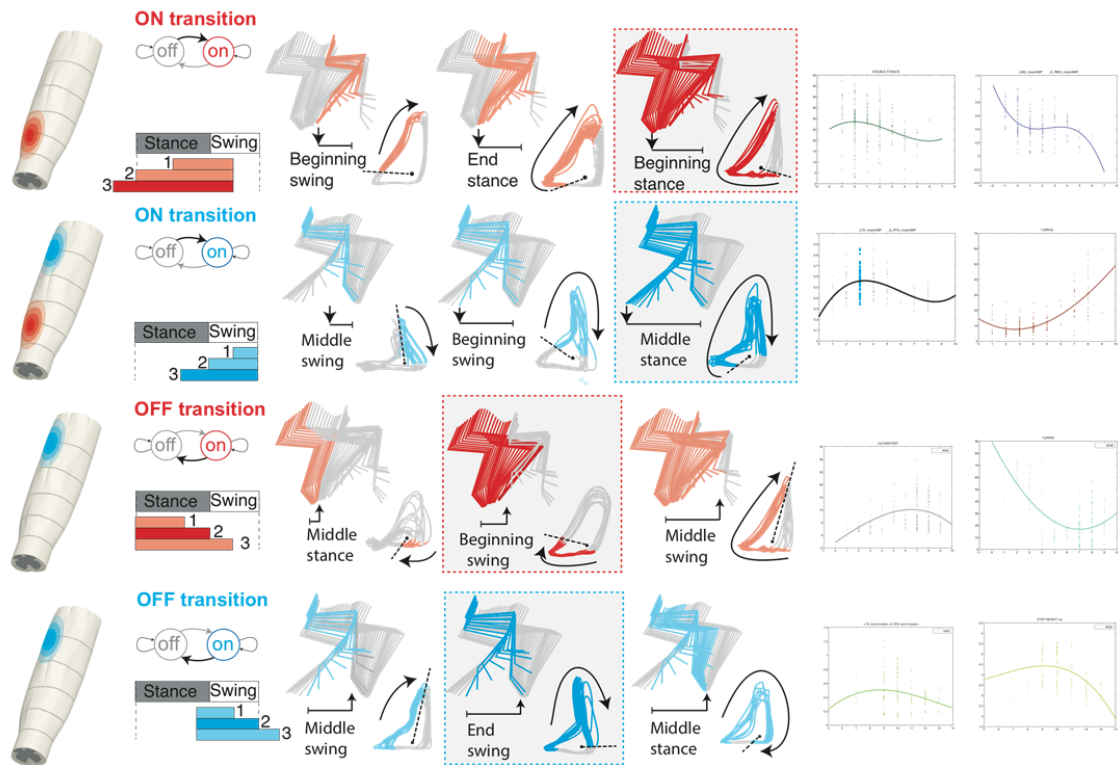
(A) Diagram illustrating the bilateral viral-mediated lesion of substantia nigra to render rats Parkinsonian. Histological quantification of tyrosine hydroxylase (TH) positive cell density in the striatum (arrowheads) and substantia nigra compacta of sham and lesioned rats. (B) Tailored implants and electrode configurations derive

40 Hz Continuous neuromodulation at extensor hotspot in healthy animal



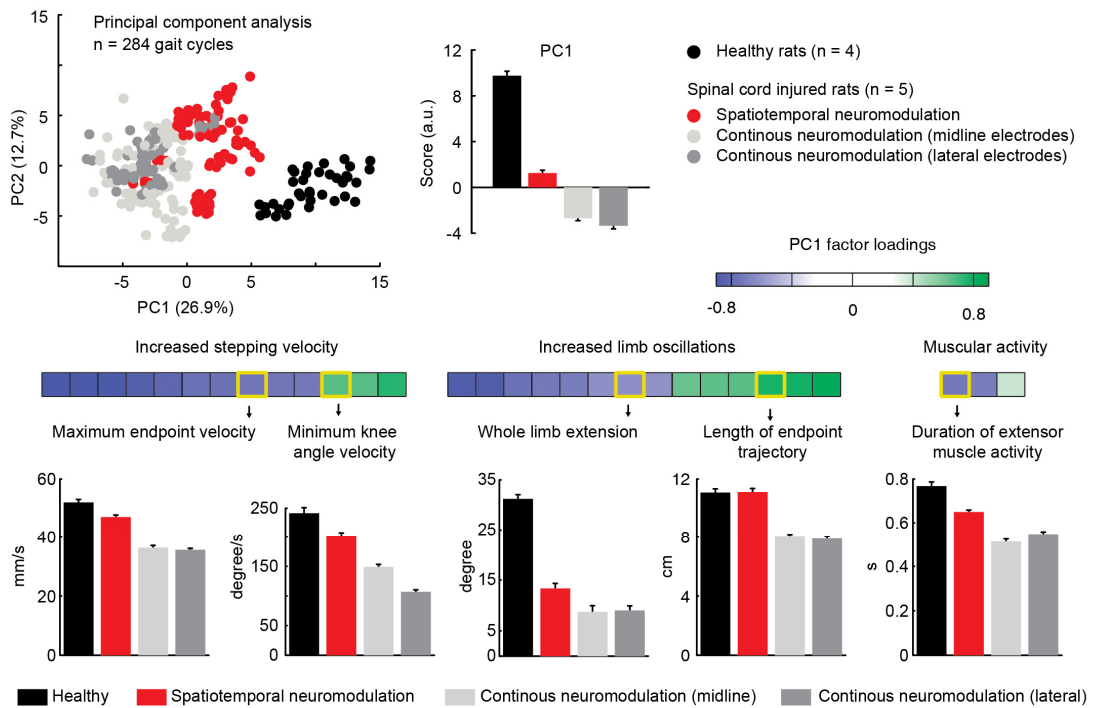
Supplementary Figure 8: Continuous neuromodulation of spinal circuits enhances the output of motoneurons during locomotion in mice rats, and monkeys

(A) Diagram illustrating the bilateral viral-mediated lesion of substantia nigra to render rats Parkinsonian. Histological quantification of tyrosine hydroxylase (TH) positive cell density in the striatum (arrowheads) and substantia nigra compacta of sham and lesioned rats. (B) Tailored implants and electrode configurations derive



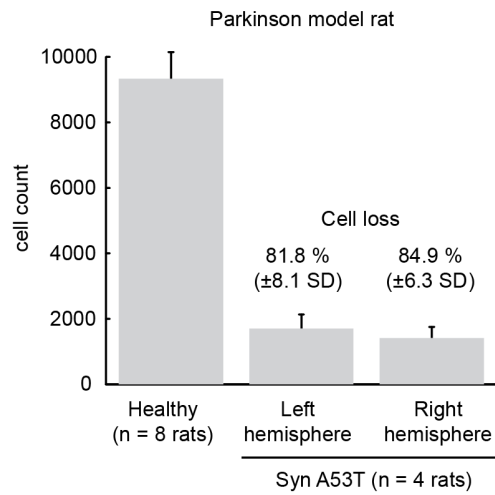
Supplementary Figure 9: Fine-tuning of the temporal structure for spatiotemporal neuromodulation

(A) Diagram illustrating the bilateral viral-mediated lesion of substantia nigra to render rats Parkinsonian. Histological quantification of tyrosine hydroxylase (TH) positive cell density in the striatum (arrowheads) and substantia nigra compacta of sham and lesioned rats. **(B)** Tailored implants and electrode configurations derive



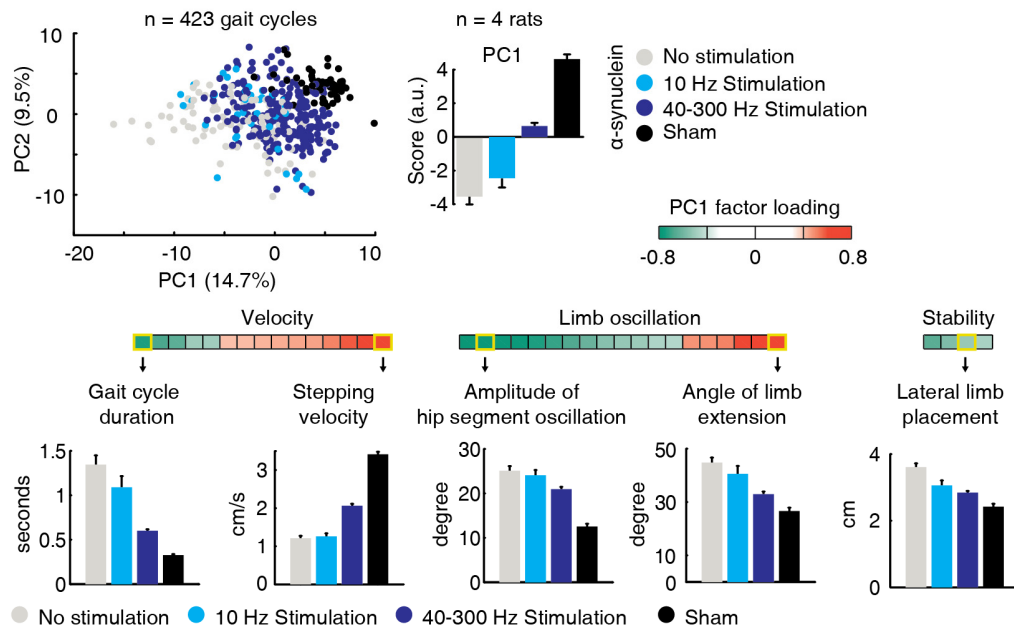
Supplementary Figure 10: Quantification of gait patterns during continuous and spatiotemporal neuromodulation in rats with complete SCI

(A) Diagram illustrating the bilateral viral-mediated lesion of substantia nigra to render rats Parkinsonian. Histological quantification of tyrosine hydroxylase (TH) positive cell density in the striatum (arrowheads) and substantia nigra compacta of sham and lesioned rats. (B) Tailored implants and electrode configurations derive



Supplementary Figure 11: Stereological quantification of cell loss in the substantia nigra in rats

(A) Diagram illustrating the bilateral viral-mediated lesion of substantia nigra to render rats Parkinsonian. Histological quantification of tyrosine hydroxylase (TH) positive cell density in the striatum (arrowheads) and substantia nigra compacta of sham and lesioned rats. **(B)** Tailored implants and electrode configurations derive



Supplementary Figure 12: Quantification of gait patterns during continuous and spatiotemporal neuromodulation in rats with experimental Parkinson's disease

(A) Diagram illustrating the bilateral viral-mediated lesion of substantia nigra to render rats Parkinsonian. Histological quantification of tyrosine hydroxylase (TH) positive cell density in the striatum (arrowheads) and substantia nigra compacta of sham and lesioned rats. **(B)** Tailored implants and electrode configurations derive

Curriculum Vitae

Nikolaus Wenger

MD-PhD Candidate Neuroscience
Center for Neuroprosthetics, EPFL
CH-1015 Lausanne, Switzerland

Tel: +41 76 3408667
Email:
nikolaus.wenger@epfl.ch



Nationality: Austria

Date and Place of Birth: 31.10.1984, Salzburg

PROFESSIONAL PREPARATION

Swiss Federal Institute of Tech. (EPFL)	Neuroscience	PhD	3/2011-9/2014
Swiss Federal Institute of Tech. (ETHZ)	Neuroinformatics	MSc. ETH	3/2011
Medical University of Innsbruck, Austria	Medicine	MD	9/2009
USMLE Step 1 (Score report: 99)			3/2009

RECENT PUBLICATIONS

1. **Wenger N**, Moraud EM, Raspopvic S, Bonizzato M, DiGiovanna J, Musienko P, Micera S, Courtine G. Closed-loop neuromodulation of spinal sensorimotor circuits controls refined locomotion after complete spinal cord injury, ***Science Translational Medicine (in press)***
2. Capogrosso M, **Wenger N**, Raspopovic S, Musienko P, Beauparlant J, Luciani LB, Courtine G and Micera S. A computational model for epidural electrical stimulation of spinal sensorimotor circuits. ***Journal of Neuroscience*** (2013)
3. Borton D, Bonizzato M, Beauparlant J, DiGiovanna J, M. Moraud E, **Wenger N**, Musienko P, Minev I, Lacour S.P., Millán J, Micera S, Courtine G. Corticospinal neuroprostheses to restore locomotion after spinal cord injury. ***Journal of Neuroscience Research*** (2013)
4. **Wenger N**, M. Moraud E, Gandar J, DiGiovanna J, Courtine G and Micera S 'A real-time platform for studying the modulatory capacity of epidural stimulation after spinal cord injury' ***6th International IEEE EMBS Conference on Neural Engineering*** (2013)
5. Mitterberger MC, Lechner S, Mattesich M, Kaiser A, Probst D, **Wenger N**, Pierer G, Zwerschke W. DLK1(PREF1) is a negative regulator of adipogenesis in D105⁺/CD90⁺/CD34⁺/CD31⁻/FABP4⁻ adipose-derived stromal cells from subcutaneous abdominal fat pats of adult women. ***Stem Cell Res.*** (2012)
6. **Wenger N**, Musienko P, Moraud EM, Gandar J, Micera S, Courtine G. Translational neuroprosthetic toolbox for spatial and temporal modulation of spinal circuits. (***in preparation***)
7. Minev I, Musienko P, Hirsch A, Barraud Q, **Wenger N**, Martin Moraud E, Milekovic T, Gandar J, Capogrosso M, Fajardo Torres R, Vachicouras N, Liu Q, Pavlova N, Duis S, Asboth L, Larmagnac A, Vörös J, Micera S, Suo Z, Courtine G, Lacour S. Electronic dura mater for chronic multimodal neural interfaces. ***submitted***

PATENTS

1. **System to deliver adaptive electrical spinal cord stimulation to facilitate and restore locomotion after a neuromotor impairment**, Patent filed to EPO (MBP13367-EP)

Curriculum Vitae

2. Spinal cord multi electrode array for multipolar selective stimulation, (in preparation)

TEACHING

Neuroscience for engineers, EPFL	Spring 2013
Teaching assistant Physiology (EMG, NLG, ECG), EPFL	Winter/Spring 2012- 2013
Teaching assistant Neuroprosthetics, EPFL	Winter 2012

Supervision of Master Students:

Marco Bonizzato, 2011
Characterization of epidural electrical stimulation after complete spinal cord injury
Jerome Gandar, 2012
Real time control of multisite spinal cord stimulation after spinal cord injury
Nicolas Vachicouras, 2013
In vivo validation of stretchable biomaterials for spinal cord stimulation

CLINICAL INTERNSHIPS

Clinical Year ('Klinisch Praktisches Jahr') Medical University of Innsbruck, Austria (Surgery, Internal Medicine, Pediatrics, Neurology, Psychiatry, Radiology)	8/2008 – 9/2009
---	-----------------

National Institute of Neurology, Queen Square University College London, England	5-7/2009
---	----------

Medical Research Unit for Malaria in African Children Albert Schweitzer Hospital, Lambaréné, Gabun, Africa	10-12/2008
---	------------

LANGUAGE

English fluent Residency in Langley, British Columbia, Canada	7/2001-3/2002
--	---------------

French, level B1 Residency in Lausanne, Switzerland	3/2012-9/2014
--	---------------

OTHER ACTIVITIES

University Big Band Innsbruck and Big Band Jazz Ensemble on Jazz Piano	2004 – 2010
--	-------------

Speaker for the Austrian Association for Social Services Abroad (Tirol, Austria) www.auslandsdienst.at	2004 – 2009
--	-------------

Hobbies: Hiking, Tennis, Volleyball, Contemporary Dance